UNIVERSITÄT
BAYREUTH

BayBatt
Bayerisches Zentrum für Batterietechnik

Application of 2D Clay Materials for Sustainable Energy Storage

DISSERTATION

zur Erlangung des akademischen Grades eines
Doktors der Naturwissenschaften (Dr. rer. nat.)
in der Bayreuther Graduiertenschule für Mathematik und Naturwissenschaften (BayNAT)
der Universität Bayreuth

vorgelegt von

Sebastian Weiß

geboren in Kulmbach

Bayreuth, März 2023

Die vorliegende Arbeit wurde in der Zeit von Oktober 2019 bis März 2023 in Bayreuth am Lehrstuhl für Anorganische Chemie I unter Betreuung von Herrn Professor Dr. Josef Breu angefertigt.

Vollständiger Abdruck der von der Bayreuther Graduiertenschule für Mathematik und Naturwissenschaften (BayNAT) der Universität Bayreuth genehmigten Dissertation zur Erlangung des akademischen Grades eines Doktors der Naturwissenschaften (Dr. rer. nat.).

Form der Dissertation: Kumulative Dissertation

Dissertation eingereicht am: 03.03.2023

Zulassung durch das Leistungsgremium: 30.03.2023

Wissenschaftliches Kolloquium: 10.10.2023

Amtierender Direktor: Prof. Dr. Jürgen Köhler

Prüfungsausschuss:

Prof. Dr. Josef Breu	(Gutachter)
Prof. Dr. Anna Schenk	(Gutachterin)
Prof. Dr. Seema Agarwal	(Vorsitz)
Prof. Dr.-Ing. Christina Roth	

Meiner Mutter

Table of Contents

List of Abbreviations

A	Ampere
Å	Angstrom
at-%	Atom percent
CA	Chronoamperometry
CE	Counter Electrode
CP	Chronopotentiometry
CV	Cyclic Voltammetry
dec	Decade
DFT	Density Functional Theory
e.g.	*Exemplum gratia*, for example
EDLC	Electrical Double-Layer Capacitor
et al.	*Et alii*, and others
ETI	Energy Transition Index
FT-IR	Fourier-Transformed Infrared
g	Gram
GC	Glassy Carbon
GR	Green Rust
GR*	Mössbauerite
HDS	Hydroxy Double Salt
HER	Hydrogen Evolution Reaction
HOR	Hydrogen Oxidation Reaction
i.e.	*Id est*, that is
ICP-AES	Inductively Couples Plasma - Atomic Emission Spectroscopy
ITO	Indium Tin Oxide
L	Liter
LDH	Layered Double Hydroxide
LHS	Layered Hydroxide Salt
LSV	Linear Sweep Voltammetry
M	Molarity
m	Meter
NMBC	Noble Metal-Based Catalyst
OER	Oxygen Evolution Reaction

ORR	Oxygen Reduction Reaction
PEEK	Polyether Ether Ketone
PHS	Pumped Hydro Storage
PXRD	Powder X-ray Diffraction
RDE	Rotating Disk Electrode
RE	Reference Electrode
RHE	Reversible Hydrogen Electrode
SEM	Scanning Electron Microscopy
TEM	Transmission Electron Microscopy
V	Volt
WE	Working Electrode
wt-%	Weight Percent
XPS	X-ray Photoelectron Spectroscopy

List of Symbols

b	Tafel Slope
E	Cell Potential
F	Faraday Constant
i_0	Exchange Current
j	Current Density
n	Amount of Substance
p	Pressure
R	Universal Gas Constant
T	Temperature
x	Ratio
α	Transfer Coefficient
ΔG_r	Gibbs Free Energy
η	Overpotential

1 Summary

Together with energy harvesting and distribution, energy storage technologies are essential to broadly establish renewable energy sources in a power grid. Chemical energy storage, e.g., through hydrogen, requires two conversion steps. Step one resembles the storage of electrical energy in chemical bonds (electrolyzer), and step two reverses this process (fuel cells). This work will introduce the technology of green hydrogen generation via water electrolysis and illustrate why efficient and sustainable catalyst systems based on non-toxic, abundant, and cost-effective materials are required.

For this purpose, the investigations focus on 2D layered materials, which have proven to be a versatile material class to facilitate the oxidative half-reaction of electrochemical water splitting, which is the oxygen evolution reaction (OER). This work will focus on the structure-property relationship in such materials while also paying attention to the ecological aspects of the technology. The aim is to tailor catalytical systems, further improving their capabilities and scalability.

In the scope of this work, the influence of composition, specifically iron-content, in layered double hydroxides is investigated concerning the triggering of grafting. That is the chemical bonding of interlayer anions to brucite-like layers. Due to the high importance of bimetallic iron-containing layered double hydroxides, it is crucial to understand which implication its incorporation bears for the structure and, ultimately, the catalytic performance. The systematic variation of Co/Fe composition within the layers showed that the presence of iron favors grafting, thereby inducing structural disorder in the form of random interstratification and planar defects. At the same time, having a minimum amount of Co in the structure is essential to ensure high catalytic activity.

From the perspective of the structure-properties relationship, the question remains open as to what kind of effect the extent of grafting has. For this purpose, different brucite-type materials are compared. Three classes are chosen that feature inherently different interlayer constitutions, while the layers have similar compositions. These include metal hydroxides $M(OH)_2$ without interlayer anions, layered double hydroxides with free interlayer anions, and hydroxynitrates with fully grafted interlayer anions. This work shows that an interlayer anion's chemical bonding can alter the metal centers' electronic structure. This is decisive for their oxidation potential, i.e., the potential at which the electrocatalytically active center forms.

In the last part of this work, the previously gained knowledge is combined to achieve control of grafting within the same material. The all-iron electrocatalyst mössbauerite is known to exhibit extensive grafting of interlayer anions. By employing a corrosion engineering approach, it is possible to obtain its precursor green rust on a steel plate as a large area electrode and control the ratio of grafted to ungrafted interlayer anions by choice of the oxidation method. This control of grafting in the same material allows for the first systematic study on the influence of grafting in mössbauerite.

This thesis is presented as a cumulative work; therefore, the results are described thematically in the attached manuscripts.

2 Zusammenfassung

Zusammen mit der Energiegewinnung und -verteilung sind Energiespeichertechnologien unerlässlich, um erneuerbare Energiequellen in einem Stromnetz auf breiter Basis zu etablieren. Die chemische Energiespeicherung, z. B. durch Wasserstoff, erfordert zwei Umwandlungsschritte. Schritt eins ist die Speicherung elektrischer Energie in chemischen Bindungen (Elektrolyseur) und Schritt zwei ist die Umkehrung dieses Prozesses (Brennstoff Zellen). In dieser Arbeit wird die Technologie der grünen Wasserstofferzeugung durch Wasserelektrolyse vorgestellt und erläutert, warum effiziente und nachhaltige Katalysatorsysteme auf der Grundlage ungiftiger, üppig vorhandener und kostengünstiger Materialien erforderlich sind.

Zu diesem Zweck konzentrieren sich die Untersuchungen auf 2D-Schichtmaterialien, die sich als vielseitige Materialklasse erwiesen haben, um die oxidative Halbreaktion der elektrochemischen Wasserspaltung, die Sauerstoffentwicklungsreaktion (OER), zu erleichtern. Diese Arbeit wird sich auf die Struktur-Eigenschafts-Beziehung in solchen Materialien konzentrieren, wobei auch ökologische Aspekte der Technologie berücksichtigt werden. Ziel ist es, die katalytischen Systeme weiter zu optimieren, um ihre Eigenschaften zu verbessern und die Möglichkeit der Skalierbarkeit zu erfüllen.

Im Rahmen dieser Arbeit wird der Einfluss der Zusammensetzung, speziell des Eisengehaltes in geschichteten Doppelhydroxiden, auf die Auslösung des Graftings untersucht. Das ist die chemische Bindung von Zwischenschichtanionen an Brucit-artige Schichten. Aufgrund der großen Bedeutung bimetallischer, eisenhaltiger Schichtdoppelhydroxide ist es von entscheidender Bedeutung zu verstehen, welche Auswirkungen ihr Einbau auf die Struktur und letztlich auf die katalytische Leistung hat. Die systematische Variation der Co/Fe-Zusammensetzung innerhalb der Schichten zeigt, dass die Anwesenheit von Eisen das Grafting begünstigt und dadurch strukturelle Unordnung in Form von zufälliger Zwischenschichtung und planaren Defekten hervorruft. Gleichzeitig ist ein Mindestanteil an Co in der Struktur für eine hohe katalytische Aktivität unerlässlich.

Offen bleibt die Frage, wie sich das Ausmaß des Graftings auf die Struktur-Eigenschafts-Beziehung auswirkt. Zu diesem Zweck werden verschiedene Materialien des Brucit-Typs verglichen. Es werden drei Klassen ausgewählt, die von Natur aus unterschiedliche Zwischenschichtaufbauten aufweisen, während die Schichten ähnliche Zusammensetzungen haben. Dazu gehören Metallhydroxide $M(OH)_2$ ohne Zwischenschichtanionen, geschichtete Doppelhydroxide mit freien Zwischenschichtanionen und Hydroxynitrate mit vollständig gegrafteten Zwischenschichtanionen. Diese Arbeit zeigt, dass die chemische Bindung eines Zwischenschichtanions die elektronische Struktur der Metallzentren verändern kann. Dies ist entscheidend für ihr Oxidationspotential, d.h. das Potential, bei dem sich das elektrokatalytisch aktive Zentrum bildet.

Im letzten Teil dieser Arbeit werden die zuvor gewonnenen Erkenntnisse kombiniert, um die Steuerung des Graftings im Material der gleichen Klasse zu erforschen. Der vollständig auf Eisen basierende Elektrokatalysator Mössbauerit ist dafür bekannt, dass er ein umfangreiches Grafting von Zwischenschichtanionen aufweist. Mit Hilfe eines korrosionstechnischen Ansatzes ist es möglich, seine Vorstufe Green Rust auf einer Stahlplatte als großflächige Elektrode zu erhalten und das Verhältnis von gegrafteten zu freien Zwischenschichtanionen durch die Wahl der Oxidationsmethode zu steuern. Die Steuerung des Graftings in ein und demselben Material ermöglicht diese erste systematische Studie über den Einfluss von Grafting in Mössbauerit.

Bei dieser Arbeit handelt es sich um eine kumulative Dissertation – die Ergebnisse werden daher thematisch sortiert in den angehängten Manuskripten beschrieben.

3 Introduction

This section gives a brief overview to outline the importance of energy storage technologies. Furthermore, it summarizes physicochemical key aspects of electrochemical water splitting, focusing on the OER, typical catalyst materials, possibilities for innovation, and current developments. The last section gives insights into three key research questions which form the foundation of this thesis.

3.1 The way toward renewable energies

Resolving energy and environmental issues has been perceived as the most critical challenge of the 21st century.[1] Since the early 2000s, it has become evident that rising CO_2 levels, increasing severity and frequency of natural disasters, and environmental pollution create a formidable incentive on the topic.[2] Due to the limited number of countries with rich fossil fuel reserves, its broad usage further poses the risk of economic dependency and becoming a target of geopolitical interests.[3] This circumstance has led to an impressive manifestation of this dependency and triggered a political rethinking. Almost a third of advanced economies rely heavily on just three trade partners for more than 70% of their fuel imports, which is a significant portion of their economy.[4] With a renewable energy ratio of 49.6% in the power mix (Fig. 1), the Energy Transition Index (ETI) only ranked Germany as number 15 out of 31 advanced economies regarding their energy performance. This rating includes the resilience and efficiency of generation, transmission, and progress to cleaner forms of energy.[5]

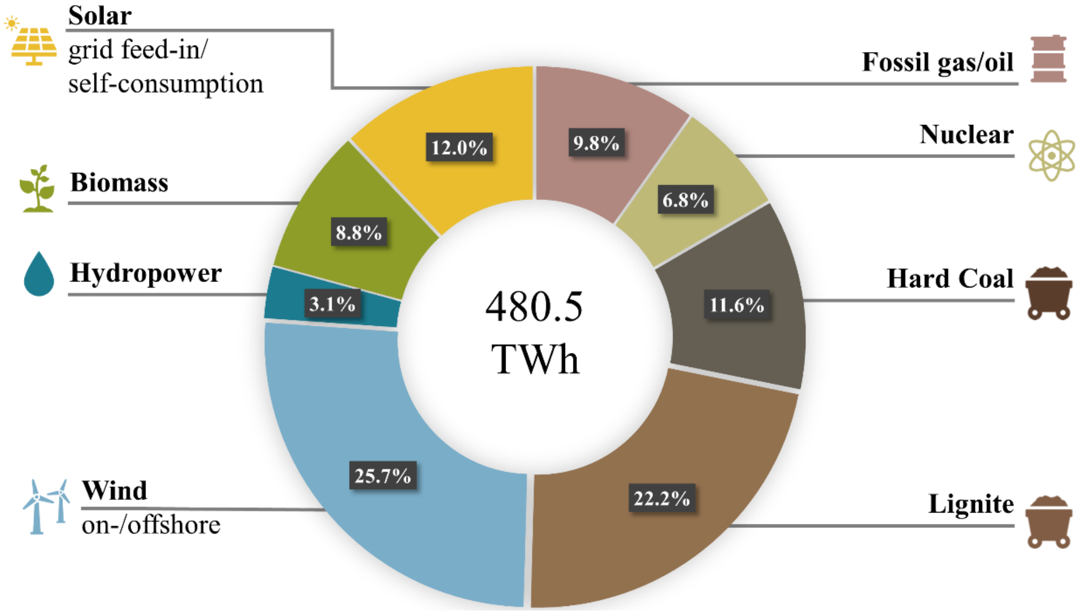

Figure 1: Net public electricity generation in Germany in the year 2022. The energy mix of Germany is still heavily reliant on fossil fuels, with the share of renewables representing less than 50%. The source data is from Fraunhofer ISE.[6]

Recent investments in green energy technologies and CO_2-neutral means of transportation have also led to the European Union's decision to ban all new internal combustion engines from 2035.[7] However, this reliance on fossil fuels ranges further than only the transport sector. Private household energy supply and the chemical, glass, and steel industries rely heavily on cheap power and chemicals from the petrol industry (e.g., hydrogen).[8] The critical aspect required to contain or even eliminate arising problems renders a transition to renewable energy sources an imperative for the years to come.

While some forms of renewable energy sources (e.g., hydropower, geothermal, or biomass plants) can run with sufficient steadiness to act as a base load supplier in the electrical grid, most sources cannot. Base-load supply implies that they operate 24/7 to meet the minimum power demand. These technologies are not designed to respond to peak demands or emergencies. Regarding conventional energy sources, coal or nuclear power plants handle this task instead. Intermediate and peaking power plants handle everything beyond this minimum power demand, which can be adjusted to the demand more easily when needed.[9]

However, it is apparent that solar and wind energy, which are typical examples of intermittent renewable energies, cannot fulfill either of these tasks in an electrical grid by themselves. Due to their output dependence on weather conditions and daily and seasonal variations, they can neither supply a steady base load nor respond quickly to meet peak power demands.[9]

Due to the intermittent character of renewable energies, coupling with suitable storage techniques is vital to ensure a continuous, secure, and demand-oriented energy supply while minimizing curtailment.[9] Thus, establishing renewable energy sources in the grid is inevitably connected to the necessity of efficient energy storage to mitigate the cyclic but often offset nature of supply and demand. Therefore, excess supply can be harvested during a power generation surplus and utilized as an intermediate or peak supplier when required. Sufficient storage infrastructure in the grid can also provide a steady base load through this coupling of energy harvesting and energy storage.[9] Ideally, storage technologies are established beyond the primary grid to meet stationary, mobile, and portable demands.

The establishment of application-oriented storage technologies entails optimization to vastly varying requirements. These different application areas quickly allow the conclusion that there is no single storage technology for all applications. Instead, all of them have their respective advantages and disadvantages. Requirements like conversion efficiency, scalability, storage/release time, transportability, acquisition and operational cost, safety, environmental friendliness, infrastructure requirements, and many more must be considered. These technologies can be categorized into five main fields (Fig. 2): Electrical (e.g., electrical double-layer capacitors EDLCs), mechanical energy (e.g., pumped hydro storage PHS), electrochemical (e.g., batteries), thermal (e.g., heat storage), and chemical storage (e.g., hydrogen fuel cells).

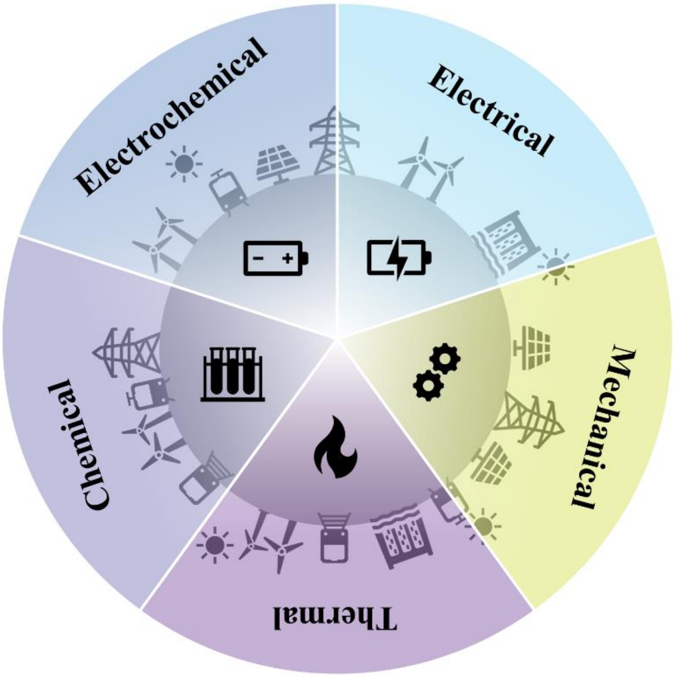

Figure 2: Overview of different categories of storage technologies. Every method has advantages and disadvantages related to efficiency, cost, applicability, and others. Adapted from Fort Frances Power Corporation.[10]

3.2 Hydrogen

Hydrogen-based storage technology belongs to the group of chemical storage, where the energy is stored in the form of chemical bonds. Hydrogen itself cannot readily be considered a clean energy source with a CO_2-neutral footprint.[11] In fact, various types, often termed colors, are differentiated. Hydrogen obtained by fossil fuels (e.g., natural gas) is considered *Grey Hydrogen* if the CO_2 generated during the production is released into the atmosphere. If it is supported by carbon capture and storage, it is termed *Blue Hydrogen*. Both cannot be regarded as sustainable energy storage.[12]

Only hydrogen, where the educts originate from sustainable sources, with the conversion energy being supplied by renewable energies and no greenhouse gas release during the production, can be termed *Green Hydrogen*.[12-13] The required infrastructure comprises two complementary processes. The first part includes converting electrical energy into chemical energy using electrolysis.[14] In the second step, this fuel can then be used directly as a reagent in the chemical industry or to convert chemical energy back into electrical energy, e.g., to support power demand in the grid or run an electric motor via a fuel cell.[14-15] While various fuel cell types exist, with their particular application area, advantages, and disadvantages, most of them share the utilization of hydrogen as their primary fuel.[15]

Due to the focus of this thesis on the generation of *Green Hydrogen* via water electrolysis, this part of the introduction aims to give an insight into the underlying challenges, setups, and benchmarks to research water electrolysis. It will focus on how to make the water splitting reaction more energy efficient, minimize losses during conversion, and make it more scalable and sustainable. Further challenges arising from the transport, medium- and long-term storage, and the utilization of a practical fuel cell will not be addressed in the scope of this thesis.

3.2.1 Thermodynamics of electrochemical water splitting

Thermodynamics tells us that splitting water in its constituents' oxygen and hydrogen is an endergonic (i.e., non-spontaneous) process. However, the reaction can proceed when an appropriate driving force, e.g., thermal energy or electricity, is provided. Using the latter for the endergonic transformation is called electrolysis, and a setup typically consists of two electrodes separated by an ionic conductor, the so-called electrolyte. Electrical work to the cell is provided via these electrodes, allowing gaseous hydrogen and oxygen production. The individual half-cell reactions and their corresponding mechanisms depend on the pH of the electrolyte.[16]

In acidic media, water splitting occurs according to the following reactions:[16-17]

Anode: $H_2O(l) \rightarrow \frac{1}{2}\,O_2(g) + 2\,H^+ + 2e^-$ $E_a^o = +1.23$ V (Eq. 1a)

Cathode: $2\,H^+ + 2e^- \rightarrow H_2(g)$ $E_c^o = +0.00$ V (Eq. 1b)

Full: $H_2O(l) \rightarrow H_2(g) + \frac{1}{2}\,O_2(g)$ (Eq. 1c)

While in alkaline conditions, it proceeds according to:[16-17]

Anode: $2\,OH^- \rightarrow \frac{1}{2}\,O_2(g) + H_2O + 2e^-$ $E_a^o = +0.40$ V (Eq. 2a)

Cathode: $2\,H_2O + 2e^- \rightarrow H_2(g) + 2\,OH^-$ $E_c^o = -0.83$ V (Eq. 2b)

Full: $H_2O(l) \rightarrow H_2(g) + \frac{1}{2}\,O_2(g)$ (Eq. 2c)

The anodic reaction (oxidation) is termed oxygen evolution reaction (OER) due to the release of oxygen gas from there, and the cathodic reaction (reduction) is called hydrogen evolution reaction (HER) due to the release of hydrogen gas. In acidic and alkaline media, H^+ ions and OH^- ions are responsible for providing charge compensation by migrating through the electrolyte during cell operation. The overall standard cell potential in both media results from the difference between the individual reaction potentials:[18]

$$E^o = E_a^o - E_c^o = 1.23\text{ V} \qquad \text{(Eq. 3)}$$

From a thermodynamic viewpoint, the amount of electricity (nFE) required at equilibrium to facilitate the reaction to split 1 mol of water can also be expressed by the change in Gibbs Free Energy (ΔG_r) of the dissociation reaction.[18]

$$\Delta G_r = -nFE \qquad \text{(Eq. 4)}$$

With $n = 2$ as the number of electrons being transferred during the electrochemical reaction, F being the Faraday constant, and E being the potential associated with reactions in the corresponding media (Eq. 1c, 2c).

For the given potentials, a standard pressure ($p^{o} = 101.325$ kPa) and standard temperature ($T^{o} = 298.15$ K) are assumed where water is liquid and the reaction products are gaseous. Thus, using literature values[18] for the Gibbs Free Energy, the thermodynamically required voltage to facilitate the electrochemical water splitting reaction results in the same as determined above from the individual half-cell reactions:[16, 18]

$$\Delta G_{r}^{o}(H_2O) = 237.22 \text{ kJ mol}^{-1} \rightarrow E^{o} = \Delta G_{r}^{o}(H_2O) / (2\ F) = 1.2293 \text{ V} \approx 1.23 \text{ V} \qquad \text{(Eq. 5)}$$

According to this solely thermodynamic point of view, the required potential would depend only on temperature, pressure, reactant concentration, and product concentration. In practice, this equilibrium cannot be reached once a current flow is involved, i.e., the electrochemical reaction proceeds at an appreciable rate. The higher the current, the greater the potential must be to maintain the flow of electrons. Consequently, this also bears kinetic implications which arise from transfer reactions, electronic and ionic conductivity limitations, and finite mass transport.[14, 17] Such phenomena give rise to so-called *overpotentials*, which are considered the irreversible part of the electrochemical reaction. They are defined as the offset of the potential of the electrode E from the reversible value E^{o} and cannot be regenerated. Thus, they are hampering the overall conversion efficiency.[16-17] Consequently, these overpotentials are regarded as a crucial evaluation criterion and design factor in evaluating the performance of new materials, which will be further discussed in chapter 3.3.

3.2.2 Oxygen evolution reaction

Practically, the overall potential required to drive the electrochemical splitting of water includes irreversible kinetic contributions from both the anodic and cathodic reactions. The HER is a two-electron transfer reaction and typically features low overpotentials.[19] A variety of different catalyst systems are reported, resulting in overpotentials as low as 27 mV for Pt on carbon.[20] Compared to the HER, the OER is subject to sluggish kinetics and thus exhibits an intrinsically lower efficiency.[21] This comparably complex reaction system originates from a coupled, multi-electron process, resulting in a higher kinetic barrier as the transfer of four electrons per O_2 is necessary to facilitate oxidation.[14, 17] Since only a single electron can be transferred with each step and various electrode surface reactions are involved, the process is forced to proceed in multiple steps with distinct intermediates. Various intermediary products are passed through depending on the employed catalyst and media.[17, 22]

Various research groups have proposed many possible mechanisms for both acidic[23] (Fig. 3) and alkaline[24] (Fig. 4) media, and the topic remains frequently discussed.[25] There exists consensus about the presence of MOH and MO intermediates, but there are discrepancies regarding the exact mechanisms, particularly related to when and from which intermediate the oxygen is released.[17] Two pathways are widely accepted. The first supposed pathway includes the formation of oxygen due to a direct reaction of two MO intermediates. Alternatively, a MOOH intermediate can form, ultimately decomposing to release O_2.[14, 17]

Acidic conditions:

$M + H_2O(l) \rightarrow MOH + H^+ + e^-$

$MOH \rightarrow MO + H^+ + e^-$

$MO \rightarrow M + ½\, O_2(g)$

$MO + H_2O(l) \rightarrow MOOH + H^+ + e^-$

$MOOH \rightarrow M + O_2(g) + H^+ + e^-$

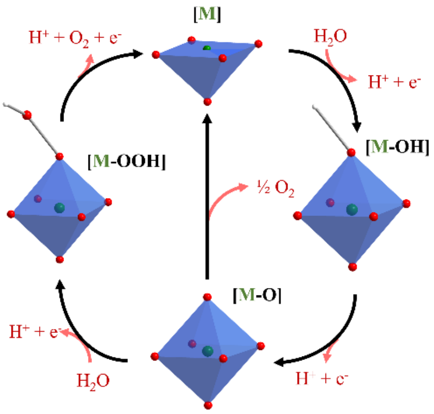

Figure 3: OER mechanism under acidic conditions.[17] Adapted from Cai et al.[14]

Alkaline conditions:

$M + OH^- \rightarrow MOH$

$MOH + OH^- \rightarrow MO + H_2O(l) + e^-$

$MO \rightarrow M + ½\ O_2(g)$

$MO + OH^- \rightarrow MOOH + e^-$

$MOOH + OH^- \rightarrow M + O_2(g) + H_2O(l) + e^-$

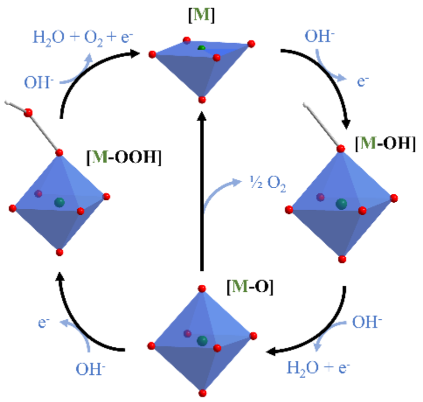

Figure 4: OER mechanism under alkaline conditions.[17] Adapted from Cai et al.[14]

While the most common application of OER is in heterogeneous catalysis, examples of homogeneous catalysis or even biocatalytic reaction also exist.[26] This circumstance renders adsorption interactions between catalysts and educts, bonding within the possible intermediates (MO, MOOH, MOH), and desorption behavior of the products from the catalyst crucial factors for the overall performance.[14, 16-17]

3.2.3 Measurement setup

The primary measurement setup to obtain crucial performance parameters is described in this section. The parameters themselves will be described in more detail in the following chapter.

Information about the catalyst system can be obtained by measuring the current passing through the electrode as a function of the applied potential over the cell. The typical testing cell consists of three electrodes, thus being called the three-electrode setup. A current is passed through the working electrode (WE) and counter electrode (CE). Changes in the working electrode's potential are measured against a reference electrode (RE) in a secondary circuit. Latter carries practically no current and thus provides a steady reference potential irrespective of the current load on the WE and CE. This constant reference potential is essential as the potential of the CE may change substantially. Due to possible alterations in CE potential, a two-electrode setup is considered unsuitable to perform such half-cell testing with sufficiently high data reliability. A typical choice for such RE is the reversible hydrogen electrode (RHE) or an Ag | AgCl | KCl electrode.[27]

Uncontrollable or severely limited mass transport can compromise accuracy and lead to non-reproducible results. Therefore, the previously described system is usually combined with a rotating disc electrode (RDE) as the WE (Fig. 5). Through rotating the electrode in solution, rather than agitating the solution by stirring or gas bubbling, efficient transport of educts to the electrode and detachment of products from the electrode can be achieved.[16, 27] The RDE is composed of a cylindrical metal rod that is embedded in an insulating cylindrical plastic holder. The outer holder usually consists of Teflon or polyether ether ketone (PEEK) due to their high chemical inertness and insulating properties. The bottom end of the electrode is attached to the respective electrode material, exposed to the solution, and polished flush with the surrounding holder. The typical electrode material for electrocatalytic investigations for the OER is glassy carbon (GC).

Therefore, the RDE setup with a GC electrode fulfills multiple important characteristics for benchmarking OER catalysts. The most important feature is the provision of a so-called uniformly accessible surface. It implies that the rate of mass transport to the surface is uniform despite the different rotational velocities depending on the distance from the center of rotation. Another fundamental property is that the flow of the solution to the surface has a laminar character up to high rotation rates, thereby underlining the possibility of obtaining highly reproducible results from RDE measurements.The electrode area typically must be minimal to reach such high stability.[27-28]

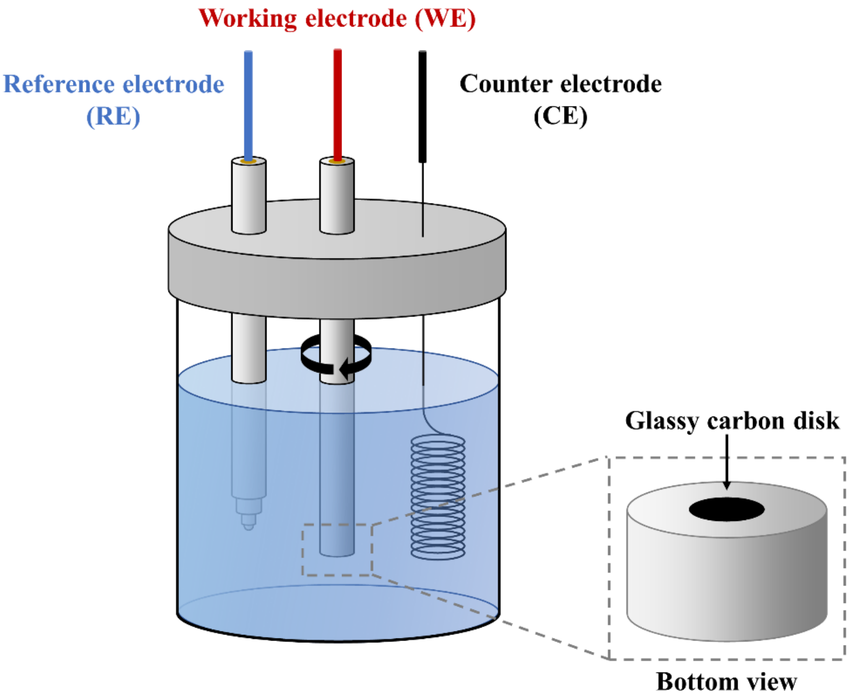

Figure 5: Typical three-electrode RDE setup for OER measurements. It consists of a working electrode (WE), a counter electrode (CE), and a reference electrode (RE). Charge flow proceeds between the WE and CE, while the potential difference is measured between the WE and RE. The WE is rotated to facilitate more effective mass transport. It has a glassy carbon bottom to apply the catalyst material.

The use of GC as the electrode material is widespread because it is highly (electro)chemically resistant at both oxidizing and reducing potentials. It features a low electric resistance and low intrinsic activity in the facilitation of the OER, thus rendering it an ideal material for the application as a current collector in benchmarking OER catalysts employing an RDE.[16, 27]

In a 3-electrode setup without an RDE, other current-collectors can also be employed, e.g., carbon cloth,[29] carbon paper,[30] nickel foam,[31] iron foam,[32] Cu foam,[33] indium tin oxide (ITO),[34] and gold.[35] Care has to be taken as the choice of substrate can significantly influence the observed activity of the respective catalysts.[36] Some can even make a notable contribution to the measured currents either through synergistic effects or dissolution and, thus, unintentional doping.[37]

A typical catalyst benchmark measurement includes the (repeated) linear variation of the potential to probe the onset of the electrochemical reaction in a 1 M KOH solution. If a single potential sweep is performed, the method is called linear sweep voltammetry (LSV), while multiple, continuous sweeps are termed cyclic voltammetry (CV). Other standard measurement techniques include the application of a constant current (chronopotentiometry, CP) or a constant potential (chronoamperometry, CA) to assess any changes in current or potential during prolonged operation.

3.3 Critical factors in catalyst development and design

Electrocatalysts facilitate electrochemical reactions such as the previously described electrochemical water splitting. In this process, they can either aid the reaction at the surface of an electrode or act as an electrode itself. The mechanism of action can be manifold such as promoting the reactant adsorption, assisting the electron transfer between the electrode and the reactant, and allowing efficient desorption of reaction products.[38]

Benchmarking corresponding catalyst materials includes kinetic performance parameters, such as the overpotential (η), Tafel slope, or behavior under long-term operation, which will be covered in this section.[39] To assess the overall versatility and scalability, economic and ecological aspects should also be considered as well due to the difficulty of transferring catalyst testing performed on the lab scale to standards demanded by industrial electrolysis applications.

Overpotential

The overpotential (η) is one of the most widely used indicators to evaluate an electrocatalyst's performance.[40] Ideally, for an electrochemical reaction, the required potential to facilitate the reaction should equal the potential of the reaction at equilibrium. Nevertheless, this idealized view breaks down once additional resistances of the wiring and kinetic hindrances due to multi-electron transfer reactions, bubble overpotential (i.e., impeded desorption of products from the electrode/catalyst surface), and ionic transfer resistances are considered. In practice, the applied potential is much higher than the equilibrium potential (E^o = 1.23 V), primarily due to the kinetic barriers of the reaction.[14]

The overpotential quantifies the collective contribution of such. It defines the difference in potential between the half-cells thermodynamically determined potential E^o and the experimental observation of the redox event E (Eq. 6).[41]

$$\eta = E - E^o \qquad \text{(Eq. 6)}$$

Thus, it quantifies at which relative potential a specific electrocatalytic activity can be observed for a target reaction. This definition raises the necessity to state how great this activity should be relative to the catalyst mass or the area covered by the catalyst. Therefore, an area-normalized current (i.e., current density) is typically used to quantify the rate of the reaction. The overpotential is then reported at a value of 10 mA cm^{-2}.

In practice, both the OER and the HER feature an overpotential η_a and η_c, respectively. For previously discussed reasons (chapter 3.2.2), the contribution of the HER is often negligible compared to the one of the OER. The practical, complete overpotential of an electrolyzer resembles the joint contribution of both η_a and η_c (Fig. 6), while for investigative purposes, the two contributions can be investigated separately in the discussed three-electrode setup.

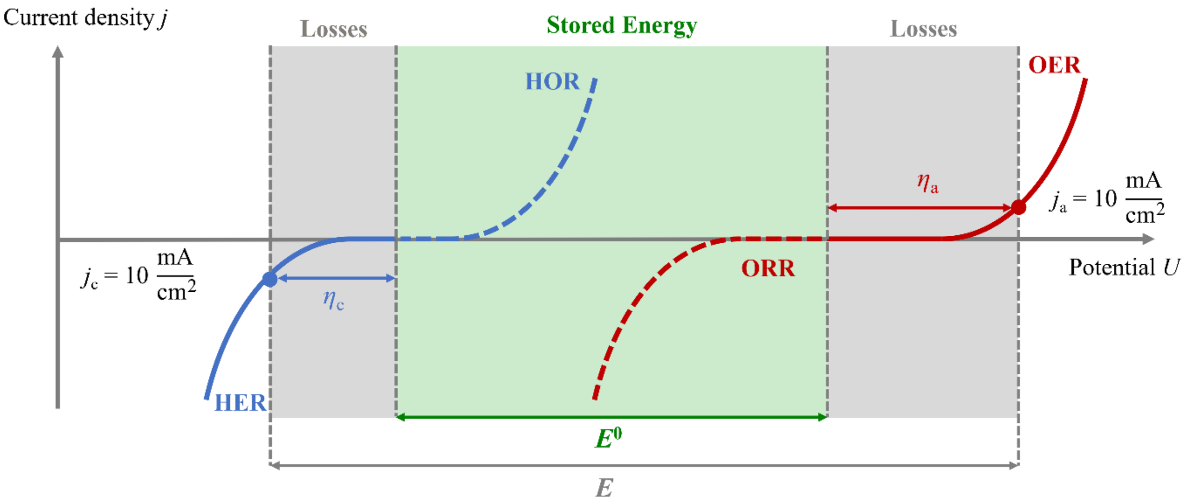

Figure 6: Depiction of the anodic and cathodic processes during the electrochemical water splitting. The hydrogen evolution reaction (HER, —) runs at the anode, while the oxygen evolution reaction (OER, —) is facilitated at the cathode. The corresponding reverse processes are the hydrogen oxidation reaction (HOR, ----) and the oxygen reduction reaction (ORR, ----). The potential E is greater than the electrochemical standard potential E^o and is required to drive the reaction. This higher potential is necessary due to the overpotentials of the HER (η_c) and OER (η_a). These are recorded at an electrode current of 10 mA cm^{-2} and represent an irreversible loss.

Tafel slope

For practical applications, operating the electrolyzer at high current densities is necessary. Faraday's law of electrolysis describes that the molar quantity of reaction products is directly proportional to the amount of total electric charge passed through the electrode during the reaction. Electric current resembles the number of charges passing in a specific time; therefore, it should be high to facilitate a fast turnover.[18] Since higher currents are subject to greater overpotentials, it is desirable to have catalysts that only feature a shallow increase in overpotential when increasing the current density. This property is described by the Butler-Volmer equation, which can be simplified into the more elementary form of the Tafel equation (Eq. 7).[17-18]

$$i \approx i_0 \exp\left(\frac{\alpha n F \eta}{RT}\right) \qquad \text{(Eq. 7)}$$

The parameters i and i_0 represent the current and the exchange current, respectively. The parameter α expresses the anodic transfer coefficient, and n is the number of transferred charges. The temperature is designated by T, R is the universal gas constant, and F is the Faraday constant. Logarithmic translation of the Tafel equation yields a simple form in which voltammetry data can be plotted (Eq. 8).[17-18]

$$\eta = b \cdot \log\left(\frac{i}{i_0}\right) \qquad \text{with} \qquad b = \frac{\partial \eta}{\partial \log(i)} = \frac{2.303RT}{\alpha F} \qquad \text{(Eq. 8)}$$

The Tafel slope b indicates how fast the overpotential increases with the current i. It is typically given in mV/dec expressing the build-up of overpotential when the current is stepped up by one decade. Consequently, a smaller Tafel slope represents better electrocatalytic properties due to fewer irreversible losses.

Long-term stability analysis

Besides the initial activity of an electrocatalyst, the versatility of a catalyst material also expresses itself by its performance under permanent load. To assess this property, it is required to perform long-term stability measurements. This investigation can be performed in either two modes – while applying a constant current (chronopotentiometry), where the change in potential is observed, or under a constant potential (chronoamperometry), where the alteration of the current is measured. The decisive difference compared to linear sweep voltammetry (LSV) and cyclic voltammetry (CV) analysis is that the material is subjected to a constant current/potential over a prolonged time ranging from hours or sometimes even days.[21b] This aids in assessing the presence and severity of aging under operation and is one key parameter to rate the versatility of catalysts for industrial use.

Post-mortem analysis

A secondary sphere to derive information about the employed catalysts involves a structural assessment after the catalytic experiments. Post-mortem analysis is a versatile step in the development process that comprises several techniques. Firstly, the catalyst itself can be investigated for structural changes.[42] These can be induced by intrinsic restructuring to a more stable phase under the given conditions,[43] through the incorporation of ions from the electrolysis solution,[44] or through a loss of material during operation.[45] These alterations often lead to a change in morphology and potentially a loss of active sites.[46] However, in other cases, an initial restructuring can also lead to the in-situ formation of a more stable and active catalyst.[47] Thus, a detailed analysis is necessary to identify the active catalyst phase. These investigations are typically performed using bulk techniques (e.g., powder X-ray diffraction; PXRD), surface techniques (e.g., X-ray photoelectron spectroscopy; XPS), and methods to determine changes in morphology (e.g., scanning electron microscopy; SEM), or by determining material loss to the electrolyte (inductively coupled plasma atomic emission spectroscopy; ICP-AES).[21b, 48]

Economic and ecologic aspects

Like many lab-scale experiments, they are not routinely scalable for commercialization. As the eventual goal for catalyst development is an industrial application, research must also be designed to meet these demands and requirements.

Experiments are almost exclusively performed on the previously introduced RDE (chapter 3.2.3). It aids in alleviating several limitations during the measurement but does not resemble a scalable setup. At low current densities like 10 mA cm^{-2}, effects of catalyst degradation, educt transport limitations, and gas evolution are kept to a minimum. Still, this current density is relatively low considering that commercial alkaline electrolyzers typically operate at 100-400 mA cm^{-2} and sometimes even up to 2 A cm^{-2}.[49] Although the turnover increases when choosing higher current densities, efficiencies drop. The operating conditions of the electrolyte significantly differ from the lab scale. While small-scale experiments employ a 1 M KOH solution, commercial electrolyzers utilize a 6.5 M-7.8 M (25-30 wt-%) KOH solution at temperatures typically between 5°C and 100°C and pressures ranging from 25-40 bar.[49a]

The development of catalyst systems cannot merely focus on performance but should also consider other industry-relevant requirements. The electrodes should be producible on a large scale with high uniformity, at an affordable cost, and eventually, allow for long-term operation to avoid the frequent exchange of the electrode. Particularly the anodic side exposes the catalyst to a highly corrosive environment, which often compromises the stability leading to irreversible phase changes or dissolution, thus hampering the catalytic activity.[14, 50] Therefore, it is desirable to resort to non-toxic, abundant, and recyclable materials that can either be reused or where catalytic capabilities can be restored. Catalysts featuring a complex preparation route or catalysts relying on expensive educts are unsuitable for commercial applications.[14, 50]

3.4 Materials for OER

To mitigate the high overpotentials of the OER and thus increase the efficiency when considering the energetic perspective of employing the technology as an energy storage technology, various catalyst material classes have been extensively investigated. Studies focus on how to improve electrode kinetics and stability in different environments.[38, 51]

One class exhibiting excellent OER activity in acidic and alkaline media are so-called noble metal-based catalysts (NMBCs). For instance, rutile-type RuO_2 and IrO_2 exhibit high activity in the OER catalysis but suffer from intrinsic drawbacks that hamper their applicability. Both are highly unstable under elevated anodic potentials due to the extremely oxidizing environment. RuO_2 undergoes oxidation to RuO_4, which ultimately dissolves into the electrolyte solution.[17] This loss of catalyst inevitably results in a loss of activity. Although more stable at high anodic potentials in both acidic and alkaline electrolytes, the use of IrO_2 entails a similar issue where the catalyst undergoes oxidation to IrO_3 before also being subject to dissolution. They are also composed of noble metals, making such materials impractical and undesirable for large-scale applications in industrial processes.[17]

To deal with these intrinsic drawbacks of the presented NMBCs, the search for viable, low-cost transition metal-based catalysts has raised increasing attention to be used under alkaline conditions. They have proven to exhibit both satisfactory intrinsic activity and stability for the OER.[52] As this thesis covers the alkaline OER, only the relevant materials for this medium will be discussed in the scope of this chapter. Popular investigated electrocatalysts include Co-, Ni-, Fe- and Mn-containing materials demonstrating the possibility of replacing NMBCs. These include Ruddles-popper oxides,[53] rock salt oxides,[54] rutiles,[55] high-entropy alloys,[56] perovskites,[57] metal oxides,[58] spinels,[59] layered double hydroxides (LDHs),[60] and hydroxides.[61] Most notably, LDHs have shown outstanding OER performances, straightforward synthesis routes, and a wide range of further improvements.[62]

Due to their unique structural and compositional features to facilitate the OER, this chapter will introduce brucite-like layered materials in more detail. Here, a particular focus will lay on LDHs and hydroxynitrate salts to cover various aspects regarding their compositional possibilities, structural constitution, and electrocatalytic capabilities.

3.4.1 Layered Double Hydroxides (LDHs)

3.4.1.1 Structure

In general, the compositions of LDHs can be described by the generic formula $M^{2+}_{1-x}M^{3+}_{x}(OH)_2(A^{n-})_{x/n} \cdot z\ H_2O$. The crystal structure is composed of edge-sharing octahedral sheets with divalent (M^{2+}; e.g., Ca^{2+}, Ni^{2+}, Mn^{2+}, Co^{2+}, Fe^{2+}) and trivalent metal cations (M^{3+}; e.g., Al^{3+}, Cr^{3+}, Mn^{3+}, Fe^{3+}, Ga^{3+}, Co^{3+}, Ni^{3+}) with similar ionic radii and hydroxide ligands extending into the interlayer space.[23a, 62f, 63] Structurally, they resemble brucite-like ($Mg(OH)_2$) layers, whereas the isomorphic substitution of M^{2+} with M^{3+} generates an excess charge. Anions in the interlayer space compensate for this additional charge (A^{n-}; e.g., NO_3^-, SO_4^{2-}, CO_3^{2-}, Cl^-).[23a, 63a, 63b] The ratio ($x = 0.17$-0.33) of M^{2+}/M^{3+} can be varied within certain boundaries,[64] but a ratio of 2:1 ($x = 0.33$) is generally assumed to be the most favorable composition.[65] The individual layers are held together by electrostatic interactions and hydrogen bonds between the brucite-like layers and the interlayer anions, forming the three-dimensional structure (Fig. 7).[66]

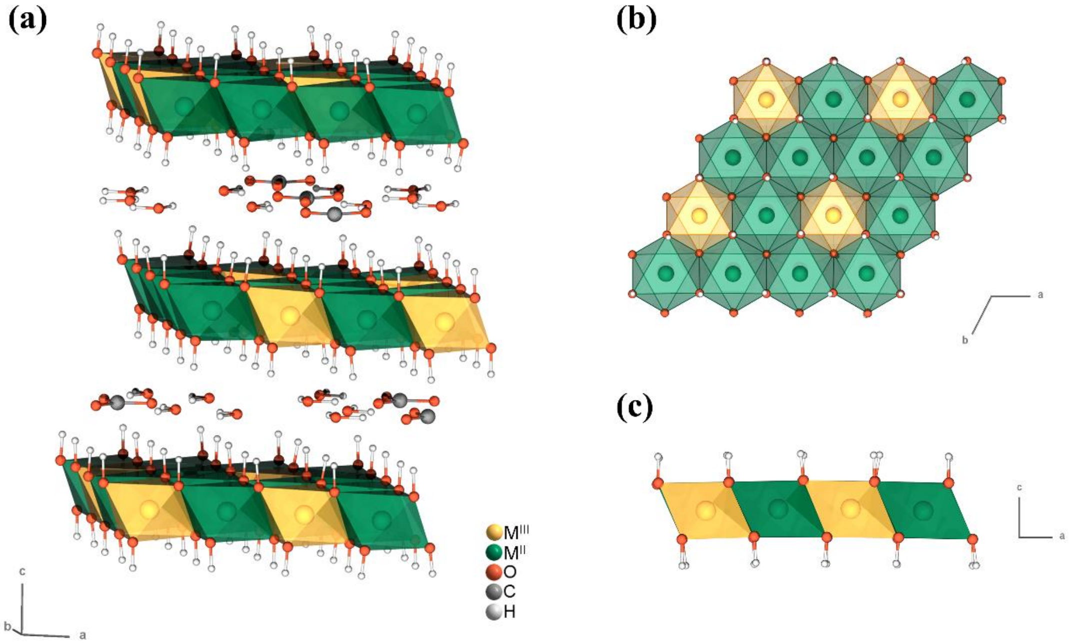

Figure 7: (a) Schematic visualization of the layered structure of a bimetallic carbonate LDH of the fougèrite group. Interlayer anions and water separate the layers. (b,c) The layers are composed of M^{2+} (green) and M^{3+} (yellow) being octahedrally coordinated by hydroxide ligands. The figure is based on the reported crystal structure of Dionigi et al. for a NiFe-CO_3 LDH.[67]

Various synthetic methods have been applied to obtain LDHs, with the most widely known being coprecipitation. Conditions can vary significantly from precipitation at low or high supersaturation, with separate nucleation and aging steps, or via an urea hydrolysis route.[68] The ion exchange method[69] is chosen when the primary metal ions react with the desired interlayer anion or when they are unstable in an alkaline solution. Other methods include the rehydration of mixed-metal oxides, hydrothermal synthesis, electrodeposition, sol-gel approaches, or more specialized strategies.[68]

However, most LDHs can be obtained by relying on a one-step precipitation synthesis where the divalent metal-ion might undergo further oxidation by atmospheric or dissolved oxygen when susceptible to oxidation.[63c] While versatile for some LDHs, this oxidation can be a considerable obstacle when, for instance, obtaining pure iron LDHs without any side phases.[70] This issue will be further discussed in section 3.4.1.3.

3.4.1.2 Application in OER catalysis

The first metal hydroxide identified to exhibit catalytic capabilities with respect to the OER was α-$Ni(OH)_2$.[71] Further investigations revealed that doping with other suitable metal cations further improves the electrocatalytic OER activity.[44, 72] Since then, also transition metal-based LDHs[73] (e.g., containing Mn, Fe, Co, and Ni) and their topotactic derivatives[74] (e.g., oxyhydroxides) have been further investigated. Their excellent OER capabilities originate from their highly controllable structure[75], intensive host-guest interactions[76], and highly dispersed single-atomic sites.[62f, 77] The performance of such bimetallic, transition metal-based LDHs as OER catalysts can be evaluated by comparing their respective overpotential and Tafel slope (Fig. 8).[70, 78]

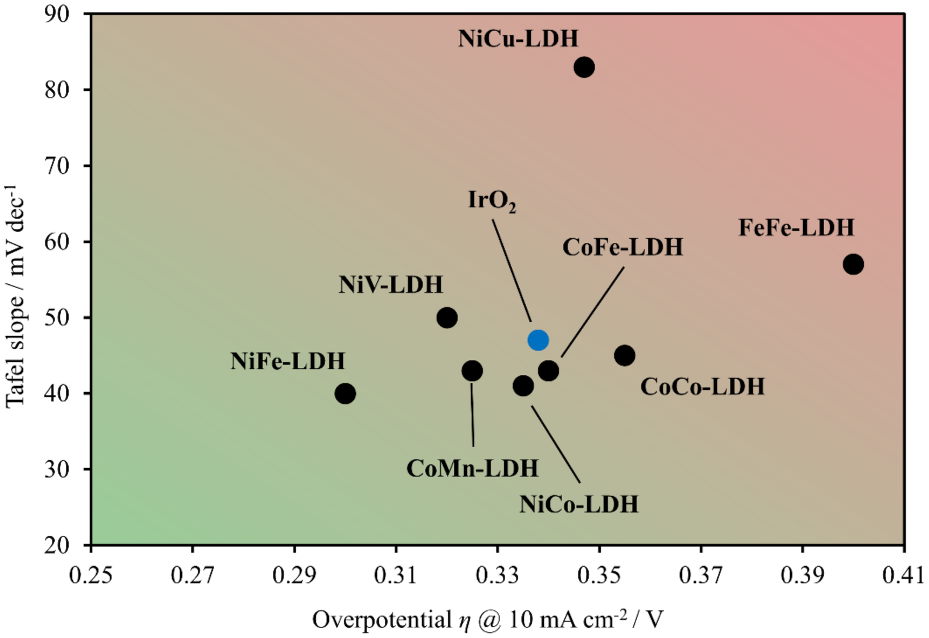

Figure 8: Tafel slope and overpotential of representative studies for a given transition metal combination in LDHs.[70, 78] The IrO_2 benchmark (blue) performance is shown as a reference. The best-performing catalysts are located on the bottom left of the plot, while the ones with inferior performance are on the top right.

The choice of transition metals for LDHs is mainly focused on those with high redox activity. Therefore, combinations of $Fe^{2+/3+}$, $Ni^{2+/3+,}$ and $Co^{2+/3+}$ metal cations are extensively researched.[62f, 63c, 63d] Among those, NiFe-LDHs excel with high activity and stability and are qualified for use as a cost-effective material for large-scale utilization. Despite the impressive catalytical capabilities, the active site of the material was subject to controversial discussion.[62f] The earliest studies suggested that the Ni atoms are the origin of the high OER activity, while Fe was acknowledged to increase the acidity of OH_x moieties coordinating with the Ni centers. Thereby, the reduction potential for the $Ni^{3+/4+}$ couple can be lowered, increasing the population of Ni^{4+} and thus aiding the OER activity.[79] Later results indicate that surface Fe exhibited lower overpotentials leading to the conclusion that these should be the active centers.[80] However, oxyhydroxides with more than 55 at-% of Fe have failed to show any attractive OER activity.[62a] In fact, density functional theory (DFT) investigations indicated that the OER overpotential of a single Fe site is considerably higher than experimental data suggests.[62a, 62f] In-operando Mössbauer spectroscopy studies indicated that the formation of localized Fe^{4+} is the reason for the observed performance, while surrounding Ni-ions exhibit a stabilizing effect.[81] Thus the synergistic interaction between Fe and Ni in NiFe-LDHs is the reason for the excellent OER performance.[23a]

Other possibilities for further optimization have been explored, including nanostructuring, vacancy creation, partial cation substitution, hybridization with conductive material, and anion replacement.[63c]

Nanostructuring aims to increase the number of active sites, facilitate a more efficient electrolyte diffusion, adsorption of educts, and desorption of products.[14, 82] This can, for example, be achieved by exfoliation and utilization of LDH nanosheets as the respective OER catalysts.[78a] It is important to note that the higher number of active sites does not only originate from a higher surface area. It is consensual knowledge that the edge sites dominate the OER performance in bulk, and there are only minor contributions from defect sites in the basal plane.[83] However, the exfoliation process introduces additional defects that contribute to OER performance. Concomitantly, different etching techniques can also be used to purposefully create vacancies and provide additional active sites in the same manner.[60b, 63c, 84]

Another approach resembles the transition from bimetallic to trimetallic LDHs, which aims to increase the number of OER active sites in the catalyst material.[85] Due to the intrinsically low conductivity of LDHs, increasing the number of active sites alone is insufficient to boost the performance significantly. Therefore, strategies aim to composite them with conductive material, grow LDH on them, or create heterostructures.[63d, 86] Anion replacement impacts the widening of the interlayer space, potentially increasing the number of accessible active sites and improving OER performance by modifying the electronic surface structure of the catalyst.[63a, 87]

Despite the apparent focus on performance aspects, it is essential to reconsider the economic and ecological aspects discussed previously. From this viewpoint, the use of Ni and Co should be considered carefully due to competing interests in the material with the manufacturing industry of Li-ion batteries. Especially the use of Co, which is toxic and bears geopolitical risks, has to be seen critically as more than half of the worldwide Co is produced in the Democratic Republic of Congo under hazardous and socioeconomically questionable working conditions.[88] These circumstances have created a research interest in the exclusive use of inexpensive and abundant iron in OER catalysis.[89] One example is the all-iron oxyhydroxide mössbauerite derived from an LDH, which will be further introduced in the next section.

3.4.1.3 All-iron OER catalyst: Mössbauerite

Besides high-performance catalysts from the LDH family, its compositional richness also allows access to a cost-efficient and green catalyst material based only on inexpensive and abundant iron. Usually, Fe-based alkaline OER catalysts are mainly subject to high overpotentials or dissolution.[90] The unique structural advantages of LDHs allow the synthesis of the mixed-valence mineral green rust (GR) with an idealized formula of $Fe_4^{2+}Fe_2^{3+}(OH)_{12}CO_3 \cdot 3\,H_2O$. Unfortunately, structural Fe^{2+} species are prone to oxidation at ambient oxygen fugacity. Thus, aerial or dissolved oxygen triggers the oxidation from Fe^{2+} to Fe^{3+}. This reaction induces the transformation into various ferric oxyhydroxides like goethite, feroxyhyte, and lepidocrocite.[70] If the oxidation is performed through a quick and defined chemical process using H_2O_2, the oxidation has been shown to yield the ferric oxyhydroxide and OER catalyst mössbauerite (GR*) $Fe_6^{3+}(O)_4(OH)_8CO_3 \cdot 3\,H_2O$. The oxidation reaction proceeds topotactically, and deprotonation provides the required charge compensation.[29b] The carbonate ions, which are situated in the interlayer space, stabilize the structure.[70] With an overpotential of 400 mV at 10 mA cm^{-2}, the catalyst is not competitive with high-performing mixed-metal transition-metal LDHs (Fig. 8), but efficiently boosts the low activity of iron-only catalysts through incorporation in this particularly beneficial layered structure.[70] Mössbauerite exhibits additional structural peculiarities worth investigating concerning the structure-property relationship.

A detailed characterization of the mössbauerite structure is indispensable to understand why – despite the topotactic nature of the transformation – the diffraction pattern of GR* features less and significantly broadened reflections compared to GR.[70] As typical for layered materials, massive defects hamper the understanding of the real structure and, thus, the structure-property relationship of brucite-type compounds in general. DFT calculations have shown that upon oxidation of the mixed-valent precursor GR to GR*, bonding of the interlayer anions to the octahedrally coordinated Fe^{3+} species is triggered.[91] This phenomenon, termed "grafting", has been described for several anionic species such as carbonates[92], phosphates[93], molybdates[94], and chromates[95] in various systems. The process proceeds exothermically for the oxidation of GR to GR*, thus resembling the driving force of this spontaneous bonding to the layers.[91] Investigations conclude that in mössbauerite, both carbonate species, grafted to the layer and free in the interlayer space, are present. The arrangement of these, however, is not systematic and expresses itself in a random interstratification of layers with various grafting degrees. Thus, the material can only be described in a model composed of random interstratification and turbostratic planar disorder.[91]

3.4.2 Nitrate double salts

3.4.2.1 Structure

Hydroxy double salts (HDS) are closely related to LDHs. Synonymous terms include basic salts and layered hydroxide salts.[96] Their composition can be expressed as $[(M^{2+}{}_{1-x}, M^{2+}{}_{1+x})(OH)_{3(1-y)}]A^{n-}{}_{(1+3y)/n} \cdot z\, H_2O$.[96b] They are composed of divalent metal ions (M^{2+}) octahedrally surrounded by hydroxide ions, resembling a structural derivative of the brucite structure (Fig. 9).[96c] The denoted M^{2+} ions can either be the same or different ionic species. In this case, however, only a difference of 0.05 Å in ionic radii *r* is tolerated, which resembles a lower tolerance than that for LDHs.[97] The most common mono-ionic HDSs include compounds based on Zn^{2+} (r = 0.74 Å), Ni^{2+} (r = 0.69 Å), Co^{2+} (r = 0.72 Å), and Cu^{2+} (r = 0.72 Å). The respective bimetallic materials also exist as long as the previously stated rule of ionic radii difference is satisfied.[97] The interlayer anion can either be monovalent, such as Cl^-, NO_3^- or CH_3COO^-, or divalent, such as SO_4^{2-}, or CO_3^{2-}.[96b, 98] Notably, this interlayer anion is bound directly to the metal ion, thus defining the structural identity. This grafting phenomenon was also found for some LDHs described in the previous chapter.[91-92] HDSs form layered structures, with either a planar layer arrangement or layers with vacancies where the metal ion is relocated in a tetrahedral position, thus expressing the relation to LDHs and the parent brucite. [96c, 97, 99] The latter vacancy-type arrangement is often found for Zn or Zn-rich compounds and is an exception as it does not exhibit this grafting characteristic.[100]

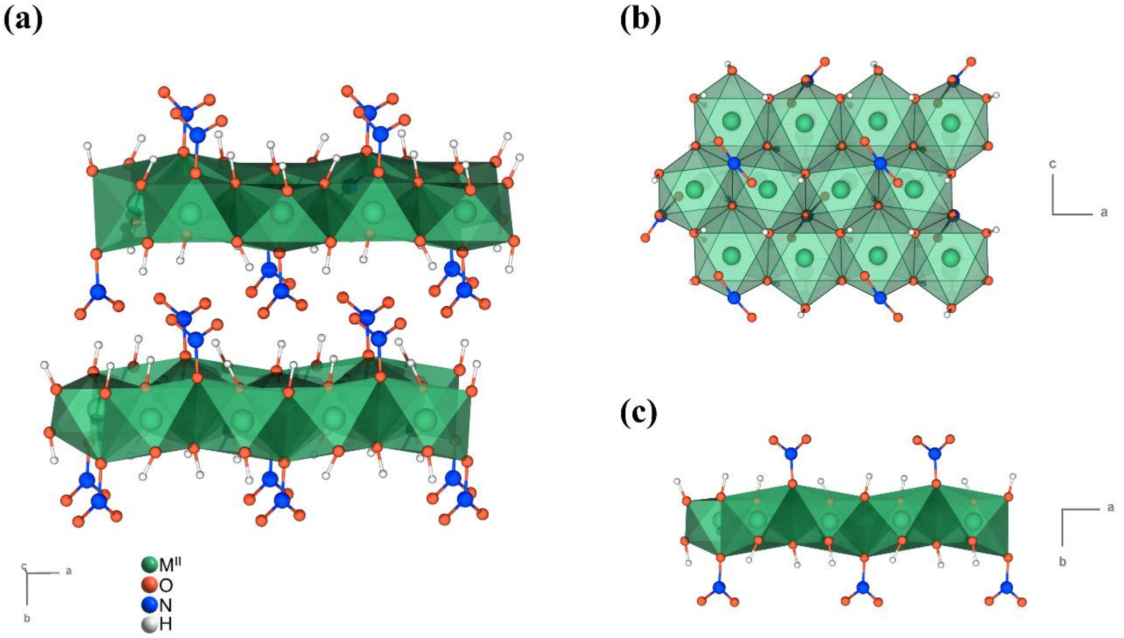

Figure 9: (a) Schematic visualization of one possible layered structure of a nitrate HDS. The layers are separated by interlayer anions, which are grafted to one layer. (b,c) The layers are composed of M^{2+} (green) octahedrally coordinated by hydroxide and nitrate ions (blue). The graphic is based on the reported crystal structure of Bovio et al. for $Cu_2(OH)_3NO_3$ (gerhardite).[101]

The structural richness, particularly for Co, Ni, and Cu HDS is well investigated, and various synthetic methods have been presented in the literature.[102] The most versatile route is simple alkaline precipitation by adding a base to a metal-salt solution containing the desired metal and anion.[103] Other synthesis methods include the reaction of a soluble metal salt with an insoluble oxide,[104] electrosynthesis,[105] mechanochemical synthesis,[106] hydrothermal synthesis[107], or via urea hydrolysis[103b, 108]. The latter method works by inducing the precipitation through a constant release of NH_3 and the subsequent slow pH increase.

3.4.2.2 Application in OER catalysis

Unlike transition metal-based hydroxides, oxyhydroxides, and LDHs, HDS have received less attention as OER catalysts. Reports include Co-hydroxycarbonate on carbon paper (η = 240 mV at 10 mA cm^{-2})[109] or Ni-foam (η = 332 mV at 10 mA cm^{-2})[110], CoZn-hydroxysulfate (η = 370 mV at 10 mA cm^{-2}) [111], and CoMn-hydroxycarbonate on Ni-foam (η = 294 mV at 30 mA cm^{-2}).[112] Among all investigated catalysts, Ni-hydroxynitrate on Ni-foam exhibited the lowest overpotential (η = 231 mV at 50 mA cm^{-2}) reported for hydroxy double salts.[113]

Analogous to the strategies elaborated for LDHs, the improvement of the HDS usually aims to utilize the compositional flexibility and move from mono-metallic catalysts to compounds employing two different transition metals. This incorporation can happen either through small-scale doping or by replacing a significant amount of the divalent cation with another.[114] Other approaches aim to deposit them on a conductive or high-surface-area substrate to boost electrical conductivity and the accessible surface area.[114b, 115]

While care should be taken when investigations are performed on substrates other than a GC to avoid additional contributions (chapter 3.2.3), the material class has been proven to be a versatile candidate for further development. However, the origin of the electrocatalytic activity regarding the structure-properties relationship, similarities, and differences to other brucite-type catalysts has been mostly disregarded.

3.5 Scope of this Thesis

The motivation for this work was to gain a deeper understanding of the OER electrocatalyst structure-performance relationship to develop efficient energy storage technologies based on green hydrogen. Employing innovative strategies, current research aims to develop efficient, environmentally friendly, and scalable methods to store the energy harvested from renewable resources. Here, different 2D electrocatalyst systems were further investigated. Particular attention was paid to structural details resulting from the interaction between the interlayer anion and the layer through grafting. This effect has not been systematically studied with respect to its impact on the electrocatalytic capabilities of the given materials. The major incentive of the performed studies was to elucidate how catalysts can be tailored not only with a focus on efficiency but also towards sustainability and applicability.

A stepwise approach ensures the correct understanding of what these alterations look like and which consequences they imply for the structure and performance. For this purpose, the presented investigations dealt with three key questions, further outlined in chapter 4.

Grafting represents a versatile parameter to tailor electrocatalysts' capabilities. The chemical bonding of interlayer anions not only results in structural alterations but also influences the electronic structure, which is similarly responsible for the activity of the OER catalyst. While it is known that grafting is triggered in mössbauerite,[70] the influence of iron incorporation in other LDHs has only been investigated from a purely electrocatalytic point of view. Therefore, connecting the LDH composition with the observation of grafting and the catalytical properties is necessary to conclude on the structure-property relationship.

- What are the structural and electrochemical effects of Fe incorporation and, thus, the Co/Fe ratio in CoFe-LDHs?

Despite the structural similarities of brucite-type materials, they all feature vastly different electrocatalytic properties. A decisive difference between such layered hydroxides, layered double hydroxides (LDH), and hydroxy double salts (HDS) is the interlayer anion's presence and binding mode. To derive conclusions on the effect of interlayer anion grafting, it is thus crucial to investigate different members of this material family and compare them regarding their structural peculiarities and properties.

- How does the interlayer anion binding state influence the OER activity in different brucite-type materials?

To further improve the capabilities of a catalyst, the previously gained knowledge about the beneficiary of grafting can be combined to control the extent of grafting within the same material class. Particularly for a material very prone to grafting, i.e., mössbauerite, it is crucial to control the grafting behavior of interlayer anions by influencing the driving force for this reaction.

- Can modulation of the synthetic procedure influence the presence of grafted and ungrafted interlayer anion species in mössbauerite? How does it impact the structure and the electrocatalytic capabilities of the material?

4 Synopsis

The presented cumulative thesis consists of three publications (Fig. 10). These pick up the key questions stated in chapter 3.5. The first focuses on the effect of Fe-content in CoFe-LDHs from a structural and electrocatalytic point of view. The second work deals with the effect of interlayer anion grafting and its influence on the observed catalytical performance of the material. In the third publication, the previous knowledge is applied to obtain the iron-only electrocatalyst mössbauerite with different degrees of grafting via an electrochemical route.

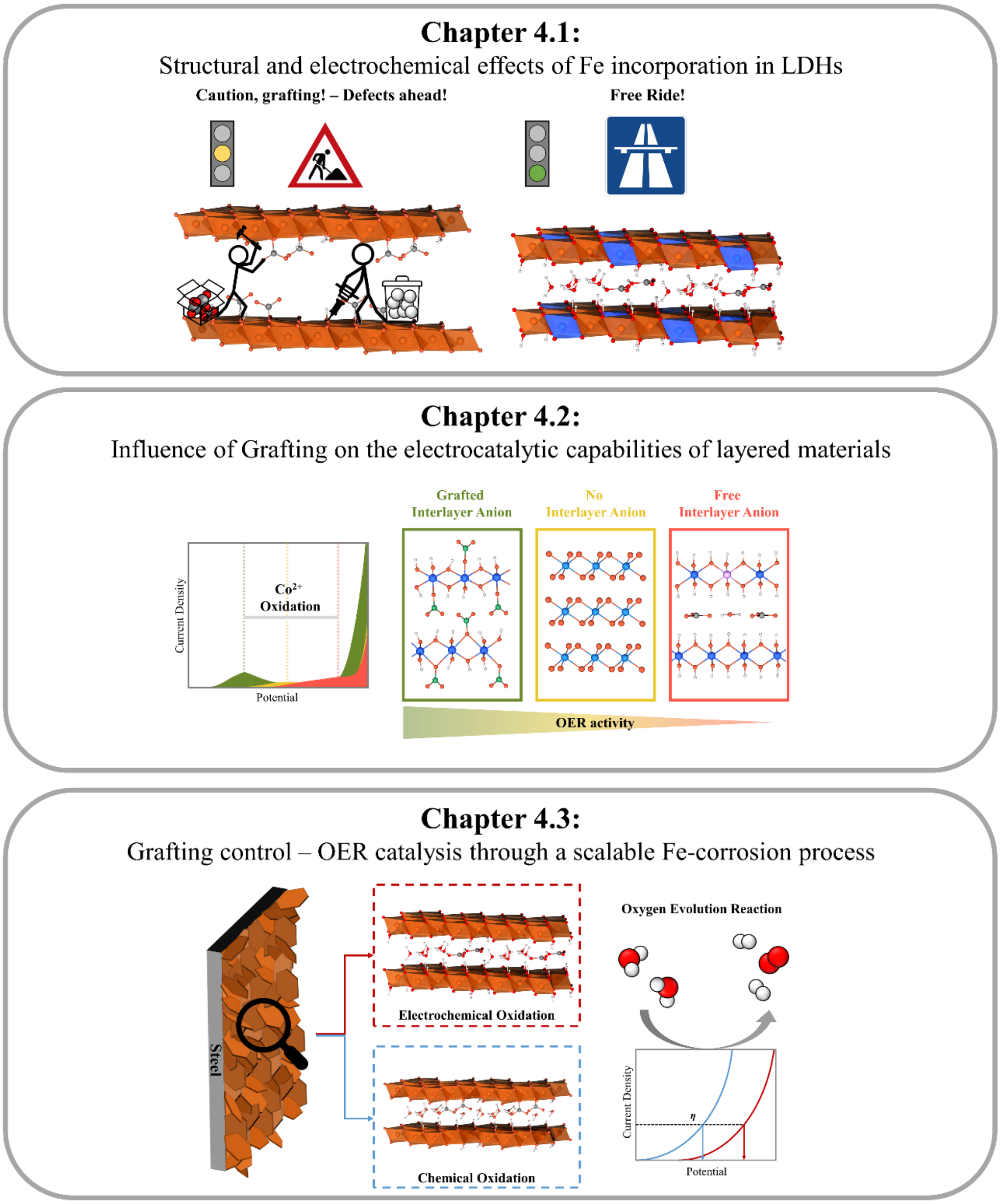

Figure 10: Graphic synopsis of all presented publications of this cumulative thesis.

In **chapter 4.1**, the successful synthesis of a variety of compositions of CoFe-LDHs is described ranging from Fe-poor (33.3 at-%) to Fe-rich (83.3 at-%) samples. In terms of structure, the publication finds that the oxidation of mixed-valence Fe-LDHs triggers partial grafting of interlayer carbonate to the brucite layers. The study indicates that a minimum of 20% of Co is required in these structures to obtain high current densities up to 200 mA cm^{-2} at potentials below 1.7 V. Based on these experimental findings, underlined by preceding theoretical investigations,[91] it is apparent that grafting can play a crucial role in OER catalysis.

The study performed in **chapter 4.2** provides a more in-depth analysis of this effect in the scope of a systematic study of brucite-type layered compounds. For this purpose, both Co- and Ni-based materials from this class are investigated. The work includes the corresponding metal hydroxides $M(OH)_2$ without an interlayer anion, LDHs with free interlayer anions, and hydroxynitrates with fully grafted interlayer anions. The investigations confirm that Ni- and Co-hydroxynitrates display notably earlier formations of the electrocatalytically active species, and particularly Co-hydroxynitrates exhibit lower overpotentials (0.34 V at 10 mA cm^{-2} and 0.40 V at 100 mA cm^{-2}) than their other brucite-type relatives.

Chapter 4.3 presents a scalable, cheap, and time-efficient route to prepare the all-iron OER catalyst mössbauerite on steel. The preparation is based on an electrochemical corrosion process to obtain the mixed Fe^{2+}/Fe^{3+} precursor green rust. The subsequently used oxidation method to obtain the ferric mössbauerite determines the degree of interlayer anion grafting. Apparent differences in interlayer spacing and the change of observable stacking disorder indicate that grafting can be reduced using an electrochemical oxidation route. The direct deposition of the OER catalyst onto a steel plate, which acts as an iron source and the current collector, allows it to outperform the bare steel substrate. The obtained material can reach 100 mA cm^{-2} at potentials of 1.82 V and 1.84 V, depending on the degree of grafting.

4.1 Structural and electrochemical effects of Fe incorporation in LDHs

As discussed in chapter 3.4.1, the class of LDHs exhibits high flexibility toward substitution patterns and enables the partial replacement of metal ions. These properties allow for the systematic variation of their composition and their respective oxidation products, the oxyhydroxides. For the mixed-valent all-iron LDH green rust, previous studies indicated that oxidation triggers partial grafting of interlayer carbonate to the brucite-like layers.[91] The iron in the layers favors the occurrence of this grafting process, inducing major stacking disorder observed through non-systematic peak broadening and an irrational *00l*-series. Therefore, it is sensible to assume that partial grafting will also be triggered above certain iron contents in mixed-metal LDHs known for their versatile OER catalytical capabilities.

To investigate the structural changes and the variation in OER activity, different Co/Fe ratios were screened in carbonate LDHs. In terms of composition, the thermodynamically most stable LDH composition of M^{2+}:M^{3+} = 2:1 was chosen, where a dense packing of flat-laying carbonate anions in the interlayer was achieved.[65] To strictly stick with this composition even at different Co/Fe ratios, both divalent and trivalent Fe-species were used, resulting in LDHs having the general composition of $[M^{2+}_{6-x}M^{3+}_{x}(OH)_{12}](CO_3^{2-})_{x/2} \cdot n\,H_2O$ with $M^{2+} = Fe^{2+}$, Co^{2+} and $M^{3+} = Fe^{3+}$. To eliminate the influence of uncontrolled aerial oxidation of ferrous Fe in the obtained products, they were subjected to fast oxidation using H_2O_2, which allowed the conversion of the material to contain only ferric Fe species. By employing this strategy, it was possible to obtain LDH-type catalysts ranging from an iron content of 33.3 at-% to 83.3 at-% on the transition-metal position.

The successful synthesis of the obtained CO_3^{2-}-LDH products with the desired structure, morphology, and composition was proven by X-ray diffraction (XRD), Fourier-transformed infrared spectroscopy (FT-IR), scanning electron microscopy (SEM), and atomic absorption spectroscopy (AAS).

The XRD investigations allowed the observation of significant peak broadening when the Fe-content exceeds 75 at-%. This value is lower than in reference studies which can most likely be attributed to the strict adherence to the composition of divalent and trivalent cations of the highest stability.[116] Through variation of the Co/Fe ratio, a shift of the *003* reflections could be observed, accompanied by variations in rationality and peak width. In line with previous reports, these findings could be attributed to the fact that oxidation of the mixed-valent LDH triggered partial grafting of carbonate of the brucite layers.[91] Models have indicated a lower *d*-spacing for LDHs with fully grafted compared to ungrafted interlayer anions.[91] Therefore, the observed shifts were attributed to an interstratified real structure composed of random interstratifications of varying amounts of grafted and non-grafted layers, explaining both irrationality of the *00l*-series and variation in peak width. The simultaneously occurring planar defects in the stacking of adjacent layers are clearly influenced by the composition. Fe-poor samples featured intense and symmetrical reflections, while Fe-rich samples featured less intense, lambda-shaped reflections indicating turbostratic stacking, i.e., no defined phase relationship between the stacking layers.

To further prove the origin of these structural alterations by relating them to grafting, FT-IR spectroscopy measurements were employed to assess the binding mode of interlayer anions. For Fe-rich samples, the presence of grafted carbonate anions was evidenced through an energetic splitting of the ν_3 band, indicating a symmetry lowering from D_{3h} to C_{2v}. This splitting further proved that the previous PXRD observations indeed originated from carbonate grafting.

Despite the structural alterations, based on the choice of Co/Fe-ratio, it also had a notable impact on the OER electrocatalysis. It was found that a minimum of 20 at-% Co is necessary to achieve high current densities in the order of 200 mA cm^{-2} at potentials lower than 1.7 V vs. RHE. The highest electrocatalytic OER activities were determined for the CoFe layered (oxy)hydroxide material with a Fe-content of 50 at-% and 66 at-%. Thereby, synergistic effects could be exploited in LDHs composed of these two transition metals. However, it was underlined that the gradual replacement of Co with Fe also bears structural alterations based on a higher tendency of interlayer carbonate grafting to the brucite-like layers.

4.2 Influence of Grafting on the electrocatalytic capabilities of layered materials

The studies presented in chapters 3.4.1.3 and 4.1 showed that the grafting of interlayer ions might play a vital role in the structural constitution of an OER catalyst, its activity, and its stability. Despite the significant relevance of brucite-type materials for OER catalysis, the effect of grafting anions to these brucite-type layers was never systematically investigated.

This study aimed to provide a more profound insight into the effect of grafting concerning the activity of materials to be used as OER catalysts. For this purpose, Co- and Ni-based materials from the class of brucite-type layered compounds were investigated. These samples included the corresponding metal hydroxides $M(OH)_2$ without interlayer ions (Fig. 11a), LDHs with free interlayer ions (Fig. 11b), and hydroxynitrates with interlayer anions bound to the layers (Fig. 11c). All compounds were synthesized, structurally characterized by means of X-ray diffraction (XRD) and Fourier-transformed infrared spectroscopy (FT-IR), and studied in terms of their catalytic capabilities to facilitate the OER.

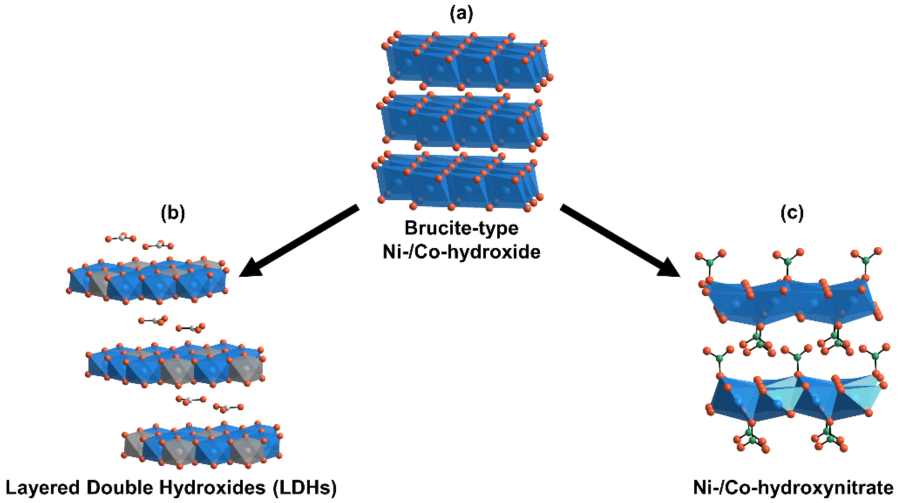

Figure 11: Chemical binding of interlayer ions, i.e., grafting to brucite-like layered materials, influences their electrocatalytic capabilities. Three Ni- and Co-compounds were assessed: (a) Brucite-type $M(OH)_2$ (no interlayer ions), (b) LDHs (free interlayer anions), and (c) hydroxynitrate (fully bonded interlayer ions). Formal substitution of OH^- with NO_3^- allowed for a widening of the interlayer space and a reduced electron density at the metal centers to induce the onset of the OER at lower potentials.[117] [Copyright 2021 Wiley-VCH Verlag GmbH & Co. KGaA. *Reproduced with permission.*]

The metal hydroxide representatives $Ni(OH)_2$ and $Co(OH)_2$ expectedly featured the lowest interlayer distances with 4.6 and 4.7 Å. The distance is the narrowest of all investigated materials due to the absence of an interlayer ion. The interlayer space of LDHs and hydroxynitrates was thus significantly higher due to the steric demand of the corresponding ions. For LDHs, considerably larger interlayer distances of 7.5 and 7.6 Å was found for NiAl-CO_3 and CoAl-CO_3, respectively. Compared to the other classes, hydroxynitrates featured a lower spacing between their layers due to the grafting of interlayer nitrate anions, which allowed for a contraction of the layers. Here, 6.9 and 7.0 Å were determined for the Ni- and Co-hydroxynitrate, respectively.

FT-IR investigations of the materials expectedly indicated the absence of any interlayer anion in the $M(OH)_2$ samples but exhibited additional bands for the interlayer anions in both LDH and hydroxynitrate samples. However, the bonding mode of the interlayer anions was inherently different. Direct bonding to the layer compared to free interlayer anions was evidenced by the symmetry of the interlayer anions. For LDHs, intercalated carbonate anions exhibited D_{3h} symmetry in both LDHs, while the symmetry in the hydroxynitrates was reduced to C_{2v} through grafting to the layer. This was concluded based on the presence of two distinct v_1 and v_4 modes at 1300 and 1500 cm^{-1}, respectively, with a characteristic wavenumber difference of 200 cm^{-1}. The presence of these nodes indicated that one oxygen of nitrate was directly bound to the metal cation completing its octahedral coordination shell and provided direct experimental evidence for the nitrate grafting in both Ni- and Co-hydroxynitrate.

Indeed, the bonding situation between the layers and the interlayer ions proved to influence the electronic structure and thus the observed OER activity. Notably, hydroxynitrates allowed the formation of the electrocatalytically active species at significantly lower potentials than the other compounds studied. Grafted nitrate anions influenced the oxidation of Ni^{2+}, allowing its conversion to the active OER species, i.e., Ni^{3+} at more cathodic potentials.[58a] This indicated the highest intrinsic activity among all Ni-containing materials tested but was unfortunately hampered due to the lower number of active sites. Similar findings for the Co-hydroxynitrate confirmed this trend. Here, the oxidation peak associated with the Co^{2+} oxidation was found to be ~0.15 V and ~0.20 V lower compared to the corresponding β-$Co(OH)_2$ and CoAl-CO_3 LDH. In the case of Co-hydroxynitrate, current densities of 10 and 100 mA cm^{-2} could already be achieved with overpotentials of only 0.34 and 0.40 V, respectively.

Additional galvanostatic testing confirmed the high stability of hydroxynitrates under continuous load and thereby underlined the potential of this compositional flexible material class as an electrocatalyst. These results led to the conclusion that there were two significant influences on the redox activity of the compounds studied. Firstly, the widening of the interlayer spacing for better accessibility of the catalytically active centers. More accessibility to such active sites resulted in increased net activity. Secondly, the electron-donor capability of the interlayer anion, by formally replacing the metal center's hydroxide ligand. This alteration in the bonding situation also significantly influenced the electronic structure and, thus, the redox activity of the compounds studied.

4.3 Grafting control – OER catalysis through a scalable Fe-corrosion process

The results summarized in chapter 4.2 evidenced that the electrocatalytic capabilities within one material class can be optimized by choosing the extent of grafting. This finding and the pursuit of designing a scalable, sustainable, and non-toxic electrocatalyst led back to the all-iron OER catalyst mössbauerite. For this material, a detailed study regarding the driving force and structural consequences of grafting was discussed previously.[91] Nevertheless, these synthetic routes never allowed obtaining different amounts of grafted interlayer ions for the same material.

For this purpose, the study aimed to remove or minimize the driving force of grafting, i.e., the exothermic reaction of the mixed-valent precursor with H_2O_2. The developed electrodeposition through a scalable corrosion process of commercial steel allowed to obtain the mixed-valent green rust ($Fe_4^{2+}Fe_2^{3+}(OH)_{12}CO_3 \cdot 3\ H_2O$) before the critical step of oxidation to the monovalent Fe^{3+} catalyst mössbauerite ($Fe_6^{3+}(O)_4(OH)_8CO_3 \cdot 3\ H_2O$). The corresponding catalyst was successfully yielded by performing the oxidation either chemically (with H_2O_2) or electrochemically. The obtained materials were subjected to structural, morphological, and electrocatalytic OER tests using X-ray diffraction (XRD), Fourier-transformed infrared spectroscopy (FT-IR), Mössbauer spectroscopy, scanning electron microscopy (SEM), cyclic voltammetry (CV), and chronopotentiometry testing (CP).

Notably, the product obtained by electrochemical oxidation featured less contraction of the interlayer space and a reduction of observable stacking disorder. This was evidenced by XRD measurements which related variations in the apparent basal spacing to a random interstratification of grafted and intercalated domains. The higher reflection intensity and *d*-value observed for the electrochemically oxidized sample indicated significantly fewer grafted domains. Consequently, more intercalated (i.e., ungrafted) domains contributed to random interstratification, resulting in an overall higher observed basal spacing of 7.3 Å. For chemical oxidation, the typically featureless XRD pattern[70, 91] with broad reflections and the absence of the *002* reflection was observed. Here, extensive grafting of interlayer anions led to a contraction of the interlayer space decreasing from 7.5 Å of the parent green rust to 7.1 Å. Thus, it could be concluded that electrochemical oxidation induced less interlayer CO_3^{2-} grafting due to a smaller driving force for grafting than chemical oxidation.

Apparent characteristics for reduced grafting in the electrochemically oxidized sample were also found by performing FT-IR investigations. Similar to the analysis described in chapter 4.2, bonding to the brucite-like layer is accompanied by a symmetry reduction of the carbonate ion from D_{3h} to C_{2v}, resulting in a pronounced v_3 band splitting upon grafting. Therefore, it was possible to distinguish between grafted and intercalated carbonate anions. Comparing the chemically and electrochemically oxidized sample, the band splitting and, thus, the presence of grafted carbonate was evident in either sample. However, the relative intensity of the respective bands presented qualitative evidence that the ratio of grafted to ungrafted species was higher for the chemically oxidized sample. This finding provided further evidence to support the previous XRD findings that the degree of grafting could be reduced by electrochemical oxidation.

SEM analysis of both samples indicated a typical morphology of platy crystals which are often intergrown with smaller platelets. These morphological changes to the surface of the bare steel plate also allowed for increasing its number of active sites by a factor of 2.4 to 2.7 for the chemically and electrochemically oxidized samples, respectively. This property was evidenced by the analysis of the electrochemically active surface area (ECSA).

Electrocatalytic testing concluded that a current density of 100 mA cm^{-2} could be reached at potentials of 1.82 V and 1.84 V for the chemically and electrochemically oxidized samples, respectively. Thus, both outperformed the bare steel plate (1.88 V) when being operated in a 1 M KOH solution. Long-term measurements also showed a slower performance degradation for the electrochemically oxidized sample compared to the bare steel plate. Interestingly, the chemically oxidized sample exhibited a faster degradation. This difference in catalysts was attributed to the harsh conditions during chemical oxidation which ultimately may give rise to the loss of electrical contact between the catalyst and the current collector. In contrast, the mild electrochemical oxidation allowed for the formation of percolation paths, effectively delaying the degradation. In general, the increase in overpotential was an indicator of degradation and the loss of active sites, which was confirmed by post-mortem analysis. The bare steel plate exhibited discoloration after the experiment, likely due to the formation of inactive corrosion products that block access to active centers. The morphology of the catalyst-coated samples was generally preserved while they exhibited rounded corners and secondary deposits on the surface, likely originating from reprecipitation.

Besides improving the electrocatalytic capabilities of the steel plate, the direct electrodeposition of the catalyst on a conductive substrate also enabled the first systematic study of the impact of grafting on the performance of mössbauerite in the OER.

5 Literature

[1] a) Z. W. Seh, J. Kibsgaard, C. F. Dickens, I. B. Chorkendorff, J. K. Norskov, T. F. Jaramillo, *Science* **2017**, *355*, eaad4998; b) S. Chu, A. Majumdar, *Nature* **2012**, *488*, 294-303.

[2] M. Coronese, F. Lamperti, K. Keller, F. Chiaromonte, A. Roventini, *Proceedings of the National Academy of Sciences of the United States of America* **2019**, *116*, 21450-21455.

[3] I. O. Festus, *Policy* **2018**, *2*, 5-10.

[4] World Economic Forum, *Fostering effective energy transition 2022 edition* **2022**, (last accessed March 2023).

[5] World Economic Forum, *Fostering effective energy transition 2021 edition* **2021**, (last accessed March 2023).

[6] Fraunhofer Institute for Solar Energy Systems ISE, *Net Electricity Generation in Germany in 2022: Significant Increase in Generation from Wind and PV* **2023**, https://www.ise.fraunhofer.de/en/press-media/press-releases/2023/net-electricity-generation-in-germany-in-2022-significant-increase-in-generation-from-wind-and-pv.html (last accessed February 2023).

[7] Council of the European Union, *Fit for 55 package: Council reaches general approaches relating to emissions reductions and their social impacts* **2022**, https://www.consilium.europa.eu/en/press/press-releases/2022/2006/2029/fit-for-2055-council-reaches-general-approaches-relating-to-emissions-reductions-and-removals-and-their-social-impacts/ (last accessed July 2022).

[8] S. de Bruyn, C. Jongsma, B. Kampman, B. Görlach, J.-E. Thie, *Energy-intensive industries: Challenges and opportunities in energy transition* **2020**.

[9] P. Kishore, J. Bogineni, J. Rajesh, S. Halder, N. Jayaram, R. B. Weli, S. A. Atrooshi, R. Schwarze, C. Charin, D. Ishak, *Assessment* **2020**.

[10] Fort Frances Power Corporation, *Energy Storage* **2022**, https://ffpc.ca/energy-services/sustainable-energy/energy-storage (last accessed July 2022).

[11] J. Fernández-González, M. Rumayor, A. Domínguez-Ramos, A. Irabien, *Industrial & Engineering Chemistry Research* **2022**, *61*, 6163-6172.

[12] A. Ajanovic, M. Sayer, R. Haas, *International Journal of Hydrogen Energy* **2022**, *47*, 24136-24154.

[13] S. van Renssen, *Nature Climate Change* **2020**, *10*, 799-801.

[14] Z. Y. Cai, X. M. Bu, P. Wang, J. C. Ho, J. H. Yang, X. Y. Wang, *Journal of Materials Chemistry A* **2019**, *7*, 5069-5089.

[15] National Energy Technology Laboratory, *Seventh Edition Fuel Cell Handbook*, United States, **2004**.

[16] P. Millet, in *Hydrogen Production*, **2015**, pp. 33-62.

[17] N. T. Suen, S. F. Hung, Q. Quan, N. Zhang, Y. J. Xu, H. M. Chen, *Chemical Society Reviews* **2017**, *46*, 337-365.

[18] P. Atkins, J. de Paula, *Atkins' Physical Chemistry*, OUP Oxford, **2010**.

[19] a) Q. Lu, G. S. Hutchings, W. Yu, Y. Zhou, R. V. Forest, R. Tao, J. Rosen, B. T. Yonemoto, Z. Cao, H. Zheng, J. Q. Xiao, F. Jiao, J. G. Chen, *Nature Communications* **2015**, *6*, 6567; b) E. J. Popczun, J. R. McKone, C. G. Read, A. J. Biacchi, A. M. Wiltrout, N. S. Lewis, R. E. Schaak, *Journal of the American Chemical Society* **2013**, *135*, 9267-9270.

[20] J. Q. Chi, J. Y. Xie, W. W. Zhang, B. Dong, J. F. Qin, X. Y. Zhang, J. H. Lin, Y. M. Chai, C. G. Liu, *ACS applied materials & interfaces* **2019**, *11*, 4047-4056.

[21] a) E. J. Popczun, C. G. Read, C. W. Roske, N. S. Lewis, R. E. Schaak, *Angewandte Chemie International Edition* **2014**, *53*, 5427-5430; b) Y. Liu, X. Liang, L. Gu, Y. Zhang, G. D. Li, X. Zou, J. S. Chen, *Nature Communications* **2018**, *9*, 2609.

[22] a) G. Bronoel, J. Reby, *Electrochimica Acta* **1980**, *25*, 973-976; b) N. N. Yuan, Q. Q. Jiang, J. Li, J. G. Tang, *Arabian Journal of Chemistry* **2020**, *13*, 4294-4309.

[23] a) B. B. Zhao, C. C. Li, C. L. Xu, *Catalysis Science & Technology* **2012**, *2*, 1985-1994; b) M. D. Bhatt, J. Y. Lee, *Nanotechnology* **2021**, *32*, 335401; c) J. O. M. Bockris, J. McBreen, L. Nanis, *Journal of The Electrochemical Society* **1965**, *112*, 1025.

[24] a) F. Song, L. C. Bai, A. Moysiadou, S. Lee, C. Hu, L. Liardet, X. L. Hu, *Journal of the American Chemical Society* **2018**, *140*, 7748-7759; b) S. Marini, P. Salvi, P. Nelli, R. Pesenti, M. Villa, M. Berrettoni, G. Zangari, Y. Kiros, *Electrochimica Acta* **2012**, *82*, 384-391; c) G. Mattioli, P. Giannozzi, A. Amore Bonapasta, L. Guidoni, *Journal of the American Chemical Society* **2013**, *135*, 15353-15363.

[25] a) K. Bhattacharyya, A. A. Auer, *Journal of Physical Chemistry C* **2022**, *126*, 18623-18635; b) T. Reier, H. N. Nong, D. Teschner, R. Schlogl, P. Strasser, *Advanced Energy Materials* **2017**, *7*, 1601275.

[26] H. Dau, C. Limberg, T. Reier, M. Risch, S. Roggan, P. Strasser, *ChemCatChem* **2010**, *2*, 724-761.

[27] N. Eliaz, E. Gileadi, *Physical electrochemistry*, Wiley-VCH, Weinheim, Germany, **2019**.

[28] C. Du, Q. Tan, G. Yin, J. Zhang, in *Rotating Electrode Methods and Oxygen Reduction Electrocatalysts* (Eds.: W. Xing, G. Yin, J. Zhang), Elsevier, Amsterdam, **2014**, pp. 171-198.

[29] a) Y. Yan, *Frontiers in Chemistry* **2021**, *9*, 754357; b) H. Antony, A. Labrit, J. C. Rouchaud, L. Legrand, A. Chausse, *Electrochimica Acta* **2008**, *53*, 7173-7181; c) M. Lu, X. Cui, B. Song, H. Ouyang, K. Wang, Y. Wang, *ChemElectroChem* **2020**, *7*, 1080-1083.

[30] a) H. X. Zhang, J. F. Zheng, Y. G. Chao, K. M. Zhang, Z. P. Zhu, *New Journal of Chemistry* **2018**, *42*, 7254-7261; b) M. Ishizaki, H. Fujii, K. Toshima, H. Tanno, H. Sutoh, M. Kurihara, *Inorganica Chimica Acta* **2020**, *502*, 119345.

[31] a) Q. X. Mou, Z. H. Xu, G. N. Wang, E. L. Li, J. Y. Liu, P. P. Zhao, X. H. Liu, H. B. Li, G. Z. Cheng, *Inorganic Chemistry Frontiers* **2021**, *8*, 2889-2899; b) P. Guo, Y. X. Wu, W. M. Lau, H. Liu, L. M. Liu, *Journal of Alloys and Compounds* **2017**, *723*, 772-778.

[32] a) M. R. Zhang, T. T. Wang, H. Y. Cao, S. S. Cui, P. W. Du, *Journal of Energy Chemistry* **2020**, *42*, 71-76; b) X. Yang, C. J. Wang, C. C. Hou, W. F. Fu, Y. Chen, *ACS Sustainable Chemistry & Engineering* **2018**, *6*, 2893-2897.

[33] a) D. Wang, J. Li, Y. Zhao, H. Xu, J. Zhao, *Electrochimica Acta* **2019**, *316*, 8-18; b) M. Xing-Xing, C. Li, Z. Zhang, T. Ji-Lin, *Chinese Journal of Analytical Chemistry* **2020**, *48*, e20001-e20012.

[34] a) S. M. Al-Zuraiji, T. Benko, K. Frey, Z. Kerner, J. S. Pap, *Catalysts* **2021**, *11*, 577; b) D. Lebedev, R. Ezhov, J. Heras-Domingo, A. Comas-Vives, N. Kaeffer, M. Willinger, X. Solans-Monfort, X. Huang, Y. Pushkar, C. Coperet, *ACS Central Science* **2020**, *6*, 1189-1198.

[35] a) J. W. D. Ng, M. Garcia-Melchor, M. Bajdich, P. Chakthranont, C. Kirk, A. Vojvodic, T. F. Jaramillo, *Nature Energy* **2016**, *1*, 1-8; b) E. Petkucheva, G. Borisov, E. Lefterova, J. Heiss, U. Schnakenberg, E. Slavcheva, *International Journal of Hydrogen Energy* **2018**, *43*, 16905-16912.

[36] M. P. Browne, A. Mills, *Journal of Materials Chemistry A* **2018**, *6*, 14162-14169.

[37] a) X. Hu, X. Tian, Y. W. Lin, Z. Wang, *RSC Advances* **2019**, *9*, 31563-31571; b) J. D. Benck, B. A. Pinaud, Y. Gorlin, T. F. Jaramillo, *PLoS One* **2014**, *9*, e107942.

[38] J. Song, C. Wei, Z. F. Huang, C. Liu, L. Zeng, X. Wang, Z. J. Xu, *Chemical Society Reviews* **2020**, *49*, 2196-2214.

[39] C. C. McCrory, S. Jung, J. C. Peters, T. F. Jaramillo, *Journal of the American Chemical Society* **2013**, *135*, 16977-16987.

[40] Á. García, J. Torrero, M. Retuerto, S. Rojas, in *Nanomaterials for Electrocatalysis* (Eds.: T. Maiyalagan, M. Khandelwal, A. Kumar, T. A. Nguyen, G. Yasin), Elsevier, **2022**, pp. 169-211.

[41] R. Li, C. Li, in *Advances in Catalysis, Vol. 60* (Ed.: C. Song), Academic Press, **2017**, pp. 1-57.

[42] C. G. Kuai, Z. R. Xu, C. Xi, A. Y. Hu, Z. J. Yang, Y. Zhang, C. J. Sun, L. X. Li, D. Sokaras, C. K. Dong, S. Z. Qiao, X. W. Du, F. Lin, *Nature Catalysis* **2020**, *3*, 743-753.

[43] a) T. Binninger, R. Mohamed, K. Waltar, E. Fabbri, P. Levecque, R. Kotz, T. J. Schmidt, *Scientific reports* **2015**, *5*, 1-7; b) F. Reikowski, F. Maroun, I. Pacheco, T. Wiegmann, P. Allongue, J. Stettner, O. M. Magnussen, *Acs Catalysis* **2019**, *9*, 3811-3821.

[44] S. Klaus, Y. Cai, M. W. Louie, L. Trotochaud, A. T. Bell, *Journal of Physical Chemistry C* **2015**, *119*, 7243-7254.

[45] S. Cherevko, *Current opinion in electrochemistry* **2018**, *8*, 118-125.

[46] R. Wang, C. Z. Wang, S. H. Yin, Y. Peng, J. J. Chen, Y. X. Deng, J. H. Li, *Catalysis Today* **2021**, *364*, 140-147.

[47] a) A. Grimaud, A. Demortière, M. Saubanère, W. Dachraoui, M. Duchamp, M.-L. Doublet, J.-M. Tarascon, *Nature Energy* **2016**, *2*, 16189; b) A. Sivanantham, P. Ganesan, A. Vinu, S. Shanmugam, *Acs Catalysis* **2019**, *10*, 463-493.

[48] S. E. Michaud, M. T. Riehs, W. J. Feng, C. C. Lin, C. C. L. McCrory, *Chemical Communications* **2021**, *57*, 883-886.

[49] a) A. Keçebaş, M. Kayfeci, M. Bayat, in *Solar Hydrogen Production* (Eds.: F. Calise, M. D. D’Accadia, M. Santarelli, A. Lanzini, D. Ferrero), Academic Press, **2019**, pp. 299-317; b) M. Schalenbach, O. Kasian, K. J. J. Mayrhofer, *International Journal of Hydrogen Energy* **2018**, *43*, 11932-11938.

[50] a) J. Garche, C. K. Dyer, P. T. Moseley, Z. Ogumi, D. A. J. Rand, B. Scrosati, *Encyclopedia of Electrochemical Power Sources*, Elsevier Science, **2013**; b) D. A. J. Rand, R. M. Dell, R. Dell, J. Hunt, R. S. o. Chemistry, *Hydrogen Energy: Challenges and Prospects*, Royal Society of Chemistry, **2008**; c) K. Zeng, D. K. Zhang, *Progress in Energy and Combustion Science* **2010**, *36*, 307-326.

[51] a) Y. Xiong, P. He, *Journal of Materials Science* **2023**, *58*, 2041-2067; b) J. Li, *Nano-Micro Letters* **2022**, *14*, 112; c) A. Vazhayil, L. Vazhayal, J. Thomas, C. S. Ashok, N.

Thomas, *Applied Surface Science Advances* **2021**, *6*, 100184; d) F. Zeng, C. Mebrahtu, L. F. Liao, R. Palkovits, A. K. Beine, *Journal of Energy Chemistry* **2022**, *69*, 301-329.

[52] K. Zhang, R. Zou, *Small* **2021**, *17*, e2100129.

[53] a) R. P. Forslund, W. G. Hardin, X. Rong, A. M. Abakumov, D. Filimonov, C. T. Alexander, J. T. Mefford, H. Iyer, A. M. Kolpak, K. P. Johnston, K. J. Stevenson, *Nature Communications* **2018**, *9*, 3150; b) Y. L. Zhu, Q. Lin, Z. W. Hu, Y. B. Chen, Y. C. Yin, H. A. Tahini, H. J. Lin, C. T. Chen, X. W. Zhang, Z. P. Shao, H. T. Wang, *Small* **2020**, *16*, 2001204.

[54] Y. Zhang, X. X. Wang, F. Q. Luo, Y. Tan, L. X. Zeng, B. Z. Fang, A. H. Liu, *Applied Catalysis B: Environmental* **2019**, *256*, 117852.

[55] Y. Lee, J. Suntivich, K. J. May, E. E. Perry, Y. Shao-Horn, *The journal of physical chemistry letters* **2012**, *3*, 399-404.

[56] a) X. D. Cui, B. L. Zhang, C. Y. Zeng, S. M. Guo, *MRS Communications* **2018**, *8*, 1230-1235; b) W. J. Dai, T. Lu, Y. Pan, *Journal of Power Sources* **2019**, *430*, 104-111.

[57] a) Y. L. Zhu, W. Zhou, J. Yu, Y. B. Chen, M. L. Liu, Z. P. Shao, *Chemistry of Materials* **2016**, *28*, 1691-1697; b) S. Yagi, I. Yamada, H. Tsukasaki, A. Seno, M. Murakami, H. Fujii, H. Chen, N. Umezawa, H. Abe, N. Nishiyama, S. Mori, *Nature Communications* **2015**, *6*, 8249.

[58] a) H. Y. Wang, Y. Y. Hsu, R. Chen, T. S. Chan, H. M. Chen, B. Liu, *Advanced Energy Materials* **2015**, *5*, 1500091; b) H. Chen, X. X. Huang, L. J. Zhou, G. D. Li, M. H. Fan, X. X. Zou, *ChemCatChem* **2016**, *8*, 992-1000.

[59] a) Y. C. Wang, T. Zhou, K. Jiang, P. M. Da, Z. Peng, J. Tang, B. A. Kong, W. B. Cai, Z. Q. Yang, G. F. Zheng, *Advanced Energy Materials* **2014**, *4*, 1400696; b) G. Gardner, J. Al-Sharab, N. Danilovic, Y. B. Go, K. Ayers, M. Greenblatt, G. C. Dismukes, *Energy & Environmental Science* **2016**, *9*, 184-192.

[60] a) C. Zhang, M. Shao, L. Zhou, Z. Li, K. Xiao, M. Wei, *ACS applied materials & interfaces* **2016**, *8*, 33697-33703; b) Y. Wang, M. Qiao, Y. Li, S. Wang, *Small* **2018**, *14*, e1800136.

[61] a) M. S. Burke, L. J. Enman, A. S. Batchellor, S. H. Zou, S. W. Boettcher, *Chemistry of Materials* **2015**, *27*, 7549-7558; b) H. Yin, Z. Tang, *Chemical Society Reviews* **2016**, *45*, 4873-4891; c) C. Tang, H. F. Wang, H. S. Wang, F. Wei, Q. Zhang, *Journal of Materials Chemistry A* **2016**, *4*, 3210-3216.

[62] a) Y. Gorlin, B. Lassalle-Kaiser, J. D. Benck, S. Gul, S. M. Webb, V. K. Yachandra, J. Yano, T. F. Jaramillo, *Journal of the American Chemical Society* **2013**, *135*, 8525-8534;

b) A. Indra, P. W. Menezes, I. Zaharieva, E. Baktash, J. Pfrommer, M. Schwarze, H. Dau, M. Driess, *Angewandte Chemie International Edition* **2013**, *52*, 13206-13210; c) R. D. Smith, M. S. Prevot, R. D. Fagan, Z. Zhang, P. A. Sedach, M. K. Siu, S. Trudel, C. P. Berlinguette, *Science* **2013**, *340*, 60-63; d) R. K. Hocking, R. Brimblecombe, L. Y. Chang, A. Singh, M. H. Cheah, C. Glover, W. H. Casey, L. Spiccia, *Nature Chemistry* **2011**, *3*, 461-466; e) R. Subbaraman, D. Tripkovic, K. C. Chang, D. Strmcnik, A. P. Paulikas, P. Hirunsit, M. Chan, J. Greeley, V. Stamenkovic, N. M. Markovic, *Nature Materials* **2012**, *11*, 550-557; f) D. Zhou, P. Li, X. Lin, A. McKinley, Y. Kuang, W. Liu, W. F. Lin, X. Sun, X. Duan, *Chemical Society Reviews* **2021**, *50*, 8790-8817.

[63] a) B. M. Hunter, W. Hieringer, J. R. Winkler, H. B. Gray, A. M. Müller, *Energy & Environmental Science* **2016**, *9*, 1734-1743; b) A. I. Khan, D. O'Hare, *Journal of Materials Chemistry* **2002**, *12*, 3191-3198; c) L. Lv, Z. X. Yang, K. Chen, C. D. Wang, Y. J. Xiong, *Advanced Energy Materials* **2019**, *9*, 1803358; d) X. Lu, H. Xue, H. Gong, M. Bai, D. Tang, R. Ma, T. Sasaki, *Nano-Micro Letters* **2020**, *12*, 86.

[64] R. Ma, J. Liang, K. Takada, T. Sasaki, *Journal of the American Chemical Society* **2011**, *133*, 613-620.

[65] J. Liang, R. Ma, N. Iyi, Y. Ebina, K. Takada, T. Sasaki, *Chemistry of Materials* **2009**, *22*, 371-378.

[66] S. M. Auerbach, K. A. Carrado, P. K. Dutta, *Handbook of Layered Materials*, CRC Press, **2004**.

[67] F. Dionigi, Z. Zeng, I. Sinev, T. Merzdorf, S. Deshpande, M. B. Lopez, S. Kunze, I. Zegkinoglou, H. Sarodnik, D. Fan, A. Bergmann, J. Drnec, J. F. Araujo, M. Gliech, D. Teschner, J. Zhu, W. X. Li, J. Greeley, B. R. Cuenya, P. Strasser, *Nature Communications* **2020**, *11*, 2522.

[68] J. He, M. Wei, B. Li, Y. Kang, D. G. Evans, X. Duan, in *Layered Double Hydroxides* (Eds.: X. Duan, D. G. Evans), Springer Berlin Heidelberg, Berlin, Heidelberg, **2005**, pp. 89-119.

[69] D. L. Bish, *Bulletin de Mineralogie* **1980**, *103*, 170-175.

[70] M. Ertl, C. Andronescu, J. Moir, M. Zobel, F. E. Wagner, S. Barwe, G. Ozin, W. Schuhmann, J. Breu, *Chemistry* **2018**, *24*, 9004-9008.

[71] D. E. Hall, *Journal of The Electrochemical Society* **1983**, *130*, 317-321.

[72] M. E. G. Lyons, M. P. Brandon, *International Journal of Electrochemical Science* **2008**, *3*, 1386-1424.

[73] a) X. Long, S. Xiao, Z. Wang, X. Zheng, S. Yang, *Chemical Communications* **2015**, *51*, 1120-1123; b) F.-S. Zhang, J.-W. Wang, J. Luo, R.-R. Liu, Z.-M. Zhang, C.-T. He, T.-B. Lu, *Chemical science* **2018**, *9*, 1375-1384.

[74] a) A. Dutta, N. Pradhan, *Journal of Physical Chemistry Letters* **2017**, *8*, 144-152; b) G. F. Chen, T. Y. Ma, Z. Q. Liu, N. Li, Y. Z. Su, K. Davey, S. Z. Qiao, *Advanced Functional Materials* **2016**, *26*, 3314-3323.

[75] a) M. F. Shao, F. Y. Ning, Y. F. Zhao, J. W. Zhao, M. Wei, D. G. Evans, X. Duan, *Chemistry of Materials* **2012**, *24*, 1192-1197; b) Y. F. Zhao, X. D. Jia, G. I. N. Waterhouse, L. Z. Wu, C. H. Tung, D. O'Hare, T. R. Zhang, *Advanced Energy Materials* **2016**, *6*, 1501974; c) Q. Wang, D. O'Hare, *Chemical Reviews* **2012**, *112*, 4124-4155.

[76] a) R. Sasai, H. Sato, M. Sugata, T. Fujimura, S. Ishihara, K. Deguchi, S. Ohki, M. Tansho, T. Shimizu, N. Oita, *Inorganic chemistry* **2019**, *58*, 10928-10935; b) X. Wang, J. Lu, W. Shi, F. Li, M. Wei, D. G. Evans, X. Duan, *Langmuir* **2010**, *26*, 1247-1253; c) M. Luo, Z. Cai, C. Wang, Y. M. Bi, L. Qian, Y. C. Hao, L. Li, Y. Kuang, Y. P. Li, X. D. Lei, Z. Y. Huo, W. Liu, H. L. Wang, X. M. Sun, X. Duan, *Nano Research* **2017**, *10*, 1732-1739.

[77] D. J. Zhou, Y. Jia, X. X. Duan, J. L. Tang, J. Xu, D. Liu, X. Y. Xiong, J. M. Zhang, J. Luo, L. R. Zheng, B. Liu, Y. Kuang, X. M. Sun, X. Duan, *Nano Energy* **2019**, *60*, 661-666.

[78] a) F. Song, X. Hu, *Nature Communications* **2014**, *5*, 4477; b) F. Song, X. Hu, *Journal of the American Chemical Society* **2014**, *136*, 16481-16484; c) K. Fan, H. Chen, Y. Ji, H. Huang, P. M. Claesson, Q. Daniel, B. Philippe, H. Rensmo, F. Li, Y. Luo, L. Sun, *Nature Communications* **2016**, *7*, 11981; d) Y. S. Xie, Z. Wang, M. Ju, X. Long, S. Yang, *Chemical science* **2019**, *10*, 8354-8359; e) X. T. Han, C. Yu, J. Yang, C. T. Zhao, H. W. Huang, Z. B. Liu, P. M. Ajayan, J. S. Qiu, *Advanced Materials Interfaces* **2016**, *3*, 1500782.

[79] N. Li, D. K. Bediako, R. G. Hadt, D. Hayes, T. J. Kempa, F. von Cube, D. C. Bell, L. X. Chen, D. G. Nocera, *Proceedings of the National Academy of Sciences of the United States of America* **2017**, *114*, 1486-1491.

[80] D. Friebel, M. W. Louie, M. Bajdich, K. E. Sanwald, Y. Cai, A. M. Wise, M. J. Cheng, D. Sokaras, T. C. Weng, R. Alonso-Mori, R. C. Davis, J. R. Bargar, J. K. Norskov, A. Nilsson, A. T. Bell, *Journal of the American Chemical Society* **2015**, *137*, 1305-1313.

[81] J. Y. Chen, L. Dang, H. Liang, W. Bi, J. B. Gerken, S. Jin, E. E. Alp, S. S. Stahl, *Journal of the American Chemical Society* **2015**, *137*, 15090-15093.

[82] H. Liang, F. Meng, M. Caban-Acevedo, L. Li, A. Forticaux, L. Xiu, Z. Wang, S. Jin, *Nano Letters* **2015**, *15*, 1421-1427.

[83] M. B. Stevens, C. D. M. Trang, L. J. Enman, J. Deng, S. W. Boettcher, *Journal of the American Chemical Society* **2017**, *139*, 11361-11364.

[84] R. Liu, Y. Wang, D. Liu, Y. Zou, S. Wang, *Advanced Materials* **2017**, *29*, 1701546.

[85] a) Z. Lu, L. Qian, Y. Tian, Y. Li, X. Sun, X. Duan, *Chemical Communications* **2016**, *52*, 908-911; b) L. Qian, Z. Y. Lu, T. H. Xu, X. C. Wu, Y. Tian, Y. P. Li, Z. Y. Huo, X. M. Sun, X. Duan, *Advanced Energy Materials* **2015**, *5*, 1500245.

[86] W. Ma, R. Ma, C. Wang, J. Liang, X. Liu, K. Zhou, T. Sasaki, *ACS Nano* **2015**, *9*, 1977-1984.

[87] a) D. J. Zhou, Z. Cai, Y. M. Bi, W. L. Tian, M. Luo, Q. Zhang, Q. Zhang, Q. X. Xie, J. D. Wang, Y. P. Li, Y. Kuang, X. Duan, M. Bajdich, S. Siahrostami, X. M. Sun, *Nano Research* **2018**, *11*, 1358-1368; b) Y. Q. Xu, Y. C. Hao, G. X. Zhang, Z. Y. Lu, S. Han, Y. P. Li, X. M. Sun, *RSC Advances* **2015**, *5*, 55131-55135.

[88] M. Yu, E. Budiyanto, H. Tuysuz, *Angewandte Chemie International Edition* **2022**, *61*, e202103824.

[89] a) I. Ahmad, J. Ahmed, S. Batool, M. N. Zafar, A. Hanif, Zahidullah, M. F. Nazar, A. Ul-Hamid, U. Jabeen, A. Dahshan, M. Idrees, S. A. Shehzadi, *Journal of Alloys and Compounds* **2022**, *894*, 162409; b) X. X. Zou, Y. Y. Wu, Y. P. Liu, D. P. Liu, W. Li, L. Gu, H. Liu, P. W. Wang, L. Sun, Y. Zhang, *Chem* **2018**, *4*, 1139-1152; c) J. C. Li, S. Maurya, Y. S. Kim, T. Li, L. G. Wang, Q. R. Shi, D. Liu, S. Feng, Y. H. Lin, M. H. Shao, *Acs Catalysis* **2020**, *10*, 2452-2458.

[90] a) S. H. Zou, M. S. Burke, M. G. Kast, J. Fan, N. Danilovic, S. W. Boettcher, *Chemistry of Materials* **2015**, *27*, 8011-8020; b) J. R. Swierk, S. Klaus, L. Trotochaud, A. T. Bell, T. D. Tilley, *Journal of Physical Chemistry C* **2015**, *119*, 19022-19029; c) W. Luo, C. Jiang, Y. Li, S. A. Shevlin, X. Han, K. Qiu, Y. Cheng, Z. Guo, W. Huang, J. Tang, *Journal of Materials Chemistry A* **2017**, *5*, 2021-2028; d) A. Samanta, S. Das, S. Jana, *ACS Sustainable Chemistry & Engineering* **2019**, *7*, 12117-12124; e) M. Müllner, M. Riva, F. Kraushofer, M. Schmid, G. S. Parkinson, S. F. L. Mertens, U. Diebold, *The Journal of Physical Chemistry C* **2018**, *123*, 8304-8311.

[91] P. B. Lyu, M. Ertl, C. J. Heard, L. Grajciar, A. V. Radha, T. Martin, J. Breu, P. Nachtigall, *Journal of Physical Chemistry C* **2019**, *123*, 25157-25165.

[92] C. Vaysse, L. Guerlou-Demourgues, C. Delmas, *Inorganic chemistry* **2002**, *41*, 6905-6913.

[93] A. Shimamura, E. Kanezaki, M. I. Jones, J. B. Metson, *Journal of Solid State Chemistry* **2012**, *186*, 116-123.

[94] K. Muranishi, A. Shimamura, M. Kurashina, E. Kanezaki, in *International Journal of Modern Physics: Conference Series, Vol. 6*, World Scientific, **2012**, pp. 127-132.

[95] L. Bigey, F. Malherbe, A. De Roy, J. P. Besse, *Molecular Crystals and Liquid Crystals Science and Technology Section a-Molecular Crystals and Liquid Crystals* **1998**, *311*, 221-226.

[96] a) H. Nabipour, Y. Hu, *Journal of Porous Materials* **2022**, *29*, 341-356; b) E. Kandare, J. M. Hossenlopp, *The Journal of Physical Chemistry B* **2005**, *109*, 8469-8475; c) M. Rajamathi, P. Vishnu Kamath, *Journal of Power Sources* **1998**, *70*, 118-121.

[97] M. Meyn, K. Beneke, G. Lagaly, *Inorganic chemistry* **2002**, *32*, 1209-1215.

[98] M. Taibi, S. Ammar, N. Jouini, F. Fievet, P. Molinie, M. Drillon, *Journal of Materials Chemistry* **2002**, *12*, 3238-3244.

[99] J.-H. Choy, Y.-M. Kwon, K.-S. Han, S.-W. Song, S. H. Chang, *Materials Letters* **1998**, *34*, 356-363.

[100] S. P. Newman, W. Jones, *Journal of Solid State Chemistry* **1999**, *148*, 26-40.

[101] B. Bovio, S. Locchi, *Journal of Crystallographic and Spectroscopic Research* **1982**, *12*, 507-517.

[102] a) G.-G. Linder, M. Atanasov, J. Pebler, *Journal of Solid State Chemistry* **1995**, *116*, 1-7; b) V. Laget, C. Hornick, P. Rabu, M. Drillon, R. Ziessel, *Coordination chemistry reviews* **1998**, *178*, 1533-1553; c) W. Fujita, K. Awaga, *Inorganic chemistry* **1996**, *35*, 1915-1917; d) K. Petrov, N. Zotov, E. Mirtcheva, O. Garciamartinez, R. M. Rojas, *Journal of Materials Chemistry* **1994**, *4*, 611-614; e) A. López-Delgado, S. López-Andrés, O. Garcia-Martinez, P. Millán, R. M. Rojas, *Journal of Materials Science* **1987**, *22*, 2169-2174.

[103] a) L. Markov, K. Petrov, V. Petkov, *Thermochimica acta* **1986**, *106*, 283-292; b) J. T. Rajamathi, A. Arulraj, N. Ravishankar, J. Arulraj, M. Rajamathi, *Langmuir* **2008**, *24*, 11164-11168.

[104] S. H. Park, Y. D. Huh, *Bulletin of the Korean Chemical Society* **2013**, *34*, 768-772.

[105] A. C. Cardiel, K. J. McDonald, K. S. Choi, *Langmuir* **2017**, *33*, 9262-9270.

[106] N. Thomas, *Materials Research Bulletin* **2012**, *47*, 3568-3572.

[107] E. Kandare, J. M. Hossenlopp, *Inorganic chemistry* **2006**, *45*, 3766-3773.

[108] U. Costantino, F. Marmottini, M. Nocchetti, R. Vivani, *European Journal of Inorganic Chemistry* **1998**, *1998*, 1439-1446.

[109] S. Zhang, B. Ni, H. Li, H. Lin, H. Zhu, H. Wang, X. Wang, *Chemical Communications* **2017**, *53*, 8010-8013.

[110] M. Xie, L. Yang, Y. Ji, Z. Wang, X. Ren, Z. Liu, A. M. Asiri, X. Xiong, X. Sun, *Nanoscale* **2017**, *9*, 16612-16615.

[111] S. Dutta, C. Ray, Y. Negishi, T. Pal, *ACS applied materials & interfaces* **2017**, *9*, 8134-8141.

[112] T. Tang, W. J. Jiang, S. Niu, N. Liu, H. Luo, Y. Y. Chen, S. F. Jin, F. Gao, L. J. Wan, J. S. Hu, *Journal of the American Chemical Society* **2017**, *139*, 8320-8328.

[113] Y. Ma, J. Chu, Z. Li, D. Rakov, X. Han, Y. Du, B. Song, P. Xu, *Small* **2018**, *14*, e1803783.

[114] a) A. Karmakar, S. K. Srivastava, *ACS Applied Energy Materials* **2020**, *3*, 7335-7344; b) S. Zhang, B. Huang, L. Wang, X. Zhang, H. Zhu, X. Zhu, J. Li, S. Guo, E. Wang, *ACS applied materials & interfaces* **2020**, *12*, 40220-40228.

[115] K. Karthick, S. Subhashini, R. Kumar, S. Sethuram Markandaraj, M. M. Teepikha, S. Kundu, *Inorganic chemistry* **2020**, *59*, 16690-16702.

[116] S. J. Kim, Y. Lee, D. K. Lee, J. W. Lee, J. K. Kang, *Journal of Materials Chemistry A* **2014**, *2*, 4136-4139.

[117] A. V. Radha, S. Weiss, I. Sanjuan, M. Ertl, C. Andronescu, J. Breu, *Chemistry* **2021**, *27*, 16930-16937.

6 Publications

This chapter lists all publications and the individual contributions:

S. Weiß, M. Ertl, S.D. Varhade, A.V. Radha, W. Schuhmann, J. Breu, C. Andronescu: Trivalent iron rich CoFe layered oxyhydroxides for electrochemical water oxidation, *Electrochimica Acta*, **2020**, 136256.

Prof. C. Andronescu, Dr. M. Ertl, and I developed the publication concept. *Dr. M. Ertl* and I conducted the synthesis and chemical characterization. *Dr. A.V. Radha* assisted in the interpretation of the data. Electrochemical measurements were performed by *S.D. Varhade* and evaluated by me. The manuscript was written by *Prof. C. Andronescu*, *Prof. J. Breu*, *Prof. W. Schuhmann,* and me.

A.V. Radha, S. Weiß, I. Sanjuán, M. Ertl, C. Andronescu, J. Breu: The Effect of Interlayer Anion Grafting on Water Oxidation Electrocatalysis: A Comparative Study of Ni- and Co-Based Brucite-Type Layered Hydroxides, Layered Double Hydroxides and Hydroxynitrate Salts, *Chemistry - A European Journal*, **2021**, 16930-16937.

Prof. J. Breu, Dr. A.V. Radha, and I developed the publication concept. The chemical synthesis was carried out by *Dr. A.V. Radha* and *Dr. M. Ertl*. I performed the structural characterization and interpretation of the data. Electrochemical measurements were performed and evaluated by *Dr. I. Sanjuán* and *Prof. C. Andronescu*. The manuscript was written by *Prof. J. Breu*, *Prof. C. Andronescu*, and me.

S. Weiß, A.V. Radha, M. Ertl, C. McCammon, J. Breu: Sustainable oxygen evolution catalysis – electrochemical generation of mössbauerite via corrosion engineering of steel, *Materials Advances*, **2021**, 5650-5656.

I developed the concept of the publication and conducted the synthesis, chemical characterization, and electrochemical measurements/evaluation. *Dr. A.V. Radha* and *Dr. M.* Ertl assisted in discussing the data. *Dr. C. McCammon* performed and evaluated the Mössbauer spectroscopy measurements. *Prof. J. Breu* and I wrote the manuscript.

6.1 Structural and electrochemical effects of Fe incorporation in LDHs

Trivalent iron rich CoFe layered oxyhydroxides for electrochemical water oxidation

Sebastian Weiß[a], Michael Ertl[a], Swapnil Digambar Varhade[b], A.V. Radha[a], Wolfgang Schuhmann[b], Josef Breu[a,*], Corina Andronescu[c,*]

Published in Electrochimica Acta **2020**, 350, 136256.

Impact Factor (2023) Electrochimica Acta: 6.901
DOI: 10.1016/j.electacta.2020.136256

[a] Bavarian Polymer Institute and Department of Chemistry, University of Bayreuth, Universitäatsstr. 30, 95440, Bayreuth, Germany

[b] Analytical Chemistry & Center for Electrochemical Sciences (CES), Faculty of Chemistry and Biochemistry, Ruhr University Bochum, Universitätsstr. 150, D-44780, Bochum, Germany

[c] Chemical Technology III and CENIDE Center for Nanointegration, University Duisburg-Essen, Carl-Benz-Str. 199, D-47057, Duisburg, Germany

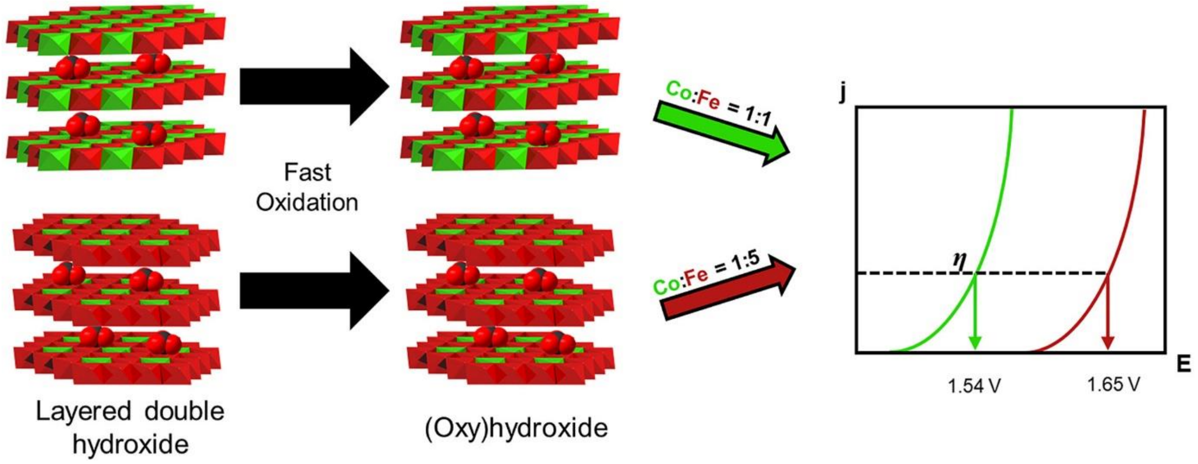

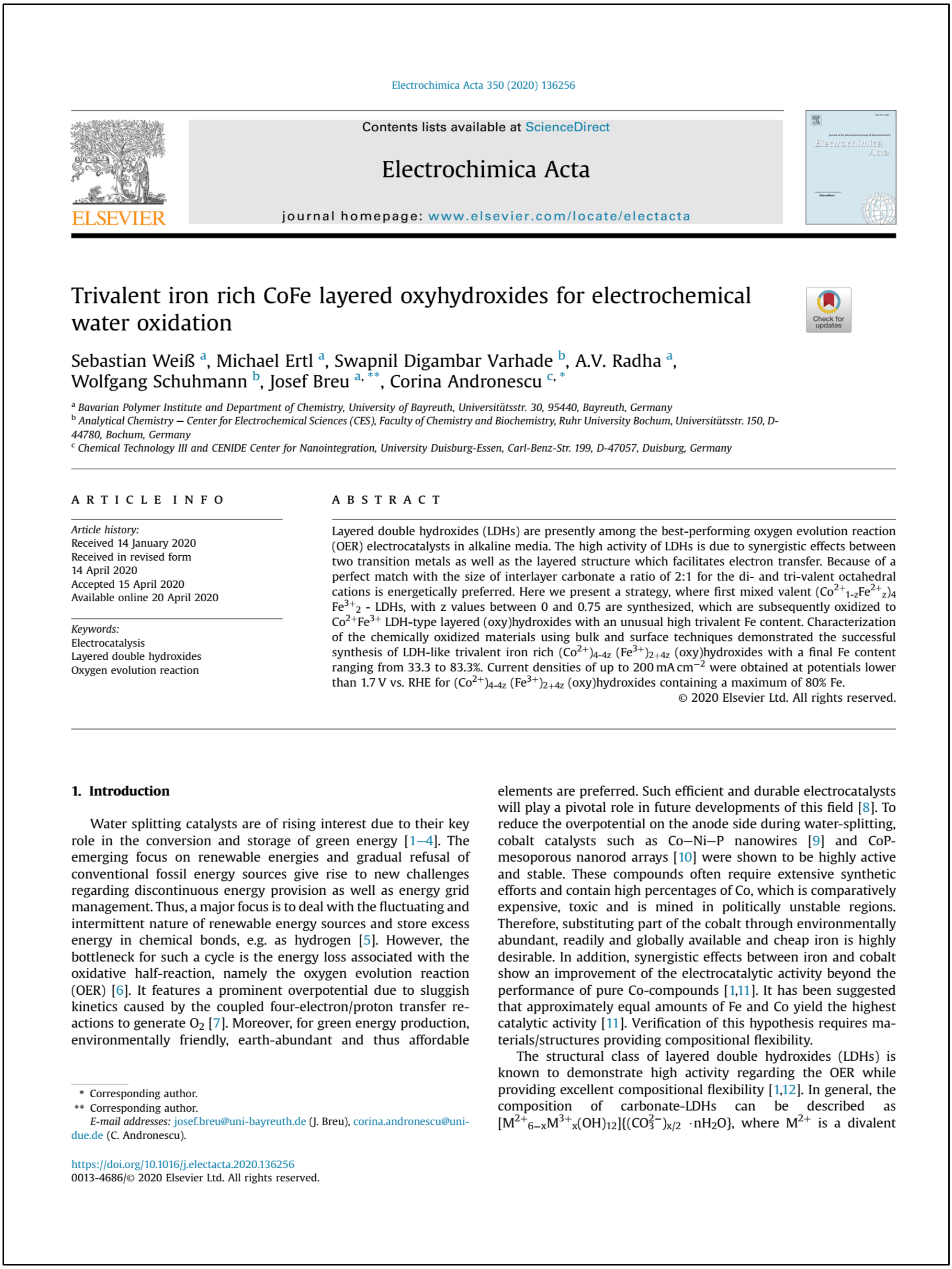

Electrochimica Acta 350 (2020) 136256

Contents lists available at ScienceDirect

Electrochimica Acta

journal homepage: www.elsevier.com/locate/electacta

Trivalent iron rich CoFe layered oxyhydroxides for electrochemical water oxidation

Sebastian Weiß [a], Michael Ertl [a], Swapnil Digambar Varhade [b], A.V. Radha [a],
Wolfgang Schuhmann [b], Josef Breu [a, **], Corina Andronescu [c, *]

[a] *Bavarian Polymer Institute and Department of Chemistry, University of Bayreuth, Universitätsstr. 30, 95440, Bayreuth, Germany*
[b] *Analytical Chemistry – Center for Electrochemical Sciences (CES), Faculty of Chemistry and Biochemistry, Ruhr University Bochum, Universitätsstr. 150, D-44780, Bochum, Germany*
[c] *Chemical Technology III and CENIDE Center for Nanointegration, University Duisburg-Essen, Carl-Benz-Str. 199, D-47057, Duisburg, Germany*

ARTICLE INFO

Article history:
Received 14 January 2020
Received in revised form
14 April 2020
Accepted 15 April 2020
Available online 20 April 2020

Keywords:
Electrocatalysis
Layered double hydroxides
Oxygen evolution reaction

ABSTRACT

Layered double hydroxides (LDHs) are presently among the best-performing oxygen evolution reaction (OER) electrocatalysts in alkaline media. The high activity of LDHs is due to synergistic effects between two transition metals as well as the layered structure which facilitates electron transfer. Because of a perfect match with the size of interlayer carbonate a ratio of 2:1 for the di- and tri-valent octahedral cations is energetically preferred. Here we present a strategy, where first mixed valent $(Co^{2+}{}_{1-z}Fe^{2+}{}_{z})_4$ $Fe^{3+}{}_2$ - LDHs, with z values between 0 and 0.75 are synthesized, which are subsequently oxidized to $Co^{2+}Fe^{3+}$ LDH-type layered (oxy)hydroxides with an unusual high trivalent Fe content. Characterization of the chemically oxidized materials using bulk and surface techniques demonstrated the successful synthesis of LDH-like trivalent iron rich $(Co^{2+})_{4-4z}$ $(Fe^{3+})_{2+4z}$ (oxy)hydroxides with a final Fe content ranging from 33.3 to 83.3%. Current densities of up to 200 mA cm^{-2} were obtained at potentials lower than 1.7 V vs. RHE for $(Co^{2+})_{4-4z}$ $(Fe^{3+})_{2+4z}$ (oxy)hydroxides containing a maximum of 80% Fe.

1. Introduction

Water splitting catalysts are of rising interest due to their key role in the conversion and storage of green energy [1–4]. The emerging focus on renewable energies and gradual refusal of conventional fossil energy sources give rise to new challenges regarding discontinuous energy provision as well as energy grid management. Thus, a major focus is to deal with the fluctuating and intermittent nature of renewable energy sources and store excess energy in chemical bonds, e.g. as hydrogen [5]. However, the bottleneck for such a cycle is the energy loss associated with the oxidative half-reaction, namely the oxygen evolution reaction (OER) [6]. It features a prominent overpotential due to sluggish kinetics caused by the coupled four-electron/proton transfer reactions to generate O_2 [7]. Moreover, for green energy production, environmentally friendly, earth-abundant and thus affordable elements are preferred. Such efficient and durable electrocatalysts will play a pivotal role in future developments of this field [8]. To reduce the overpotential on the anode side during water-splitting, cobalt catalysts such as Co–Ni–P nanowires [9] and CoP-mesoporous nanorod arrays [10] were shown to be highly active and stable. These compounds often require extensive synthetic efforts and contain high percentages of Co, which is comparatively expensive, toxic and is mined in politically unstable regions. Therefore, substituting part of the cobalt through environmentally abundant, readily and globally available and cheap iron is highly desirable. In addition, synergistic effects between iron and cobalt show an improvement of the electrocatalytic activity beyond the performance of pure Co-compounds [1,11]. It has been suggested that approximately equal amounts of Fe and Co yield the highest catalytic activity [11]. Verification of this hypothesis requires materials/structures providing compositional flexibility.

The structural class of layered double hydroxides (LDHs) is known to demonstrate high activity regarding the OER while providing excellent compositional flexibility [1,12]. In general, the composition of carbonate-LDHs can be described as $[M^{2+}{}_{6-x}M^{3+}{}_{x}(OH)_{12}]\{(CO_3^{2-})_{x/2}\cdot nH_2O\}$, where M^{2+} is a divalent

---

[*] Corresponding author.
[**] Corresponding author.
E-mail addresses: josef.breu@uni-bayreuth.de (J. Breu), corina.andronescu@uni-due.de (C. Andronescu).

https://doi.org/10.1016/j.electacta.2020.136256

and M^{3+} a trivalent metal species with x having values between 0 and 2 [13]. LDHs exhibit a layered morphology, are nanosized and may, moreover, be exfoliated providing significant surface areas and hence active sites for reactants, rendering them effective water-splitting catalysts [14–18]. Particularly their high flexibility towards substitution patterns with various metals renders them ideal to partially substitute some of the metal sites allowing for systematic variations of the composition [19]. For carbonate-LDHs, a ratio of M^{2+}:M^{3+} = 2:1 represents the thermodynamically most stable LDH composition because it corresponds to a dense packing of flat-lying carbonate anions in the interlayer space [20]. In this work, we consequently stick to this preferred charge density. As a trivalent cation Fe^{3+} is applied, while for M^{2+} various ratios of Co^{2+} and Fe^{2+} were chosen. Since mixed valent Fe-LDHs ("green rusts") are very sensitive to oxidation, the materials were subsequently converted to Fe^{3+}-only materials by fast oxidation with H_2O_2. This way LDH-type catalysts were obtained with Co^{2+}:Fe^{3+} ratios ranging from 2:1 to 1:5 that were tested for catalytic activity in OER.

2. Experimental details

2.1. Chemicals

Cobalt (II) chloride hexahydrate, iron (II) chloride tetrahydrate, iron (III) chloride hexahydrate, sodium carbonate, hydrochloric acid (32%), phosphoric acid (85%), nitric acid (70%), fluoroboric acid (48%), potassium hydroxide and Nafion 117 solution (5%) were purchased from Sigma-Aldrich and used as received. All solutions were prepared with Ar-saturated Milli-Q water. Hydrogen peroxide solution (30%) was supplied by VWR chemicals.

2.2. Catalyst material preparation

The mixed valence LDHs $[(Co^{2+}{}_{1-z}\,Fe^{2+}{}_{z})_4\,Fe^{3+}{}_2(OH)_{12}]\{(CO_3^{2-})\cdot n\,H_2O\}$ with $0 < z < 0.75$ were synthesized by a co-precipitation process. Corresponding amounts of metal chloride salts were dissolved in 50 mL Ar-saturated Milli-Q water yielding typically a total metal concentration of 0.4 M. 40 mL of a 1.0 M Na_2CO_3 solution was added in one shot to the metal salts solution inducing the precipitation of a carbonate interlayered LDH. After stirring the suspension for 30 min, 2 mL of 30% H_2O_2 solution were added. Please note: Neither 0.4 M $CoCl_2 \cdot 6H_2O$ nor a mixture of $FeCl_2 \cdot 4H_2O$ and $FeCl_3 \cdot 6H_2O$ can be precipitated upon addition of H_2O_2. This indicates that (oxy)hydroxides will not form under these conditions. After additional 10 min of stirring, the suspension was centrifuged and washed five times with water before freeze-drying. The nominal metal ratios used for the synthesis of the different CoFe-LDH samples as well as the final compositions of the obtained CoFe layered (oxy)hydroxides are presented in Tables 1 and 2.

Table 1
Nominal metal compositions used for synthesis $[(Co^{2+}{}_{1-z}\,Fe^{2+}{}_{z})_4\,Fe^{3+}{}_2(OH)_{12}]\{(CO_3^{2-})\cdot n\,H_2O\}$ with $0 < z < 0.75$ LDH intermediates.

Co^{2+}	Fe^{2+}	Fe^{3+}	M^{2+}/M^{3+}	Fe-ratio/%
1	3	2	2	83.3
1.2	2.8	2	2	80.0
1.5	2.5	2	2	75.0
2	2	2	2	66.7
3	1	2	2	50.0
4	0	2	2	33.3

Table 2
Metal compositions of final CoFe layered (oxy)hydroxide samples according to AAS data.

Sample	Co^{2+}	Fe^{3+}	Full formula
Co_1Fe_5	1	5	$[Co_1Fe_5(OH)_9O_3]CO_3$
$Co_{1\cdot 2}Fe_{4.8}$	1.2	4.8	$[Co_{1\cdot 2}Fe_{4\cdot 8}(OH)_{9\cdot 2}O_{2.8}]CO_3$
$Co_{1\cdot 5}Fe_{4.5}$	1.5	4.5	$[Co_{1\cdot 5}Fe_{4\cdot 5}(OH)_{9\cdot 5}O_{2.5}]CO_3$
Co_2Fe_4	2	4	$[Co_2Fe_4(OH)_{10}O_2]CO_3$
Co_3Fe_3	3	3	$[Co_3Fe_3(OH)_{11}O_1]CO_3$
Co_4Fe_2	4	2	$[Co_4Fe_2(OH)_{12}O_0]CO_3$

2.3. Structural characterization of the materials

Powder X-ray diffraction (XRD) patterns were recorded with Ag Kα radiation (λ = 0.5594 Å) in transition mode applying a STOE Stadi P equipped with four MYTHEN2 R 1 K detectors. XRD patterns can be indexed according to PDF#50–0235 reported for CoFe-LDH [1]. The infrared (IR) spectra of the powder samples were recorded using a JASCO FTIR 6100 spectrometer (400-4000 cm^{-1} range, 4 cm^{-1} resolution). The specific surface area was measured with a Quantochrome Nova A with N_2 as adsorbate at 77 K applying the Brunauer-Emmet-Teller (BET) method. Transmission electron microscopy (TEM) images were registered using a Zeiss/LEO EM922 Ω transmission electron microscope. Scanning electron microscopy (SEM) images were acquired using a Zeiss/LEO 1530 system. Fe and Co concentrations were determined by atomic absorption spectroscopy (AAS) applying a Varian AA100 spectrometer. For this, 20 mg of the compounds were dissolved in an acidic solution of HCl (3 mL), H_3PO_4 (1.5 mL), HNO_3 (1.5 mL) and HBF_4 (2 mL) and diluted with water to a volume of 100 mL. X-ray photoelectron spectra (XPS) were recorded using a Versa Probe III from Physical Electronics. Copper and gold were used for calibration. Shirley-type background-subtracted data is presented.

2.4. Electrochemical characterization

The catalyst ink was prepared by dispersing 1 mg powder catalyst in 0.2 mL solvent mixture (0.004 mL Nafion solution, 0.098 mL ethanol, 0.098 mL water) by 30 min sonication generating a stable suspension (5 mg/mL). A certain volume of the ink was drop-coated on the glassy carbon electrode ($A_{electrode} = 0.1134\ cm^2$) to obtain a mass loading of 0.2 mg cm^{-2} catalyst. Rotating disk electrode measurements were carried out in a standard three-electrode setup using an Autolab Potentiostat/Galvanostat PGSTAT128 N with a platinum mesh as counter electrode, a Ag/AgCl (3 M KCl) reference electrode and the catalyst modified glassy carbon electrode as working electrode. The counter electrode was separated from the bulk electrolyte by a glass frit and all electrochemical measurements were performed in O_2 saturated 1 M KOH solution. Purified electrolyte was used for all electrochemical measurements using a cation-exchange resin – Chelex 100 (Bio-Rad Laboratories) following the procedure recommended by the producer. The uncompensated resistance was determined from electrochemical impedance spectroscopy (EIS) recorded in the frequency range from 100 kHz –100 Hz with an AC perturbation voltage of 10 mV (RMS) at open circuit voltage. Linear sweep voltammograms (LSVs) were further recorded in the potential window from 0 to 1 V vs. Ag/AgCl (3 M KCl) at a scan rate of 5 mVs^{-1} and at 1600 rpm (before cycling). In order to have a fast hint on the catalyst stability during OER, 10 CVs were further recorded in the same potential window at a scan rate of 100 mVs^{-1}. Following this, a second LSV was recorded at a scan rate of 5 mVs^{-1} and this LSV was named "after cycling".

The potentials measured vs. Ag/AgCl (3 M KCl) were converted to the RHE scale and corrected for the uncompensated resistance using the formula:

$$E_{RHE} = E_{Ag/AgCl} + E°_{Ag/AgCl(3M\ KCl)} + 0.059*pH - iR$$

Where: E_{RHE} is the potential (in V) vs. RHE, $E_{Ag/AgCl}$ is the applied potential (in V) vs. Ag/AgCl (3 M KCl), $E^0_{Ag/AgCl\ (3\ M\ KCl)}$ is the formal potential of Ag/AgCl (3 M KCl) (in V), *i* is the registered current (in A) and R is the solution resistance (in Ω), which was derived from EIS (high frequency range).

The electrochemical surface area (ECSA) was calculated following the report of McCrory et al. [21] Cyclic voltammograms were recorded in the non-Faradaic region at scan rates (ν) of 0.005, 0.01, 0.025, 0.05, 0.1 and 0.2 Vs^{-1} in the potential window calculated as open circuit potential (OCP) ± 0.05 V. The electrochemical double layer capacitance was calculated using the formula: $C_{DL} = i \cdot \nu^{-1}$ where i is the current recorded at a defined potential at different ν. For ECSA calculation the following formula was used: $ECSA = C_{DL} \cdot C_S^{-1}$, where C_s is the specific capacitance which was in this manuscript approximated with 0.04 mF cm^{-2} [21].

3. Results and discussion

The co-precipitation of different ratios of Co^{2+}, Fe^{2+} and Fe^{3+} chloride salts yielded carbonate interlayered LDHs with the preferred $(Co^{2+}+Fe^{2+})/Fe^{3+}$ ratio equal to 2 and a total nominal Fe content varying between 83.3 and 33.3% (Table 1). Mixed valence green rust type LDH materials are known to be prone to slow oxidation in suspension or at ambient oxygen fugacity whereupon the materials eventually transform into goethite [22]. Due to this sensitivity to oxidation the materials were, without isolation of this precursor, directly oxidized by addition of H_2O_2 to layered mössbauerite-type all Fe^{3+} materials according to our recently reported procedure [23]. To preserve the LDH structure at ambient conditions this rather fast and complete chemical oxidation to Fe^{3+} is required. Thus, all materials tested for electrocatalysis are mössbauerite-type Fe^{3+} only materials.

The CoFe layered (oxy)hydroxide materials contain Co^{2+} and Fe^{3+}, they are stable and can be handled in atmosphere without any precautions. Charge compensation upon oxidation is accomplished by partial deprotonation of structural hydroxyl groups [24]. The compositions of oxidized products were analyzed by means of AAS and were consistent with nominal ratios of the metal salts within experimental errors (Table 2).

All observed diffraction peaks (Fig. 1) located at 4.1°, 8.3°, 12.2°, 13.8°, 16.4°, 20.6° and 21.1° can be indexed with the unit cell published for CoFe-LDH (PDF#50−0235) as (*003*), (*006*), (*012*), (*015*), (*018*) (*110*) and (*113*) planes, respectively. The interlayer d-spacing determined based on the *003* reflection is 7.8 Å for Co_4Fe_2, which is in good agreement with the value for a CO_3^{2-} intercalated LDH [25]. Kim et al. [26] observed a pronounced broadening of reflections with decreasing cobalt content. The effect became very noticeable when the Co-content is decreased to 60% [26]. We observe a significant broadening only starting from less than 25% cobalt ($Co_{1.5}Fe_{4.5}$, $Co_{1.2}Fe_{4.8}$, Co_1Fe_5). We attribute this improvement to our specific synthesis protocol that initially applies strictly the preferred 2:1 ratio of M^{2+}:M^{3+}. This synthesis protocol contrasts with previous reports where the materials with different Co/Fe-ratios were synthesized using a one-step approach involving only Co^{2+} and Fe^{3+} salts [26,27], which implies a significant deviation from the preferred 2:1 ratio of M^{2+}:M^{3+} for carbonate-LDHs.

The *003* reflection is first gradually shifted from 7.8 Å to a minimum of 6.4 Å with increasing Fe^{3+}-content (Co_4Fe_2, Co_3Fe_3, Co_2Fe_4) and then increases again to 7.5 Å when further increasing the Fe^{3+}-content ($Co_{1.5}Fe_{4.5}$, $Co_{1.2}Fe_{4.8}$, Co_1Fe_5). These shifts are accompanied by variations in the peak widths and the rationality of the *00l*-series. We have previously shown that the oxidation of mixed valence Fe-LDHs triggers partial grafting of interlayer carbonate to the brucite layers [28]. According to ab-initio modelling, the completely grafted structure is expected to have a significantly smaller basal spacing (6.9 Å) than the non-grafted LDH (7.2 Å) [28]. The above shifts may therefore be related to interstratified real structures composed of a random interstratification of varying amounts of grafted and non-grafted interlayers. The variation of peak widths and irrational *00l*-series could also be explained by such an interstratification. According to the Hall−Williamson method, thickness related broadening would increase FWHM of *00l* peaks systematically with cos θ. We observed, however, a non-systematic broadening, which clearly is related to the effects of statistical interstratification as described by Mering's rules [29]. For instance, for sample Co_3Fe_3 the FWHM of the *006* (0.272°) is smaller than the FWHM of the *003* (0.305°).

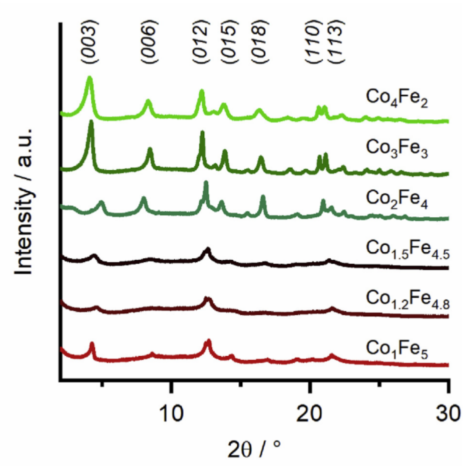

Fig. 1. XRD patterns acquired for the different CoFe layered (oxy)hydroxide samples. The cobalt-content decreases from top to bottom. Differences in peak positions and sharpness can be observed depending on the metal compositions of the materials.

Refinement of these real structures is tedious and time-consuming and thus beyond the scope of this paper. Grafting with some of the CoFe layered (oxy)hydroxides is additionally qualitatively supported by Fourier-transform infrared spectroscopy (FT-IR) as discussed below.

Concomitantly, planar defects in the stacking of adjacent layers vary with composition as indicated by the shape and the relative intensity of cross-reflections, e.g. *110*. The *110* reflection for the cobalt-rich samples Co_4Fe_2, Co_3Fe_3 and Co_2Fe_4 is symmetrical and intense indicating few to null planar defects while it becomes lambda-shaped and less intense for samples $Co_{1.5}Fe_{4.5}$, $Co_{1.2}Fe_{4.8}$ and Co_1Fe_5 indicating a turbostratic stacking with no defined phase relationship of adjacent layers in the stack.

The oxidation state of Co and Fe of the CoFe layered (oxy)hydroxide catalyst was verified by XPS (Fig. 2). The binding energies were calibrated using the peak corresponding to the C 1s adventitious carbon located at 284.8 eV as reference. Although deconvolution of the Co 2p and Fe 2p peaks is hampered by the low signal to noise ratio of the recorded spectra, both Co and Fe can safely be

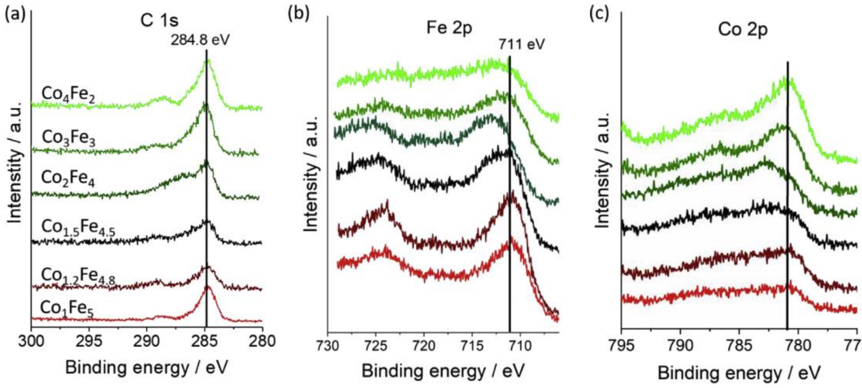

Fig. 2. High resolution XPS spectra of CoFe layered (oxy)hydroxide samples recorded in the (a) C 1s, (b) Fe 2p and (c) Co 2p regions.

assigned to oxidation states Co^{2+} and Fe^{3+}, respectively. For Fe the main peak is observed at BE ~711 eV, which is in good agreement with values reported for FeOOH [30]. XPS cannot provide evidence for the formal oxidation state of Co. We can, however, indirectly conclude on it: In a previous publication on iron-only mössbauerite we have presented Mössbauer spectroscopy showing complete oxidation to Fe^{3+} by means of H_2O_2 [23]. It is sensible to assume that Fe oxidation is also complete in the CoFe samples as presented in this manuscript. Moreover, we see a clear oxidation peak in the first linear sweep voltammogram (Fig. 4b) which, depending on the Co content, is located at potentials between 1.2 and 1.4 V vs RHE and which corresponds to the oxidation of Co^{2+} [11].

All CoFe layered (oxy)hydroxides come in irregularly shaped platy crystals with rounded corners (TEM-images: Fig. S1 and SEM-images: Fig. S2). The degree of inter-growth of platelets varied with composition. Samples with high iron content featured more individual, particular platelets, whereas an increase in the cobalt ratio leads to an increasing inter-growth of the platelets to aggregates (Fig. S2) into rose-like morphologies quite typical for LDHs. Size distributions of all CoFe layered (oxy)hydroxides catalyst samples was determined by TEM through averaging over multiple crystals (Fig. S1). Within errors, the disordered crystals feature similar average dimensions as the less disordered samples. However, the irregular shape results in a high intra-sample variability with lateral dimension ranging from 50 nm up to 275 nm with a thickness of 20 nm for the platy crystals. For the specimen with the highest content of Co, the size determination was not feasible because of the strong intergrowth and formation of bigger aggregates (Figs. S1 and S2).

The specific surface area of all samples was determined using the Brunauer-Emmett-Teller method (Table 3) [31]. Co_1Fe_5, featuring the highest iron content, exhibited the largest specific surface area with 242.1 $m^2 g^{-1}$, while sample $Co_{1.5}Fe_{4.5}$ exhibited the lowest with 98.3 $m^2 g^{-1}$. As the iron content decreases, the surface area decreases from sample Co_1Fe_5 to $Co_{1.5}Fe_{4.5}$ and then increases again from samples Co_2Fe_4 to Co_4Fe_2.

Table 3
BET-data and the calculated electrochemical surface areas (ECSA) of the samples with various compositions.

Sample	BET surface area/$cm^2 g^{-1}$	ECSA/cm^2
Co_1Fe_5	242.1	0.389 ± 0.004
$Co_{1.2}Fe_{4.8}$	114.1	0.322 ± 0.032
$Co_{1.5}Fe_{4.5}$	98.3	0.735 ± 0.024
Co_2Fe_4	106.3	0.561 ± 0.048
Co_3Fe_3	106.5	0.424 ± 0.014
Co_4Fe_2	147.8	0.797 ± 0.034

UV Vis/DRS spectra of all CoFe layered (oxy)hydroxide materials (Fig. S3) showed a prominent semiconductor transition with no obvious localized transitions. The bandgaps vary slightly between 1.8 and 1.6 eV for the direct and 1.5 and 1.7 eV for the indirect transitions. No clear trend can be recognized depending on the composition. The trend could, however, be masked as the values might be shifted slightly due to the Urbach tail. This phenomenon originates from less crystalline domains or defect states and is frequently encountered in semiconducting materials [32].

To verify the presence of grafted carbonate as opposed to simply intercalated carbonate as indicated by XRD, FT-IR spectra were analyzed (Fig. 3). For all synthesized materials a broad band located

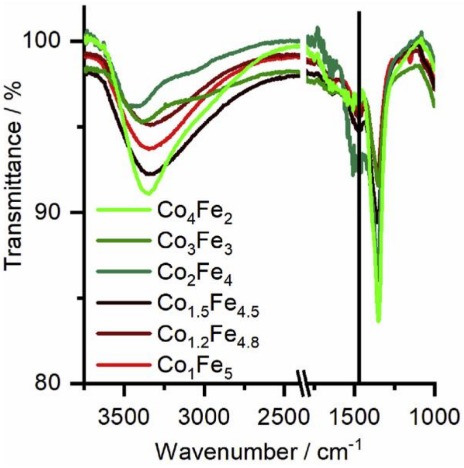

Fig. 3. FT-IR spectra of the synthesized CoFe layered (oxy)hydroxides samples. The inset shows the regional characteristic for the carbonate. The splitting of the ν_3 band of carbonate with an energy difference of ~120 cm^{-1} is an indication for the monodentate carbonate in Co_2Fe_4, $Co_{1.5}Fe_{4.5}$, $Co_{1.2}Fe_{4.8}$ and Co_1Fe_5. Particularly Co_2Fe_4 exhibits pronounced band splitting. Contrarily, Co_4Fe_2 and Co_3Fe_3 show almost no band splitting.

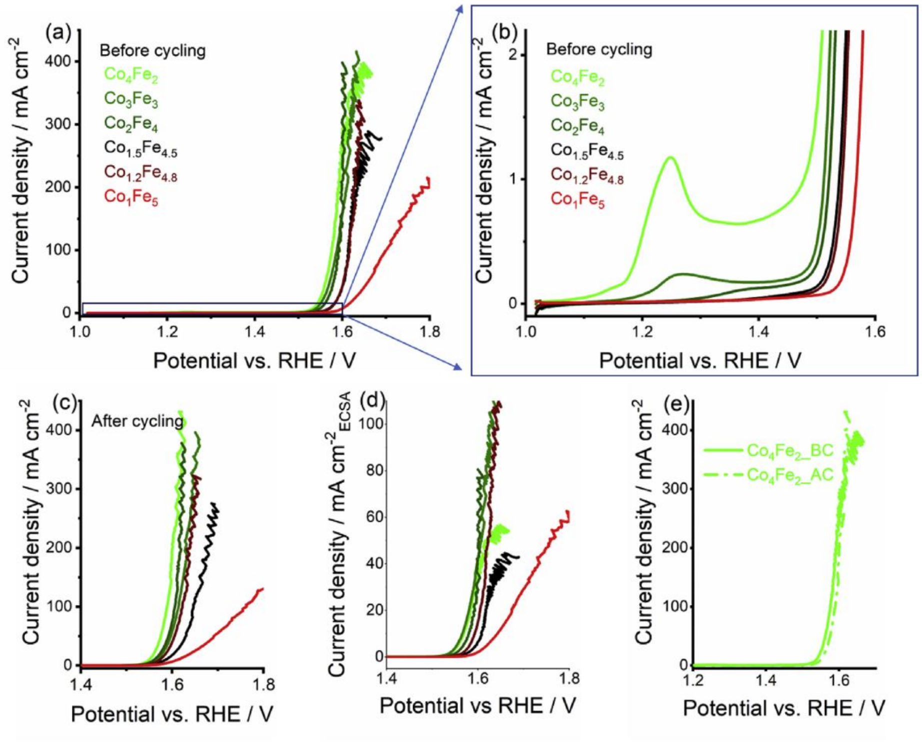

Fig. 4. Electrochemical data recorded for the synthesized CoFe layered (oxy)hydroxides catalyst samples using RDE experiments in O_2 saturated 1 M KOH solution with 1600 rpm and 5 mV s^{-1} scan rate: (a) First linear sweep voltammograms recorded (before cycling), (b) zoom of Fig. 4 (a) in the low region current part, (c) Linear sweep voltammograms recorded after performing 10 CVs with 100 mv s^{-1} (after cycling), (d) first linear sweep voltammograms recorded (before cycling) where the current densities were calculated using the electrochemical surface area and (e) comparison of the initially most active electrocatalyst Co_4Fe_2 before and after the electrochemical cycling.

at 3650 - 3200 cm^{-1} corresponding to the O—H stretching vibration mode of water and hydroxyl groups was observed. The signal at 3000 cm^{-1}, which was for most samples only visible as a shoulder, is attributed to the hydroxyl interactions with carbonate and ions in the interlayer [33]. At 1611 cm^{-1}, the bending mode of interlayer water is visible. Carbonate ions located in the interlayer space with D_{3h} symmetry were confirmed by the presence of characteristic bands at 1382 cm^{-1} and 1350 cm^{-1} corresponding to asymmetric stretching modes of CO_3^{2-} [26,34]. A splitting of the ν_3 band into 1470 cm^{-1} and 1350 cm^{-1} can be clearly observed in the iron-rich samples Co_1Fe_5, $Co_{1.2}Fe_{4.8}$, $Co_{1.5}Fe_{4.5}$ and Co_2Fe_4. The identification of such ν_3 band splitting with an energy difference of 120 cm^{-1} indicates a lowering of the symmetry from D_{3h} to C_{2v} and has previously been assigned to monodentate carbonate. Thus, it provides qualitative evidence of interlayer carbonate grafted to the layers [28]. In contrast, the Co-rich samples Co_4Fe_2 and Co_3Fe_3 show little to no band splitting indicating free interlayer carbonate in D_{3h} symmetry and no grafted carbonate. Interestingly, XRD indicated that these samples suffer least of planar defects and interstratification, suggesting that grafting might be directly related to defect concentration.

The electrocatalytic activity towards the OER of the synthesized trivalent Fe-rich CoFe layered (oxy)hydroxide materials was assessed by means of linear sweep voltammetry in rotating disk electrode experiments. The lowest electrocatalytic activity was registered when Co_1Fe_5 was used as electrocatalyst, this being the only case when a current of up to 200 mA cm^{-2} could not be reached. Interestingly, the small increase of the Co content in $Co_{1.2}Fe_{4.8}$ leads to a tremendous boost of the activity, despite the surface area of the sample, determined from BET measurements, being almost 2 times lower than of that of sample Co_1Fe_5 (Table 3). Also, by normalizing the recorded currents to the ECSA, Co_1Fe_5 shows the lowest activity of all measured samples (Fig. 4d). Taking only minor structural differences between these two samples into consideration, as suggested by XRD and TEM data, it can be concluded that a critical amount of Co is necessary in order to boost the electrochemical activity of the CoFe layered (oxy)hydroxides. A further increase in Co content leads to an increased catalytic activity with the maximum value reached for Co_4Fe_2 or Co_3Fe_3, depending if the current normalization is performed by the geometric surface area (Fig. 4a) or by the ECSA (Fig. 4d), respectively. While at lower current densities (10 mA cm^{-2}) no significant difference can be observed between Co_2Fe_4, Co_3Fe_3 and Co_4Fe_2, the difference becomes more visible at high current densities (Fig. 4 a, Table 4). Normalization of the currents by the ECSA instead of the geometric area of the electrode is not significantly impacting the observed trend (Fig. 4 a vs. 4 d). After running 10 CVs at a scan rate of 100 mV s^{-1} in the same potential window, an additional LSV was

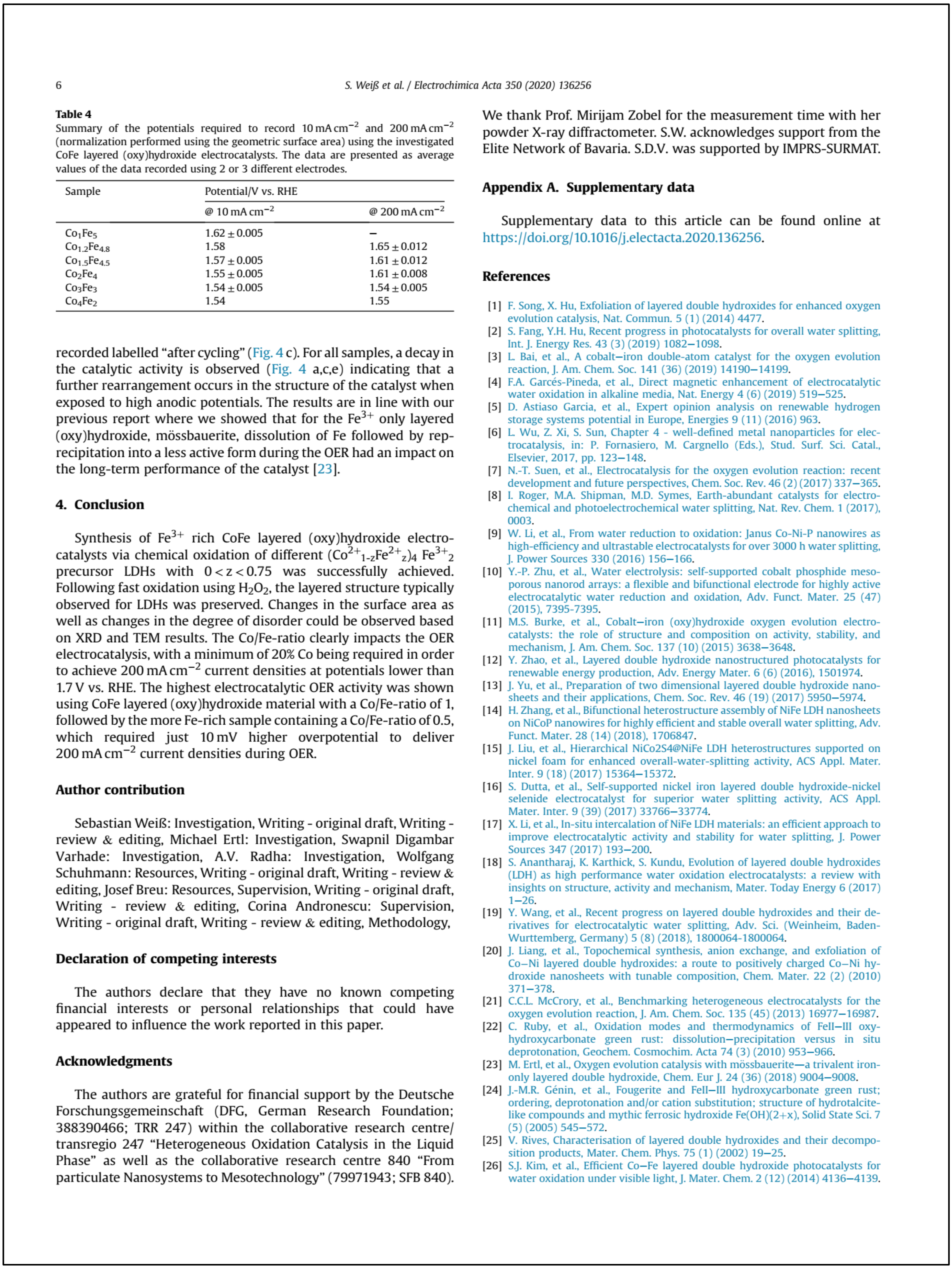

Table 4
Summary of the potentials required to record 10 mA cm^{-2} and 200 mA cm^{-2} (normalization performed using the geometric surface area) using the investigated CoFe layered (oxy)hydroxide electrocatalysts. The data are presented as average values of the data recorded using 2 or 3 different electrodes.

Sample	Potential/V vs. RHE	
	@ 10 mA cm^{-2}	@ 200 mA cm^{-2}
Co_1Fe_5	1.62 ± 0.005	–
$Co_{1.2}Fe_{4.8}$	1.58	1.65 ± 0.012
$Co_{1.5}Fe_{4.5}$	1.57 ± 0.005	1.61 ± 0.012
Co_2Fe_4	1.55 ± 0.005	1.61 ± 0.008
Co_3Fe_3	1.54 ± 0.005	1.54 ± 0.005
Co_4Fe_2	1.54	1.55

recorded labelled “after cycling” (Fig. 4 c). For all samples, a decay in the catalytic activity is observed (Fig. 4 a,c,e) indicating that a further rearrangement occurs in the structure of the catalyst when exposed to high anodic potentials. The results are in line with our previous report where we showed that for the Fe^{3+} only layered (oxy)hydroxide, mössbauerite, dissolution of Fe followed by reprecipitation into a less active form during the OER had an impact on the long-term performance of the catalyst [23].

4. Conclusion

Synthesis of Fe^{3+} rich CoFe layered (oxy)hydroxide electrocatalysts via chemical oxidation of different $(Co^{2+}{}_{1-z}Fe^{2+}{}_z)_4$ $Fe^{3+}{}_2$ precursor LDHs with $0 < z < 0.75$ was successfully achieved. Following fast oxidation using H_2O_2, the layered structure typically observed for LDHs was preserved. Changes in the surface area as well as changes in the degree of disorder could be observed based on XRD and TEM results. The Co/Fe-ratio clearly impacts the OER electrocatalysis, with a minimum of 20% Co being required in order to achieve 200 mA cm^{-2} current densities at potentials lower than 1.7 V vs. RHE. The highest electrocatalytic OER activity was shown using CoFe layered (oxy)hydroxide material with a Co/Fe-ratio of 1, followed by the more Fe-rich sample containing a Co/Fe-ratio of 0.5, which required just 10 mV higher overpotential to deliver 200 mA cm^{-2} current densities during OER.

Author contribution

Sebastian Weiß: Investigation, Writing - original draft, Writing - review & editing, Michael Ertl: Investigation, Swapnil Digambar Varhade: Investigation, A.V. Radha: Investigation, Wolfgang Schuhmann: Resources, Writing - original draft, Writing - review & editing, Josef Breu: Resources, Supervision, Writing - original draft, Writing - review & editing, Corina Andronescu: Supervision, Writing - original draft, Writing - review & editing, Methodology,

Declaration of competing interests

The authors declare that they have no known competing financial interests or personal relationships that could have appeared to influence the work reported in this paper.

Acknowledgments

The authors are grateful for financial support by the Deutsche Forschungsgemeinschaft (DFG, German Research Foundation; 388390466; TRR 247) within the collaborative research centre/transregio 247 “Heterogeneous Oxidation Catalysis in the Liquid Phase” as well as the collaborative research centre 840 “From particulate Nanosystems to Mesotechnology” (79971943; SFB 840). We thank Prof. Mirijam Zobel for the measurement time with her powder X-ray diffractometer. S.W. acknowledges support from the Elite Network of Bavaria. S.D.V. was supported by IMPRS-SURMAT.

Appendix A. Supplementary data

Supplementary data to this article can be found online at https://doi.org/10.1016/j.electacta.2020.136256.

References

[1] F. Song, X. Hu, Exfoliation of layered double hydroxides for enhanced oxygen evolution catalysis, Nat. Commun. 5 (1) (2014) 4477.
[2] S. Fang, Y.H. Hu, Recent progress in photocatalysts for overall water splitting, Int. J. Energy Res. 43 (3) (2019) 1082–1098.
[3] L. Bai, et al., A cobalt–iron double-atom catalyst for the oxygen evolution reaction, J. Am. Chem. Soc. 141 (36) (2019) 14190–14199.
[4] F.A. Garcés-Pineda, et al., Direct magnetic enhancement of electrocatalytic water oxidation in alkaline media, Nat. Energy 4 (6) (2019) 519–525.
[5] D. Astiaso Garcia, et al., Expert opinion analysis on renewable hydrogen storage systems potential in Europe, Energies 9 (11) (2016) 963.
[6] L. Wu, Z. Xi, S. Sun, Chapter 4 - well-defined metal nanoparticles for electrocatalysis, in: P. Fornasiero, M. Cargnello (Eds.), Stud. Surf. Sci. Catal., Elsevier, 2017, pp. 123–148.
[7] N.-T. Suen, et al., Electrocatalysis for the oxygen evolution reaction: recent development and future perspectives, Chem. Soc. Rev. 46 (2) (2017) 337–365.
[8] I. Roger, M.A. Shipman, M.D. Symes, Earth-abundant catalysts for electrochemical and photoelectrochemical water splitting, Nat. Rev. Chem. 1 (2017), 0003.
[9] W. Li, et al., From water reduction to oxidation: Janus Co-Ni-P nanowires as high-efficiency and ultrastable electrocatalysts for over 3000 h water splitting, J. Power Sources 330 (2016) 156–166.
[10] Y.-P. Zhu, et al., Water electrolysis: self-supported cobalt phosphide mesoporous nanorod arrays: a flexible and bifunctional electrode for highly active electrocatalytic water reduction and oxidation, Adv. Funct. Mater. 25 (47) (2015), 7395-7395.
[11] M.S. Burke, et al., Cobalt–iron (oxy)hydroxide oxygen evolution electrocatalysts: the role of structure and composition on activity, stability, and mechanism, J. Am. Chem. Soc. 137 (10) (2015) 3638–3648.
[12] Y. Zhao, et al., Layered double hydroxide nanostructured photocatalysts for renewable energy production, Adv. Energy Mater. 6 (6) (2016), 1501974.
[13] J. Yu, et al., Preparation of two dimensional layered double hydroxide nanosheets and their applications, Chem. Soc. Rev. 46 (19) (2017) 5950–5974.
[14] H. Zhang, et al., Bifunctional heterostructure assembly of NiFe LDH nanosheets on NiCoP nanowires for highly efficient and stable overall water splitting, Adv. Funct. Mater. 28 (14) (2018), 1706847.
[15] J. Liu, et al., Hierarchical NiCo2S4@NiFe LDH heterostructures supported on nickel foam for enhanced overall-water-splitting activity, ACS Appl. Mater. Inter. 9 (18) (2017) 15364–15372.
[16] S. Dutta, et al., Self-supported nickel iron layered double hydroxide-nickel selenide electrocatalyst for superior water splitting activity, ACS Appl. Mater. Inter. 9 (39) (2017) 33766–33774.
[17] X. Li, et al., In-situ intercalation of NiFe LDH materials: an efficient approach to improve electrocatalytic activity and stability for water splitting, J. Power Sources 347 (2017) 193–200.
[18] S. Anantharaj, K. Karthick, S. Kundu, Evolution of layered double hydroxides (LDH) as high performance water oxidation electrocatalysts: a review with insights on structure, activity and mechanism, Mater. Today Energy 6 (2017) 1–26.
[19] Y. Wang, et al., Recent progress on layered double hydroxides and their derivatives for electrocatalytic water splitting, Adv. Sci. (Weinheim, Baden-Wurttemberg, Germany) 5 (8) (2018), 1800064-1800064.
[20] J. Liang, et al., Topochemical synthesis, anion exchange, and exfoliation of Co–Ni layered double hydroxides: a route to positively charged Co–Ni hydroxide nanosheets with tunable composition, Chem. Mater. 22 (2) (2010) 371–378.
[21] C.C.L. McCrory, et al., Benchmarking heterogeneous electrocatalysts for the oxygen evolution reaction, J. Am. Chem. Soc. 135 (45) (2013) 16977–16987.
[22] C. Ruby, et al., Oxidation modes and thermodynamics of FeII–III oxyhydroxycarbonate green rust: dissolution–precipitation versus in situ deprotonation, Geochem. Cosmochim. Acta 74 (3) (2010) 953–966.
[23] M. Ertl, et al., Oxygen evolution catalysis with mössbauerite—a trivalent iron-only layered double hydroxide, Chem. Eur J. 24 (36) (2018) 9004–9008.
[24] J.-M.R. Génin, et al., Fougerite and FeII–III hydroxycarbonate green rust; ordering, deprotonation and/or cation substitution; structure of hydrotalcite-like compounds and mythic ferrosic hydroxide Fe(OH)(2+x), Solid State Sci. 7 (5) (2005) 545–572.
[25] V. Rives, Characterisation of layered double hydroxides and their decomposition products, Mater. Chem. Phys. 75 (1) (2002) 19–25.
[26] S.J. Kim, et al., Efficient Co–Fe layered double hydroxide photocatalysts for water oxidation under visible light, J. Mater. Chem. 2 (12) (2014) 4136–4139.

[27] L. Feng, et al., A highly active CoFe layered double hydroxide for water splitting, ChemPlusChem 82 (3) (2017) 483–488.

[28] P. Lyu, et al., Structure determination of the oxygen evolution catalyst mössbauerite, J. Phys. Chem. C 123 (41) (2019) 25157–25165.

[29] D.M. Moore, R.C. Reynolds, X-ray Diffraction and the Identification and Analysis of Clay Minerals, Oxford University Press, 1989.

[30] F. Yang, et al., Synergistic effect of cobalt and iron in layered double hydroxide catalysts for the oxygen evolution reaction, ChemSusChem 10 (1) (2017) 156–165.

[31] S. Brunauer, P.H. Emmett, E. Teller, Adsorption of gases in multimolecular layers, J. Am. Chem. Soc. 60 (2) (1938) 309–319.

[32] D.J. Dunstan, Evidence for a common origin of the Urbach tails in amorphous and crystalline semiconductors, J. Phys. C Solid State Phys. 15 (13) (1982) L419–L424.

[33] S.J. Palmer, R.L. Frost, T. Nguyen, Hydrotalcites and their role in coordination of anions in Bayer liquors: anion binding in layered double hydroxides, Coord. Chem. Rev. 253 (1) (2009) 250–267.

[34] M.A. Oliver-Tolentino, et al., An approach to understanding the electrocatalytic activity enhancement by superexchange interaction toward OER in alkaline media of Ni–Fe LDH, J. Phys. Chem. C 118 (39) (2014) 22432–22438.

Supporting Information

Trivalent Iron rich CoFe Layered Oxyhydroxides for Electrochemical Water Oxidation

1. Electron micrographs

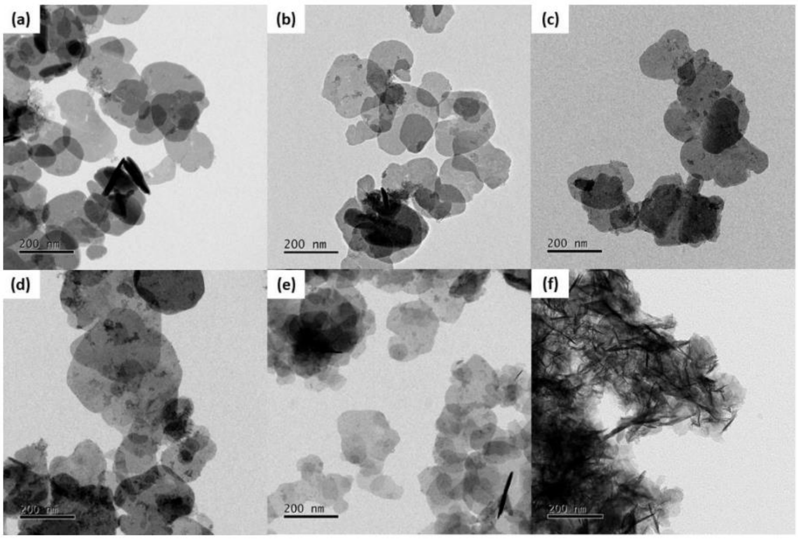

Figure S1: TEM micrographs of the CoFe layered (oxy)hydroxides materials with various compositions. The micrographs depict the following samples: (a) Co_1Fe_5*, (b)* $Co_{1.2}Co_{4.8}$*, (c)* $Co_{1.5}Co_{4.5}$*, (d)* Co_2Fe_4*, (e)* Co_3Fe_3 *and (f)* Co_4Fe_2*. The change in composition is accompanied by a morphological alteration of the sample which is most evident in (f) due to the strong intergrowth of the crystals.*

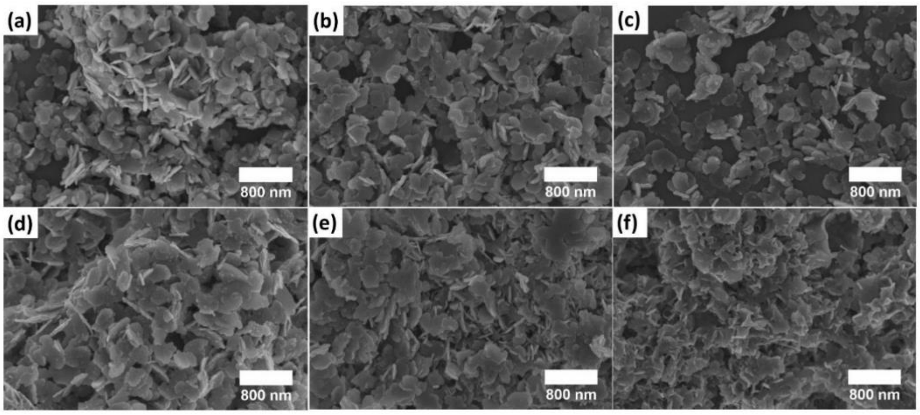

Figure S2: SEM micrographs of the CoFe layered (oxy)hydroxides materials with various composition. The micrographs depict the following samples: (a) Co_1Fe_5*, (b)* $Co_{1.2}Co_{4.8}$*, (c)* $Co_{1.5}Co_{4.5}$*, (d)* Co_2Fe_4*, (e)* Co_3Fe_3 *and (f)* Co_4Fe_2*. The change in composition is accompanied by a morphological alteration of the sample which is most evident in (f) due to the strong intergrowth of the crystals.*

2. UV Vis Diffuse Reflectance Spectroscopy (UV Vis/DRS)

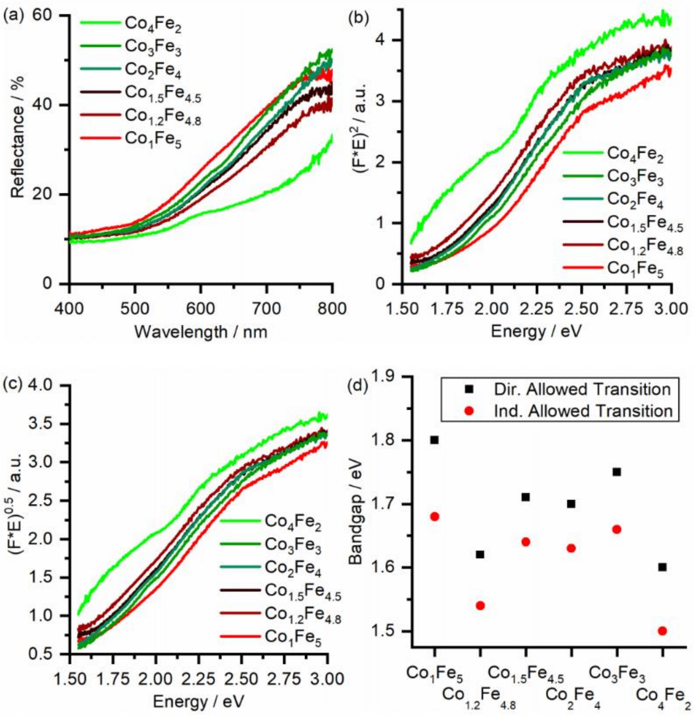

Figure S3: UV Vis DRS spectral analysis of the CoFe layered (oxy)hydroxide materials (a). The direct (b) and indirect bandgap transitions (c) are determined using a Tauc plot with the Kubelka-Munk formula. The results are summarized (d).

6.2 Influence of Grafting on the electrocatalytic capabilities of layered materials

The Effect of Interlayer Anion Grafting on Water Oxidation Electrocatalysis: A Comparative Study of Ni- and Co-Based Brucite-Type Layered Hydroxides, Layered Double Hydroxides and Hydroxynitrate Salts

A. V. Radha[+a], Sebastian Weiß[+a,b], Ignacio Sanjuán[+c], Michael Ertl[a], Corina Andronescu[*c] and Josef Breu[*a,b]

Published in Chemistry – A European Journal **2021**, 27, 16930-16937.

Impact Factor (2023) Chemistry – A European Journal: 5.236
DOI: 10.1002/chem.202100452

[a] Department of Chemistry, University of Bayreuth, Universitätsstr. 30, 95447 Bayreuth (Germany)

[b] Bavarian Center for Battery Technology (BayBatt), University of Bayreuth, Universitätsstr. 30, 95447 Bayreuth (Germany)

[c] Technical Technology III and Center for Nanointegration (CENIDE), University Duisburg-Essen, Carl-Benz-Str. 199, 47057 Duisburg (Germany)

[+] These authors contributed equally to this work.

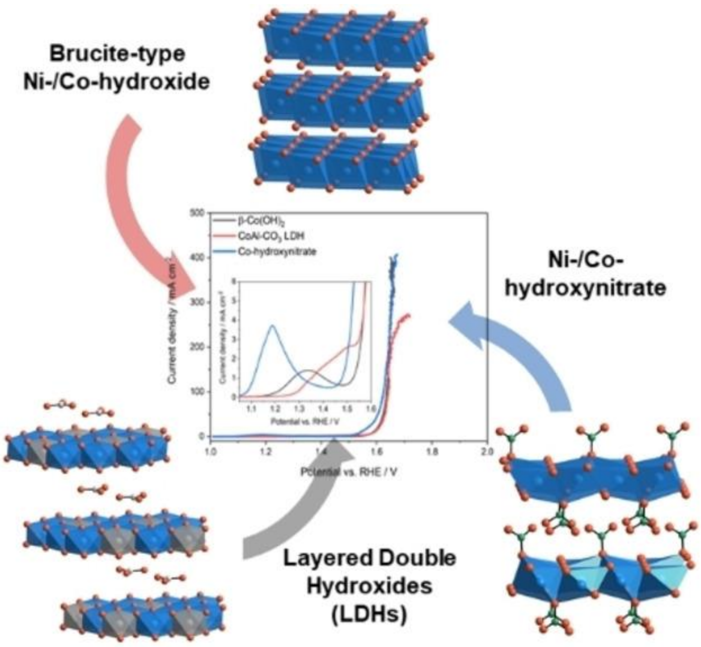

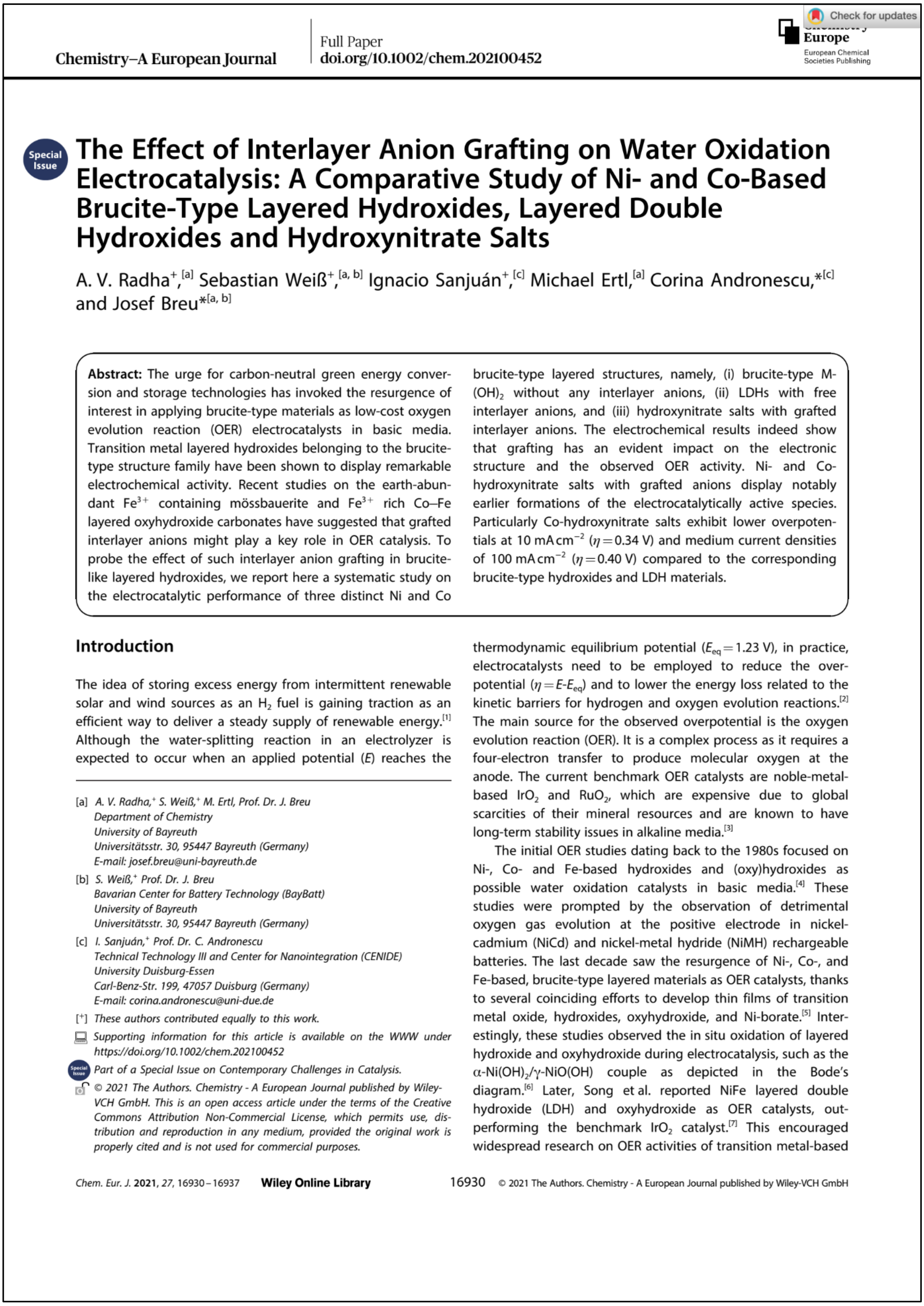

Chemistry–A European Journal | Full Paper
doi.org/10.1002/chem.202100452

The Effect of Interlayer Anion Grafting on Water Oxidation Electrocatalysis: A Comparative Study of Ni- and Co-Based Brucite-Type Layered Hydroxides, Layered Double Hydroxides and Hydroxynitrate Salts

A. V. Radha+,[a] Sebastian Weiß+,[a, b] Ignacio Sanjuán+,[c] Michael Ertl,[a] Corina Andronescu,*[c] and Josef Breu*[a, b]

Abstract: The urge for carbon-neutral green energy conversion and storage technologies has invoked the resurgence of interest in applying brucite-type materials as low-cost oxygen evolution reaction (OER) electrocatalysts in basic media. Transition metal layered hydroxides belonging to the brucite-type structure family have been shown to display remarkable electrochemical activity. Recent studies on the earth-abundant Fe^{3+} containing mössbauerite and Fe^{3+} rich Co–Fe layered oxyhydroxide carbonates have suggested that grafted interlayer anions might play a key role in OER catalysis. To probe the effect of such interlayer anion grafting in brucite-like layered hydroxides, we report here a systematic study on the electrocatalytic performance of three distinct Ni and Co brucite-type layered structures, namely, (i) brucite-type $M(OH)_2$ without any interlayer anions, (ii) LDHs with free interlayer anions, and (iii) hydroxynitrate salts with grafted interlayer anions. The electrochemical results indeed show that grafting has an evident impact on the electronic structure and the observed OER activity. Ni- and Co-hydroxynitrate salts with grafted anions display notably earlier formations of the electrocatalytically active species. Particularly Co-hydroxynitrate salts exhibit lower overpotentials at 10 mA cm^{-2} ($\eta = 0.34$ V) and medium current densities of 100 mA cm^{-2} ($\eta = 0.40$ V) compared to the corresponding brucite-type hydroxides and LDH materials.

Introduction

The idea of storing excess energy from intermittent renewable solar and wind sources as an H_2 fuel is gaining traction as an efficient way to deliver a steady supply of renewable energy.[1] Although the water-splitting reaction in an electrolyzer is expected to occur when an applied potential (E) reaches the thermodynamic equilibrium potential ($E_{eq} = 1.23$ V), in practice, electrocatalysts need to be employed to reduce the overpotential ($\eta = E - E_{eq}$) and to lower the energy loss related to the kinetic barriers for hydrogen and oxygen evolution reactions.[2] The main source for the observed overpotential is the oxygen evolution reaction (OER). It is a complex process as it requires a four-electron transfer to produce molecular oxygen at the anode. The current benchmark OER catalysts are noble-metal-based IrO_2 and RuO_2, which are expensive due to global scarcities of their mineral resources and are known to have long-term stability issues in alkaline media.[3]

The initial OER studies dating back to the 1980s focused on Ni-, Co- and Fe-based hydroxides and (oxy)hydroxides as possible water oxidation catalysts in basic media.[4] These studies were prompted by the observation of detrimental oxygen gas evolution at the positive electrode in nickel-cadmium (NiCd) and nickel-metal hydride (NiMH) rechargeable batteries. The last decade saw the resurgence of Ni-, Co-, and Fe-based, brucite-type layered materials as OER catalysts, thanks to several coinciding efforts to develop thin films of transition metal oxide, hydroxides, oxyhydroxide, and Ni-borate.[5] Interestingly, these studies observed the in situ oxidation of layered hydroxide and oxyhydroxide during electrocatalysis, such as the α-$Ni(OH)_2$/γ-NiO(OH) couple as depicted in the Bode's diagram.[6] Later, Song et al. reported NiFe layered double hydroxide (LDH) and oxyhydroxide as OER catalysts, outperforming the benchmark IrO_2 catalyst.[7] This encouraged widespread research on OER activities of transition metal-based

---

[a] A. V. Radha,+ S. Weiß,+ M. Ertl, Prof. Dr. J. Breu
Department of Chemistry
University of Bayreuth
Universitätsstr. 30, 95447 Bayreuth (Germany)
E-mail: josef.breu@uni-bayreuth.de

[b] S. Weiß,+ Prof. Dr. J. Breu
Bavarian Center for Battery Technology (BayBatt)
University of Bayreuth
Universitätsstr. 30, 95447 Bayreuth (Germany)

[c] I. Sanjuán,+ Prof. Dr. C. Andronescu
Technical Technology III and Center for Nanointegration (CENIDE)
University Duisburg-Essen
Carl-Benz-Str. 199, 47057 Duisburg (Germany)
E-mail: corina.andronescu@uni-due.de

[+] These authors contributed equally to this work.

Supporting information for this article is available on the WWW under https://doi.org/10.1002/chem.202100452

Part of a Special Issue on Contemporary Challenges in Catalysis.

LDHs with various combinations of cations, exfoliated and electrodeposited ultrathin LDH sheets, as well as numerous graphite composites of LDHs.[8]

Recently, our research group introduced two OER active materials, the earth-abundant Fe^{3+} containing mössbauerite,[9] and Fe^{3+} rich Co–Fe layered (oxy)hydroxides.[10] Later, a detailed structural analysis of mössbauerite by combining powder X-ray diffraction fitting with the DFT computed structural models revealed a randomly interstratified disordered structure with the interlayer carbonate partially grafted to the brucite layers.[11] In line with this, previously, Hunter et al.[12] identified some of the interlayer nitrite ions to be directly bound to Fe located at the edge of the brucite-type layer.

To the best of our knowledge, the effect of grafting anions to the brucite-type layers on the electrocatalytic performance has not been studied systematically. For selected transition metal cations such as Co and Ni, brucite-type materials, grafted hydroxy salts, and intercalated LDHs are accessible (Figure 1) and hence allowing for an investigation on the influence of grafting on their electrocatalytic performances.

Results and Discussion

Hydroxides of divalent first-row transition metal cations such as Ni^{2+}, Co^{2+}, Fe^{2+}, Mn^{2+}, Cu^{2+}, and Zn^{2+} with ionic radii in the range of 0.60 to 0.75 Å crystallize in the brucite structure (Figure 1a) with an interlayer distance of 4.6 Å.[13] LDHs of general formula $[M^{2+}_{6-z}M^{3+}_{z}(OH)_{12}]\{CO_3{\cdot}nH_2O\}$ with $z=1.2$ to 2, are formed upon partial replacement of divalent with trivalent cations, which results in positive hydroxide layers that are charge compensated by hydrated interlayer anions (Figure 1b).[14] Partial substitution of hydroxides with grafted anions leads to the third class of brucite-derived compounds known as metal hydroxy salts (Figure 1c) or hydroxide-rich basic salts, $[M(OH)_{2\text{-}y}]\{(A^{n-})_{y/n}\cdot nH_2O\}$ with distinct y values of 0.5, 0.67, and 1 and $A^{n-}=NO_3^{-}$, Cl^{-}, CO_3^{2-} or SO_4^{2-}.[15]

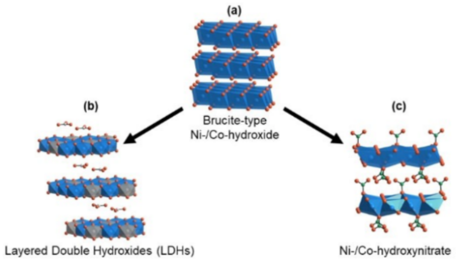

Figure 1. Schematic depiction of brucite-derived transition metal compounds investigated in this work.

Unlike transition metal-based brucite $M(OH)_2$ and LDHs, basic hydroxy salts have received less attention as OER catalysts. For instance, Co-hydroxycarbonate on carbon paper ($\eta=240$ mV at 10 mA cm^{-2})[16] or Ni-foam ($\eta=332$ mV at 10 mA cm^{-2}),[17] and CoMn-hydroxycarbonate on Ni-foam ($\eta=294$ mV at 30 mA cm^{-2})[18] have shown to catalyze OER at low overpotentials. However, these materials were either amorphous or poorly crystalline, with barely visible reflections in their PXRD patterns. The electrocatalytic studies on well-crystalline basic hydroxy salts are mostly limited to CoZn-hydroxy sulfate ($\eta=370$ mV at 10 mA cm^{-2} for $Zn_{2.22}Co_{1.78}SO_4(OH)_6\cdot0.5\,H_2O$) on a glassy carbon electrode.[19] Ni-hydroxynitrate on Ni-foam exhibited the lowest overpotential ($\eta=231$ mV at 50 mA cm^{-2})[20] reported so far for hydroxy salts. Later it has, however, been shown that the Ni-foam itself contributes to the electrocatalytic activity.[21]

The focus of this study is not reducing the overpotential to the minimum value. Instead, we want to gain insights into the effect of grafting on the overpotential by comparing the performance of three distinct Ni and Co brucite-derived layered structures, namely, (i) brucite $M(OH)_2$ without any interlayer anions, (ii) LDHs with free interlayer anions and (iii) hydroxynitrates with grafted interlayer anions.

For brucite structure, commercial reagent grade $Ni(OH)_2$ and $Co(OH)_2$ were used. The LDH structure requires trivalent cations. To avoid synergistic effects reported with Fe^{3+} in electrocatalysis,[22] Al^{3+} is chosen as an electrochemically inert trivalent cation. Both NiAl-CO_3 and CoAl-CO_3 LDHs were obtained by urea hydrolysis. Ni and Co are known to exist as hydroxynitrate.[23] Here, nitrate bonds or grafts directly to the metal cation, replacing hydroxide in the brucite layers (Figure 1c), leading to an interlayer distance of 6.9 Å, which is intermediate between brucite-type hydroxides (Figure 1a) and LDHs (Figure 1b).[15]

Synthesis and Characterization of Compounds

The compositions of hydroxide samples, LDHs, and hydroxynitrates were determined by elemental analyses and were found to be within the expected range (Table 1). All X-ray powder diffraction traces could be fully indexed, indicating phase pure

Table 1. Summary of compositions and the cell parameters of Ni- and Co-based phases.

Sample	Composition	*a* (Å)	*c* (Å)	Polytype
$Ni(OH)_2$	$Ni(OH)_2$	3.127(5)	4.613(1)	1*H*
NiAl-CO_3 LDH	$Ni_{4.04}Al_{1.96}(OH)_{12}(CO_3)_{0.98}\cdot2.5\,H_2O$	3.027(1)	22.57(1)	$3R_1$
Ni-hydroxy-nitrate	$Ni(OH)_{1.5}(NO_3)_{0.5}\cdot0.12\,H_2O$	3.131(3)	6.869(1)	1*H*
$Co(OH)_2$	$Co(OH)_2$	3.183(0)	4.657(2)	1*H*
CoAl-CO_3-LDH	$Co_{4.07}Al_{1.93}(OH)_{12}(CO_3)_{0.97}\cdot3.2\,H_2O$	3.077(7)	22.83(2)	$3R_1$
Co-hydroxy-nitrate	$Co(OH)_{1.54}(NO_3)_{0.46}\cdot0.05\,H_2O$	3.188(9)	20.79(8)	$3R_2$

materials (Figures 2). The PXRD patterns of $Ni(OH)_2$ and $Co(OH)_2$ conform to a typical brucite structure (Figures 2a and d) with P-3m1 space group and refined cell parameters in close agreement with reported literature values (PDF: 14-117 (4.6 Å) and PDF: 30-443 (4.7 Å) for Ni $(OH)_2$ and $Co(OH)_2$, respectively; Table 1).

The PXRD patterns of NiAl-CO_3 and CoAl-CO_3 LDHs (Figure 2b and e) could be indexed with a three-layer rhombohedral cell with R-3m space group with interlayer distances of 7.52(3) Å and 7.61(0) Å for NiAl-CO_3 and CoAl-CO_3 LDHs, respectively, which is in perfect agreement with published values for carbonate intercalated LDHs (for instance 7.5 Å for NiAl-CO_3 (PDF: 015-0087)). In line with earlier studies, the presence of prominent mid-2θ reflections around 2.6 Å, 2.3 Å, and 1.9 Å in these PXRD patterns match with (012), (015), and (018) reflections supporting the $3R_1$ polytype structure having a stacking sequence of *AC CB BA AC*.[24]

As expected, for hydroxynitrates (Figure 2c and f), interlayer distances of 6.9 Å (Co-hydroxynitrate) and 7.0 Å (Ni-hydroxynitrate) were found to be intermediate between the values of the hydroxide and the LDH counterparts. This confirmed the presence of grafted nitrate anions. A nice integral series of (00l) reflections indicates a uniform interlayer distance with grafted anions being present in all interlayers. For both the Co- and Ni-hydroxynitrate salts (Figure 2c and f), (hkl) reflections with $l \neq 0$ indicated ordered polytypes. For Ni-hydroxynitrate, the reflections observed at d-values of 6.9 Å, 3.5 Å, 2.7 Å, 2.5 Å, 2.1 Å, 1.7 Å, 1.6 Å, and 1.5 Å correspond to (001), (002), (100), (101), (102), (103), (110), and (111) reflections of the 1H polytype as shown in earlier reported data (PDF: 022-0752).[25] The non-systematic broadening of mid-2θ reflections between 30° to 50° (FWHM varying from 0.5° to 0.8° compared to 0.3° of basal ones), however, indicated a certain degree of stacking faults. As previously reported and contrary to Ni-hydroxynitrate, Co-hydroxynitrate crystallizes in the $3R_2$ polytype with an *AC BA CB A* stacking sequence.[26] The positions of the prominent mid-2θ reflections in Co-hydroxynitrate (Figure 2f) at 2.7 Å, 2.4 Å, and 2.0 Å are consistent with this earlier polytype assignment and correspond to (101), (104), and (107) reflections. Again, the non-systematic broadening of mid-2θ reflections (FWHM varying from 0.1° to 0.3° compared to 0.1° of basal ones) is due to the presence of stacking faults similar to its Ni analogue.

FTIR spectra of both, $Ni(OH)_2$ (Figure 3a) and $Co(OH)_2$ (Figure 3d), showed three absorptions bands in two different regions as typical for brucite structures: A sharp peak due to non-hydrogen bonded hydroxide groups around 3630 cm^{-1}, and two overlapping M–O vibration mode at ≈500 cm^{-1}.

FTIR spectra of NiAl-CO_3 (Figure 3b) and CoAl-CO_3 LDHs (Figure 3e) displayed peaks in three different regions due to the presence of interlayer anions and interlayer water molecules in addition to structural hydroxyl anions. The hydroxide stretching modes in LDHs appear to be broad and shifted to a lower region around ≈3400 cm^{-1} due to hydrogen bonding with the interlayer water molecules. The corresponding bending mode showed up as a weak signal at 1600 cm^{-1}.[27] A large mass difference between the transition metal Ni/Co and Al cations split the M–O–H bending modes into a doublet at 560 and 615 cm^{-1}. Additional peaks like a strong v_3 band at 1350 cm^{-1}

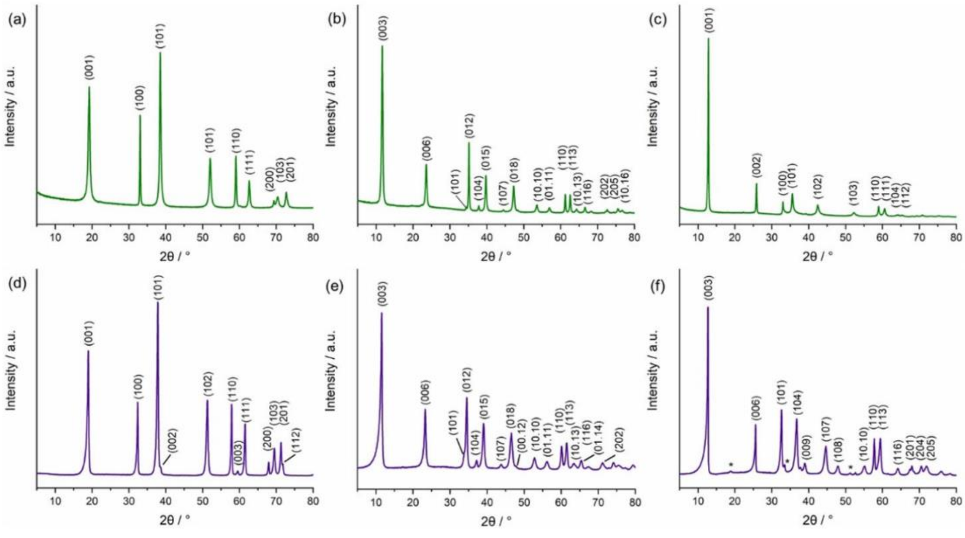

Figure 2. PXRD patterns of Ni-compounds (top): (a) $Ni(OH)_2$ without interlayer anions, (b) NiAl-CO_3 LDH, and (c) Ni-hydroxynitrate with grafted nitrate anion. PXRD patterns of Co-compounds (bottom): (d) $Co(OH)_2$ without interlayer anions, (e) CoAl-CO_3 LDH, and (f) Co-hydroxynitrate with grafted nitrate anion. A minor $Co(OH)_2$ impurity in (f) is marked with an asterisk.

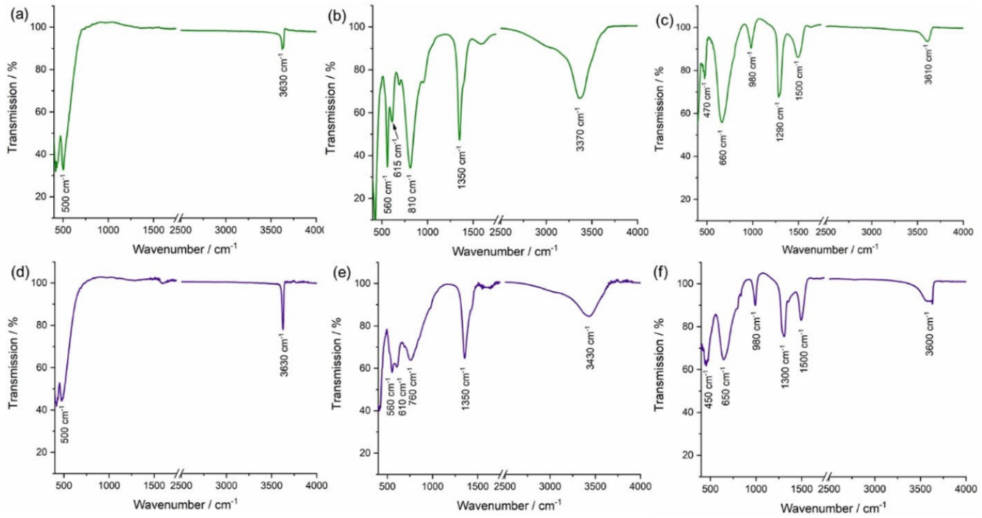

Figure 3. FTIR spectra of Ni-compounds (top): (a) $Ni(OH)_2$ without interlayer anions, (b) $NiAl-CO_3$ LDH, and (c) Ni-hydroxynitrate with grafted nitrate anion. FTIR spectra of Co-compounds (bottom): (d) $Co(OH)_2$ without interlayer anions, (e) $CoAl-CO_3$ LDH, and (f) Co-hydroxynitrate with grafted nitrate anion.

along with two weak signals due to v_2 and v_4 modes around 810 and 667 cm^{-1} that overlap with the M–O lattice vibrations modes confirmed the presence of intercalated carbonate anion in D_{3h} symmetry in both LDHs.

The FTIR spectra of Ni- (Figure 3c) and Co-hydroxynitrate (Figure 3f) were distinctly different from the LDH spectra regarding both wavenumbers and the splitting of the bands. For instance, the band due to the hydrogen-bonded hydroxide group appeared as a broad peak around 3600 cm^{-1} and M–O–OH and M–O lattice vibration modes at ca. 650 and ca. 450 cm$^{-1,}$ respectively. A strikingly distinct part was the presence of three strong absorption bands at 1300 cm^{-1}, 1500 cm^{-1}, and 980 cm^{-1}, which could be assigned to v_1, v_4, and v_3, vibration modes of the nitrate anion with symmetry lowered to C_{2v}. The presence of two distinct v_1 and v_4 modes with a wavenumber difference of 200 cm^{-1} indicated that one oxygen of nitrate is directly bound to the metal cation completing its octahedral coordination shell. This provides direct experimental evidence for the nitrate grafting in both Ni- and Co-hydroxynitrate.

As evidenced by the SEM micrographs (Figure 4), all compounds tend to form larger, intergrown aggregates of platy crystals as expected for layered structures. The corresponding BET surface areas are depicted in the micrographs and give a first hint regarding the accessible surface, solely based on morphological considerations. For Ni-based compounds, the $NiAl-CO_3$ LDH and $Ni(OH)_2$ feature the highest and the lowest surface area, respectively. Similarly, the $CoAl-CO_3$ LDH resembles the compound with the highest BET surface area, while the Co-hydroxynitrate features the lowest. Based on these structural considerations alone, the samples with the lowest accessible surface area are expected to perform the least active in OER catalysis.

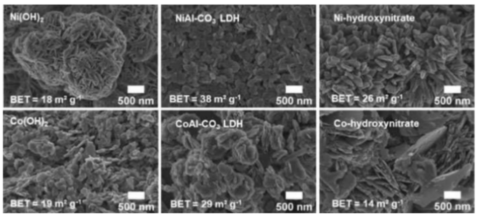

Figure 4. SEM micrographs of Ni- (top) and Co- (bottom) compounds: $Ni(OH)_2$ and $Co(OH)_2$ without interlayer anions (left), $NiAl-CO_3$ LDH and $CoAl-CO_3$ LDH (middle), and Ni-/Co-hydroxynitrate with grafted nitrate anion (right) with corresponding BET values.

However, as the active site for OER has been proposed to be located at the edges of the brucite layers rather than the planes, activity is expected to increase with the surface area and the contribution of the edges to it.[28] Thus, platelets with small diameters and small aspect ratio (diameter/thickness) should be most advantageous. To determine the accessibility based on the electrochemically active surface area, double layer capacitance measurements are performed complementary to the electrocatalytic measurements in the following section.

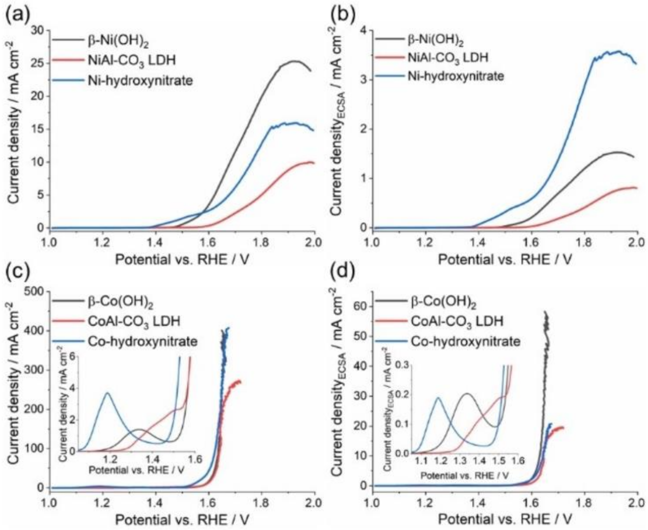

Figure 5. Linear sweep voltammograms of the Ni- (a and b) and Co-based compounds (c and d). LSVs were recorded with a scan rate of 5 mV s^{-1}, and RDE speed of 1600 rpm in O_2 saturated purified 1 M KOH solutions. In plots (a) and (c), the current density is calculated using the geometric area of the electrode. In contrast, in plots (b) and (d), the current density is calculated using the ECSA.

Table 2. Summary of the ECSA and the overpotential (V) required to record 10 and 100 mA cm^{-2} of Ni- and Co-based layered hydroxides (overpotentials for geometric area normalized 10 mA cm^{-2} and 10 mA cm^{-2} ECSA normalization).

Sample	ECSA (cm^2)	Overpotential η (V) 10 mA cm^{-2}	Overpotential η (V) 10 mA cm^{-2} (ECSA)	Overpotential η (V) 100 mA cm^{-2}
$Ni(OH)_2$	1.88 ± 0.09	0.49 ± 0.03	–	–
NiAl-CO_3-LDH	1.39 ± 0.17	–	–	–
Ni-hydroxy-nitrate	0.51 ± 0.01	0.56 ± 0.03	-	-
$Co(OH)_2$	0.80 ± 0.02	0.358 ± 0.003	0.40 ± 0.01	0.414 ± 0.009
CoAl-CO_3-LDH	1.57 ± 0.03	0.366 ± 0.005	0.415 ± 0.001	0.416 ± 0.003
Co-hydroxy-nitrate	2.22 ± 0.10	0.34 ± 0.02	0.415 ± 0.002	0.401 ± 0.005

OER electrocatalysis of Ni and Co compounds

The OER electrocatalytic performance of the different brucite-type layered materials was analyzed using linear sweep voltammograms recorded in the OER potential window (Figure 5). The normalization of the recorded currents was done using both geometric area of the catalyst film, as well as its ECSA evaluated from the cyclic voltammograms recorded in the non-Faradaic region using different scan rates (Table 2). When normalized to the geometric area, significantly higher activity is observed for Co-based compounds, for which current densities up to hundreds of mA cm^{-2} are recorded with ~400 mV overpotential. At the same time, in the same potential window, just a few tenths of mA cm^{-2} are generated for the Ni-based materials (Figure 5, Table 2). This fact suggests the superior activity of Co-based compounds towards OER and is in line with the proposed activity trend for different transition-metal (oxy) hydroxides in alkaline media.[29]

In the LSVs recorded using the Ni-based compounds (Figure 5a and b), different features are observed associated with the Ni^{2+} oxidation. In the case of β-$Ni(OH)_2$ and Ni-hydroxynitrate, the Ni^{2+} electro-oxidation to Ni^{3+} was observed as a pre-oxidation shoulder which appeared at potentials below OER. In the case of Ni-hydroxynitrate, Ni^{2+} electro-oxidation occurred at more cathodic potentials (~1.4 V vs. RHE) than in the case of β-$Ni(OH)_2$ (~1.45 V vs. RHE), while for NiAl-CO_3 LDH, no clear Ni^{2+} oxidation peak could be observed. This indicates that the grafted nitrate anions influence the oxidation of Ni^{2+}, allowing its conversion to the active Ni^{3+} OER electrocatalyst at more cathodic potentials already. Different activity trends were observed depending on the area used to normalize the recorded currents, the geometric or the ECSA one. While the normalization by the geometric area indicates β-$Ni(OH)_2$ as the most active, the normalization to the ECSA concludes that Ni-hydroxynitrate shows the highest catalytic activity of Ni-based electrocatalysts. Based on these findings, we conclude that electrocatalytic centers in Ni-hydroxynitrate are the most active. Still, the overall performance suffers from the lower number of active sites accessible due to its morphology. The rotating ring disk electrode (RRDE) technique was used to confirm the O_2 formation on the Co- and Ni hydroxynitrates (Figure S1). The faradaic efficiencies (FE) of O_2 obtained using Ni-hydroxynitrate at +1.5 V vs. RHE was 91±9% indicating that the recorded currents correspond mainly to the OER.

As observed for the Ni-hydroxynitrate, and also in the case of Co-hydroxynitrate, an oxidation peak associated with Co^{2+} oxidation[30] was present at ~1.2 V. In comparison, for β-$Co(OH)_2$ and CoAl-CO_3 LDH, an oxidation process was observed at more anodic potentials with ~1.35 V and 1.4 V vs. RHE, respectively. This suggests that the presence of grafted nitrate anions is influencing the formation of the Co^{3+} species. Different activity trends were also observed for the Co-based compounds when comparing the potentials at which a current density of 10 mA cm^{-2} was obtained, depending on the considered area. When the geometric area is used, Co-hydroxynitrate shows the highest activity reaching 10 mA cm^{-2} at 0.34 V overpotential while β-$Co(OH)_2$ requires 0.36 V. At a higher current density of 100 mA cm^{-2}, the Co-hydroxynitrate still allows for a lower overpotential than the other materials under investigation. With an overpotential of 0.4 V, it performs better than the β-$Co(OH)_2$ (0.41 V) and the CoAl-CO_3 LDH (0.42 V). When the ECSA is considered, the Co-hydroxynitrate initially shows the earliest onset of OER. However, at a current density of 10 mA cm^{-2} the recorded overpotential for β-$Co(OH)_2$ is 0.4 V while 10 mV more are needed for Co-hydroxynitrate and CoAl-CO_3 LDH. These differences are not as pronounced as in Ni-based materials, indicating that in the case of Co-based materials, nitrate grafting influences the oxidation of Co^{2+}. Still, overall the OER electrocatalytic activity is not so strongly affected as in Ni-based compounds. Since higher current densities are recorded on Co hydroxynitrate compared with the Ni one, to quantify the formed O_2 we used a gas chromatograph coupled to a gas-tight electrochemical cell. In this case, the Co-hydroxynitrate catalyst was deposited on carbon paper, and the electrolysis was performed in galvanostatic mode. We started by applying 15 mA (3.75 mA cm^{-2}), and we increased the current up to 200 mA (50 mA cm^{-2}). The produced O_2 was quantified by gas chromatography, and FE values in the range 91-103 were calculated (Figure S3). For example, at 50 mA cm^{-2}, the calculated FE is 95±1%.

In general, the performance of electrocatalysts must be interpreted in terms of oxidation state, electronic structure, and coordination state of the active metal sites.[8b] *In-situ* studies of layered electrocatalysts have recognized the transition metal positions located at the edges and corners of the layers as more active OER sites.[31] Here, synergistic effects based on metal cations in the second coordination sphere are regarded negligible as the catalytic activity of CoAl-CO_3 LDH ($\eta = 366$ mV at 10 mA cm^{-2}) is comparable to NiCo-CO_3 and CoCo-CO_3 LDHs with overpotentials of 385 and 395 mV at 10 mA cm^{-2}.[7] Thus, we assume that the effect of electrochemically inactive, structural Al can indeed be neglected.

Ni-hydroxynitrate showed the earliest formation of electrocatalytically active Ni^{3+} from all Ni-based compounds. Similarly, among all Co-based samples studied, Co-hydroxynitrate additionally featured the highest OER activity up to 407 mA cm^{-2}. This would indicate that the grafted anion of hydroxy salts triggers a larger separation of individual layers than the hydroxide compounds. Thus, it improves the accessibility of electrochemically active cation sites for OER catalysis at the edges, facilitating the OER reaction. Furthermore, the electronic structure and thus redox activity is modulated by the formal replacement of hydroxide by nitrate anions. According to the spectrochemical row,[32] the electron-donating capability of hydroxide ions is expected to be higher than those of the nitrate-ions. Thus, a lower electron density is expected at the electrocatalytically active transition-metal centers for hydroxy salts compared to hydroxide or LDH compounds. Previous investigations on NiFe-LDHs have shown that charge delocalization and reduced electron density created by incorporating electron-withdrawing anions or cations can facilitate higher-valent electrophilic transition metal ion sites. These can promote the nucleophilic attack of hydroxyl and water molecules and thus improve the adsorption of the reaction intermediate during OER.[33]

To further understand the potential of hydroxynitrates as OER electrocatalysts, their stability was evaluated by current-controlled electrolysis (Figure 6a). A constant current corresponding to 10 mA cm^{-2} current density was applied for 2 h while continuously monitoring the potential. While Ni-hydroxynitrate shows an initial deactivation, followed by activation with time, a constant potential is recorded when using Co-hydroxynitrate (Figure 6b), indicating superior stability of the latter with time at these moderate electrolysis conditions. For the Co-hydroxynitrate catalyst, we analyzed every 15 minutes the concentration of the formed O_2 during the 2 h electrolysis. The calculated FEs indicate a stable electrolysis process in which O_2 is produced with FE close to 100% without significant variations over the course of the 2 h (Figure S4).

LSVs recorded for both materials before and after the stability test support the previous observation. While for Ni-hydroxynitrate, higher current densities are recorded after the prolonged electrolysis (Figure S7), in the case of Co-hydroxynitrate, a slight decay of the activity is observed, probably due to

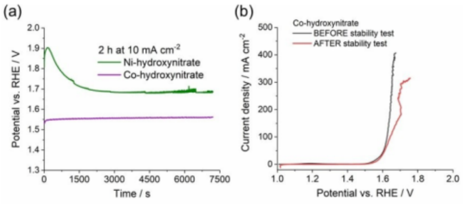

Figure 6. (a) Chronopotentiometric measurements performed in 1 M KOH at a current density corresponding to 10 mA cm^{-2} for 2 h under 1600 rpm, using Co- and Ni-hydroxynitrate modified GC electrodes; (b) LSVs recorded for the Co-hydroxynitrate modified GC before and after the stability test.

decreased conductivity of the Co-hydroxynitrate as it can be observed from the LSV slope. Still, the Co-hydroxynitrate shows higher electrocatalytic activity compared with the Ni one. No significant changes can be noticed on the electrocatalysts film based on the SEM pictures taken before and after the stability measurement.

Post-electrolysis XRD analysis was performed for both the Ni-hydroxynitrate (Figure S8) and the Co-hydroxynitrate (Figure S9). Both XRD patterns show the presence of the initial catalyst with some side phases formed during the 2 h electrolysis. However, an unaltered basal spacing of the layered structures indicates that the interlayer space composition has not changed over the course of the experiment. For Ni-hydroxynitrate, some of the additional reflections can be assigned to the presence of $K_2Ni(CO_3)_2$ (PDF: 00-046-0783), K_2CO_3 (PDF: 00-011-0655), and NiO (PDF: 00-047-1049). Previous studies of this catalyst have also shown the alteration of the surface layer upon prolonged electrolysis.[34] The newly formed phases can contribute to the fluctuations observed in the chronopotentiometric measurements. Besides this, possible catalyst dissolution occurring during the electrolysis process can change the catalyst film conductivity and generate a catalyst film with an overall higher electrocatalytic activity. In Co-hydroxynitrate, evidence for the presence of Co_3O_4 (PDF: 00-042-1467) and K_2CoO_2 (PDF: 00-049-1556) can be found. Post-electrolysis EDX measurements for Ni- and Co-hydroxynitrate indicate no detectable incorporation of secondary metal ions from the electrolyte (Figure S10, S11). Despite the fact that secondary phases formed during the 2 h electrolysis, no significant impact can be noticed in the overall performance of the Co-hydroxynitrate coated electrode.

Conclusion

Grafting of anions to brucite-type layered structures formally represents a substitution of hydroxides, for example, by nitrate. On the one hand, adjacent layers are separated to larger distances allowing for easier access to active sites at the edges. On the other hand, the nitrate ligand's basicity is smaller than the hydroxide ligand, and the electron density at the metal center is reduced. Both factors may contribute to the observed increased OER efficiency of hydroxy salts than simple hydroxides or LDH structures. While hydroxy salts are less flexible with respect to compositional variations than LDHs, doping, for instance, with Fe, will be feasible to some extent. During 2 h electrolysis performed at 10 mA cm^{-2}, both Co and Ni-hydroxynitrates form secondary phases, as often observed for transition metal-based OER electrocatalysts. Hydroxy salts show high versatility, being accessible for various anions like acetate, sulfate, carbonate, perchlorates, and halides. Based on previous experience with NiFe-LDHs, further performance improvement should be achievable this way. Hydroxy salts certainly deserve further attention in the electrocatalysis world.

Acknowledgements

The authors are grateful for financial support by the Deutsche Forschungsgemeinschaft (DFG) in the framework of the SFB 840. We thank Prof. Mirijam Zobel for the measurement time with her powder X-ray diffractometer as well as Anna-Maria Dietel for CHN analysis of the samples. We thank Lena Geiling and Marco Schwarzmann for SEM measurements and BayCEER for ICP-OES measurements. We thank Renee Timmins for English proofreading. S.W. acknowledges the support from the Elite Network of Bavaria and thanks the graduate school of the Bavarian Center for Battery Technology (BayBatt) for ongoing support. C.A. acknowledges the financial support by DFG if the framework of the CRC 247. Open access funding enabled and organized by Projekt DEAL.

Conflict of Interest

The authors declare no conflict of interest.

Keywords: electrochemistry · nickel/cobalt hydroxynitrate · nitrate grafting · oxygen evolution reaction · water splitting

[1] a) H. L. Tuller, *Mater. Renew. Sustain. Energy* **2017**, *6*, 3; b) Z. Yan, J. L. Hitt, J. A. Turner, T. E. Mallouk, *Proc. Natl. Acad. Sci. USA* **2020**, *117*, 12558–12563.

[2] R. L. Doyle, M. E. G. Lyons, *Photoelectrochemical Solar Fuel Production: From Basic Principles to Advanced Devices* (Eds.: S. Giménez, J. Bisquert), Springer International Publishing, Cham, **2016**, pp. 41–104.

[3] a) S. Trasatti, *J. Electroanal. Chem.* **1980**, *111*, 125–131; b) Y. Lee, J. Suntivich, K. J. May, E. E. Perry, Y. Shao-Horn, *J. Phys. Chem. Lett.* **2012**, *3*, 399–404.

[4] a) D. E. Hall, *J. Electrochem. Soc.* **1983**, *130*, 317; b) M. R. Gennero de Chialvo, A. C. Chialvo, *Electrochim. Acta* **1988**, *33*, 825–830; c) D. A. Corrigan, *J. Electrochem. Soc.* **1987**, *134*, 377.

[5] a) L. Trotochaud, J. K. Ranney, K. N. Williams, S. W. Boettcher, *J. Am. Chem. Soc.* **2012**, *134*, 17253–17261; b) D. K. Bediako, B. Lassalle-Kaiser, Y. Surendranath, J. Yano, V. K. Yachandra, D. G. Nocera, *J. Am. Chem. Soc.* **2012**, *134*, 6801–6809; c) R. L. Doyle, I. J. Godwin, M. P. Brandon, M. E. G. Lyons, *Phys. Chem. Chem. Phys.* **2013**, *15*, 13737–13783.

[6] H. Bode, K. Dehmelt, J. Witte, *Electrochim. Acta* **1966**, *11*, 1079–1087.

[7] F. Song, X. Hu, *Nat. Commun.* **2014**, *5*, 4477.

[8] a) N.-T. Suen, S.-F. Hung, Q. Quan, N. Zhang, Y.-J. Xu, H. M. Chen, *Chem. Soc. Rev.* **2017**, *46*, 337–365; b) Y. Wang, D. Yan, S. El Hankari, Y. Zou, S. Wang, *Adv. Sci.* **2018**, *5*, 1800064.

[9] M. Ertl, C. Andronescu, J. Moir, M. Zobel, F. E. Wagner, S. Barwe, G. Ozin, W. Schuhmann, J. Breu, *Chem. Eur. J.* **2018**, *24*, 9004–9008.

[10] S. Weiß, M. Ertl, S. D. Varhade, A. V. Radha, W. Schuhmann, J. Breu, C. Andronescu, *Electrochim. Acta* **2020**, *350*, 136256.

[11] P. Lyu, M. Ertl, C. J. Heard, L. Grajciar, A. V. Radha, T. Martin, J. Breu, P. Nachtigall, *J. Phys. Chem. C* **2019**, *123*, 25157–25165.

[12] B. M. Hunter, W. Hieringer, J. R. Winkler, H. B. Gray, A. M. Müller, *Energy Environ. Sci.* **2016**, *9*, 1734–1743.

[13] H. R. Oswald, R. Asper, *Preparation and Crystal Growth of Materials with Layered Structures* (Ed.: R. M. A. Lieth), Springer Netherlands, Dordrecht, **1977**, pp. 71–140.

[14] H. F. W. Taylor, *Mineral. Mag.* **1973**, *39*, 377–389.

[15] a) M. Rajamathi, G. S. Thomas, P. V. Kamath, *J. Chem. Sci.* **2001**, *113*, 671–680; b) S. P. Newman, W. Jones, *J. Solid State Chem.* **1999**, *148*, 26–40.

[16] S. Zhang, B. Ni, H. Li, H. Lin, H. Zhu, H. Wang, X. Wang, *Chem. Commun.* **2017**, *53*, 8010–8013.

[17] M. Xie, L. Yang, Y. Ji, Z. Wang, X. Ren, Z. Liu, A. M. Asiri, X. Xiong, X. Sun, *Nanoscale* **2017**, *9*, 16612–16615.

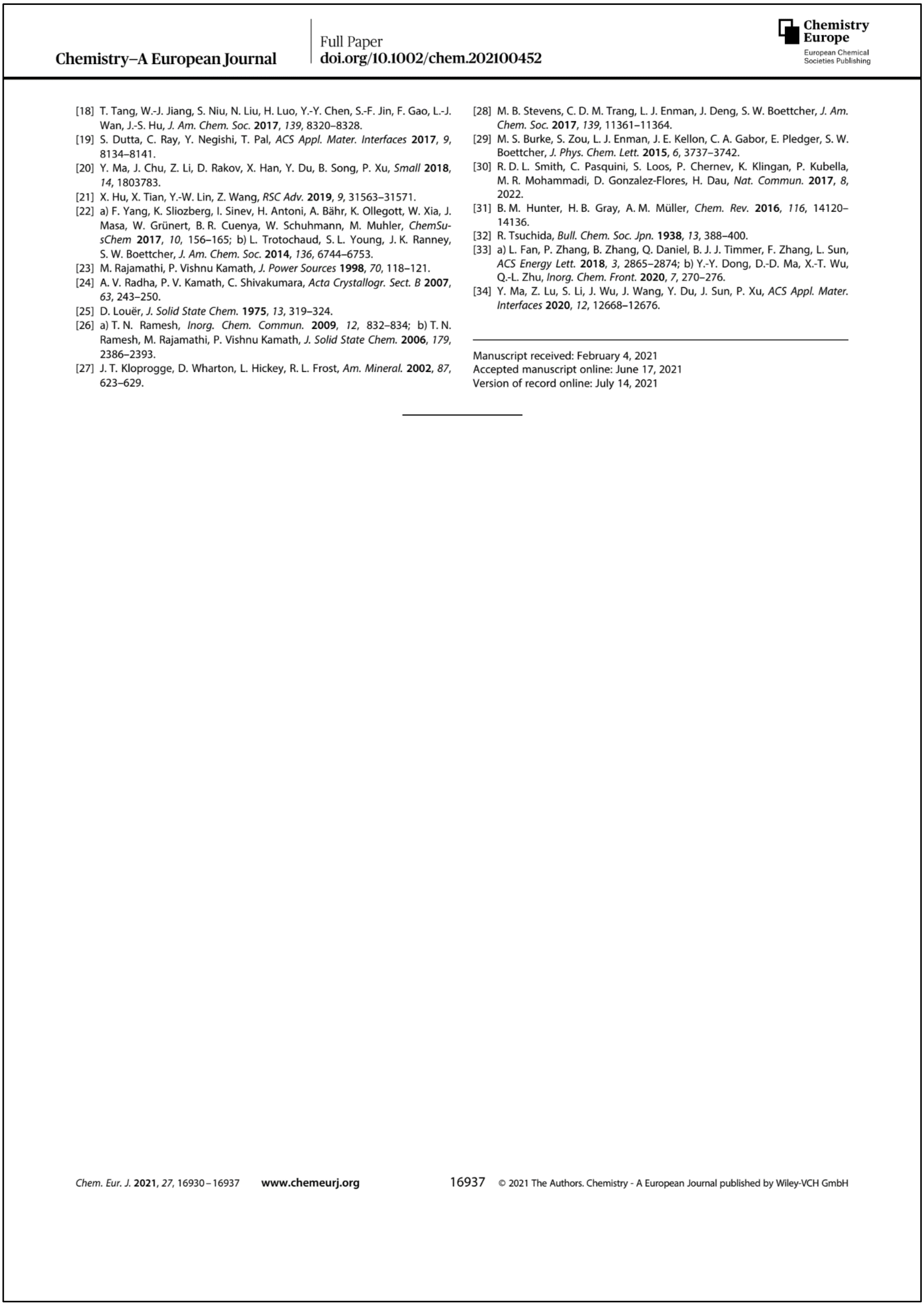

Chemistry–A European Journal
Full Paper
doi.org/10.1002/chem.202100452
Chemistry Europe
European Chemical Societies Publishing

[18] T. Tang, W.-J. Jiang, S. Niu, N. Liu, H. Luo, Y.-Y. Chen, S.-F. Jin, F. Gao, L.-J. Wan, J.-S. Hu, *J. Am. Chem. Soc.* **2017**, *139*, 8320–8328.
[19] S. Dutta, C. Ray, Y. Negishi, T. Pal, *ACS Appl. Mater. Interfaces* **2017**, *9*, 8134–8141.
[20] Y. Ma, J. Chu, Z. Li, D. Rakov, X. Han, Y. Du, B. Song, P. Xu, *Small* **2018**, *14*, 1803783.
[21] X. Hu, X. Tian, Y.-W. Lin, Z. Wang, *RSC Adv.* **2019**, *9*, 31563–31571.
[22] a) F. Yang, K. Sliozberg, I. Sinev, H. Antoni, A. Bähr, K. Ollegott, W. Xia, J. Masa, W. Grünert, B. R. Cuenya, W. Schuhmann, M. Muhler, *ChemSusChem* **2017**, *10*, 156–165; b) L. Trotochaud, S. L. Young, J. K. Ranney, S. W. Boettcher, *J. Am. Chem. Soc.* **2014**, *136*, 6744–6753.
[23] M. Rajamathi, P. Vishnu Kamath, *J. Power Sources* **1998**, *70*, 118–121.
[24] A. V. Radha, P. V. Kamath, C. Shivakumara, *Acta Crystallogr. Sect. B* **2007**, *63*, 243–250.
[25] D. Louër, *J. Solid State Chem.* **1975**, *13*, 319–324.
[26] a) T. N. Ramesh, *Inorg. Chem. Commun.* **2009**, *12*, 832–834; b) T. N. Ramesh, M. Rajamathi, P. Vishnu Kamath, *J. Solid State Chem.* **2006**, *179*, 2386–2393.
[27] J. T. Kloprogge, D. Wharton, L. Hickey, R. L. Frost, *Am. Mineral.* **2002**, *87*, 623–629.
[28] M. B. Stevens, C. D. M. Trang, L. J. Enman, J. Deng, S. W. Boettcher, *J. Am. Chem. Soc.* **2017**, *139*, 11361–11364.
[29] M. S. Burke, S. Zou, L. J. Enman, J. E. Kellon, C. A. Gabor, E. Pledger, S. W. Boettcher, *J. Phys. Chem. Lett.* **2015**, *6*, 3737–3742.
[30] R. D. L. Smith, C. Pasquini, S. Loos, P. Chernev, K. Klingan, P. Kubella, M. R. Mohammadi, D. Gonzalez-Flores, H. Dau, *Nat. Commun.* **2017**, *8*, 2022.
[31] B. M. Hunter, H. B. Gray, A. M. Müller, *Chem. Rev.* **2016**, *116*, 14120–14136.
[32] R. Tsuchida, *Bull. Chem. Soc. Jpn.* **1938**, *13*, 388–400.
[33] a) L. Fan, P. Zhang, B. Zhang, Q. Daniel, B. J. J. Timmer, F. Zhang, L. Sun, *ACS Energy Lett.* **2018**, *3*, 2865–2874; b) Y.-Y. Dong, D.-D. Ma, X.-T. Wu, Q.-L. Zhu, *Inorg. Chem. Front.* **2020**, *7*, 270–276.
[34] Y. Ma, Z. Lu, S. Li, J. Wu, J. Wang, Y. Du, J. Sun, P. Xu, *ACS Appl. Mater. Interfaces* **2020**, *12*, 12668–12676.

Manuscript received: February 4, 2021
Accepted manuscript online: June 17, 2021
Version of record online: July 14, 2021

Chemistry–A European Journal

Supporting Information

The Effect of Interlayer Anion Grafting on Water Oxidation Electrocatalysis: A Comparative Study of Ni- and Co-Based Brucite-Type Layered Hydroxides, Layered Double Hydroxides and Hydroxynitrate Salts

A. V. Radha[+], Sebastian Weiß[+], Ignacio Sanjuán[+], Michael Ertl, Corina Andronescu,* and
Josef Breu*

Experimental Section

All starting materials $Ni(NO_3)_2 \cdot 6H_2O$, $Co(NO_3)_2 \cdot 6H_2O$, $Al(NO_3)_3 \cdot 6H_2O$, and urea reagents, as well as Chelex resin, $K_3[Fe(CN)_6]$ and 5 wt.% Nafion dispersion in a mixture 45 % water and 55 % aliphatic alcohols were purchased from Sigma-Aldrich or Merck (India) and used as such. KOH (reagent grade, 85.9 %) and ethanol absolute (reagent grade 99.97%) were purchased from VWR chemicals. All solutions were prepared using Milli-Q water, with a resistivity below 18.2 MΩ cm.

Material preparations

Metal hydroxides: Reagent grade $Ni(OH)_2$ and $Co(OH)_2$ procured from Sigma-Aldrich were used as control samples without further treatment.

LDH synthesis: Both, NiAl-CO_3, and CoAl-CO_3 LDHs with interlayer carbonate were synthesized by making use of the urea hydrolysis method.[1] In a typical synthesis, 0.5 M mixed metal nitrate solution with M^{2+}:M^{3+} ratio as 2:1 was prepared by mixing suitable amounts of divalent and trivalent salts. Then solid urea was dissolved in 40 mL of this mixed metal nitrate solution by maintaining a urea/total metal ratio of 3.3 to 5. Finally, this clear solution was transferred to a Teflon lined stainless steel autoclave and hydrothermally treated at 110 or 180 °C for 24 hours. Then the autoclave was cooled before filtration, the solid was washed with water a couple of times and finally dried in an air oven at 60 °C for 24 hours.

Hydroxynitrate synthesis: Ni- and Co-hydroxynitrate were synthesized using previously reported urea hydrolysis of metal salt melts.[1-2] A slurry was prepared by mixing 18 g of nickel nitrate or cobalt nitrate, 2 g urea and 2 mL of water in a round bottom flask. This slurry was heated at 140 to 160 °C by placing the flask on a heating mantle for 2 to 3 hours until all water evaporated completely leaving behind a solid green (for Ni sample) or a pink cake (for Co sample) at the bottom. Finally, the solid cake/paste was recovered using Milli-Q water after cooling, washed with Milli-Q water 5 times by centrifugation and finally freeze-dried overnight.

Material characterization

Powder X-ray Diffraction (PXRD) traces for Ni-compounds were measured in transmission mode on a STOE STADI P powder diffractometer with a Cu $K_{\alpha 1}$ radiation source ($\lambda = 1.540598$ Å) with a Ge monochromator and a linear position-sensitive detector. To circumvent heavy fluorescence, PXRD patterns of Co-samples were collected using a STOE STADI-P diffractometer with Ag $K_{\alpha 1}$ radiation source ($\lambda = 0.5594075$ Å) in transmission geometry equipped with four MYTHEN2 R 1K detectors. The data collection was done in stationary mode for one hour with samples loaded in 0.5 mm glass capillaries. To assist comparability, the diffraction traces shown in Figure 2 were, however, recalculated assuming Cu $K_{\alpha1}$ radiation. The solid-state infrared (IR) spectra of samples were collected using a JASCO FTIR 6100 spectrometer (range 400-4000 cm^{-1}; resolution 4 cm^{-1}). The specific surface area was measured with a Quantochrome Nova A with N_2 as adsorbate at 77 K applying the Brunauer-Emmet-Teller (BET) method. The Scanning Electron Microscopy (SEM) micrographs were acquired using a Zeiss Ultra Plus. Post-mortem EDX measurements were acquired using the same device equipped with a UltraDry-EDX-Detector (Thermo Fisher Scientific NS7) unit.

Sample compositions: The metal (Ni, Co and Al) contents were determined using a Varian, Vista-Pro Radial Inductively Coupled Plasma Optical Emission Spectrometer (ICP-OES). All solutions were prepared by two-fold dilution to reduce the original metal concertation to the ICP-OES detection range of 1 to 10 mg L^{1} using 5 % HCl (high purity spectroscopic grade). The nitrate and carbonate anions were estimated based on N and C contents determined by CHN analyses using an Elementar Vario EL III equipment. The water contents in samples were calculated from the first step weight loss observed in the thermogravimetric analysis (TGA) curves obtained by heating samples in a platinum crucible under Ar from 25 to 800 °C using a Netzsch STA 449c system (heating rate = 10 K min^{-1}).

Electrochemical measurements

Working electrode preparation: Disk-shaped glassy carbon (GC) electrodes having a geometric area of 0.1134 cm^2 mounted in a Teflon sheath were used as the current collectors. To ensure a reproducible mirror-like surface in all the experiments, the GCs were polished using 3, 1, and 0.3 µm of abrasive particle size polishing papers, followed by 5 min polishing with a suspension of alumina (0.05 µm particle size) in water. Finally, to remove the remaining alumina, the GCs were rinsed thoroughly with Milli-Q water, sonicated for 1 min in a mixture Milli-Q water and absolute ethanol, and left to dry under a nitrogen stream. A catalyst ink was obtained by dispersing 5 mg catalyst in 1 mL solvent mixture (490 µL ethanol absolute, 490 µL Milli-Q water, and 20 µL of a 5 wt.% Nafion dispersion). Finally, the mixture was sonicated for 30 minutes at room temperature to ensure a stable dispersion. A certain volume of this dispersion was pipetted on the GC to generate homogeneous catalyst films with a mass loading of 0.2 mg cm^{-2}.

OER measurements were performed using an Autolab potentiostat/galvanostat (PGSTAT302N, Methrom) and a rotating disk electrode (RDE) (Autolab RDE-2 rotator and motor controller, Methrom). A standard three-electrode configuration containing the catalyst modified GC, a Pt wire, and a double junction Ag/AgCl 3 M KCl as working, counter, and reference electrodes, respectively, were used. A glass frit was employed to separate the counter electrode from the bulk electrolyte. KOH solution (1 M KOH, pH 13.5) was used as the electrolyte in all electrochemical experiments. It was purified using a cation-exchange resin in its potassium form (Chelex 100, Sigma-Aldrich) following the procedure recommended by the producer.

The electrocatalytic activity of the materials was investigated in O_2 saturated 1 M KOH using linear sweep voltammetry (LSV) recorded from 0 to +1 V vs. Ag/AgCl (3 M KCl), with a scan rate of 5 mV s^{-1} and a rotation speed of 1600 rpm. Three measurements were conducted for each material, and the average values of these measurements were reported. Before recording the LSV, electrochemical impedance spectroscopy (EIS) was conducted at open-circuit potential (OCP) in the frequency range from 100 kHz to 100 Hz using an AC perturbation of 10 mV (RMS). All the potentials shown in this work were referred to the reversible hydrogen reference electrode (RHE) scale, and the conversion from the Ag/AgCl 3 M KCl to the RHE scale, was done using the following expression:

$$E_{\mathrm{RHE}} = E_{\mathrm{app}} + E^{\circ}_{\mathrm{Ag/AgCl/3M\ KCl}} + 0.059 \cdot \mathrm{pH} \qquad \text{[Eq. 1]}$$

where E_{RHE} is the electrode potential in the RHE scale (in V); E_{app} is the applied potential versus Ag/AgCl/3 M KCl (in V); $E^{\circ}_{\mathrm{Ag/AgCl}}$ is the standard potential of the Ag/AgCl (3 M KCl) reference electrode (0.21 V). Potential values were 100% manually *iR*-corrected using the following formula:

$$E'_{\mathrm{RHE}} = E_{\mathrm{RHE}} - iR_{\mathrm{u}} \qquad \text{[Eq. 2]}$$

Where E'_{RHE} is the *iR*-drop compensated potential (V), i is the measured current intensity (in A) and R_{u} is the uncompensated resistance determined by EIS (in Ω) in the high-frequency range.

The electrochemical surface area (ECSA) was determined following protocols described in literature.[3] Cyclic voltammograms were recorded in the OCP ± 0.05 V potential window using different scan rates (v): 0.005, 0.01, 0.025, 0.05, 0.1, 0.2 and 0.4 V s^{-1}. 10 s waiting time was used between the anodic and cathodic scans. From the CVs, the electrochemical double-layer capacitance (C_{DL}) was calculated using the following formulas:

$$C_{\mathrm{DL}} = i_{\mathrm{average}} / v \qquad \text{[Eq. 3]}$$

$$i_{\mathrm{average}} = (i_{\mathrm{a}\,-}\, i_{\mathrm{c}}) / 2 \qquad \text{[Eq. 4]}$$

Where i_{average} stands for the average value of anodic (i_{a}) and cathodic (i_{c}) currents in modulus at different scan rates, taken from the CVs at OCP. Then, ECSA was calculated by dividing the C_{DL} value with the specific capacitance (C_{S}) approximated to be 0.04 mF cm^{-2} in alkaline electrolyte:[3]

$$\mathrm{ECSA} = C_{\mathrm{DL}} / C_{\mathrm{S}} \qquad \text{[Eq. 5]}$$

Screening of catalyst stability based on fast benchmarking protocol: Galvanostatic measurements investigated initial evaluation of the stability of the hydroxynitrates samples. A current of 0.0011 A (corresponding to a current density of 10 mA cm^{-2}) was applied for 2 h. After the stability measurement, an LSV was recorded from 0 to +1 V vs. AgCl/Ag (3 M KCl) to explore changes in the electrocatalytic performance. The experimental conditions were the same as those described above.

OER Faradaic efficiency

Faradaic efficiency (FE) of the Ni-hydroxynitrates was evaluated using rotating ring disk electrode (RRDE) measurements. A rotating ring disk electrode device (rotor and motor controller, Methrom) was used along with the PGSTAT302N in the bipotentiostat mode for these measurements. The experiments were performed in an Ar-saturated 1 M KOH solution and a rotation speed of 3000 rpm. The potential of the Pt ring electrode was set at -0.7 V vs. Ag/AgCl (3 M KCl). Initially, OCP was applied to the disk electrode for 60 s to establish the background currents for both ring and disk electrodes. The potential of the disk electrode was further increased to +0.50 V vs. Ag/AgCl (3 M KCl) and kept at this potential for 500 s. The FE was calculated using the following formula:

$$\mathrm{FE} = |I_{\mathrm{ring}}| \,/\, (N \cdot I_{disk}) \qquad \text{[Eq. 6]}$$

where N is the collection efficiency. The collection efficiency was determined using an Ar-saturated solution of 5 mM $K_3[Fe(CN)_6]$ in 1 M KOH. The potential of the Pt ring electrode was kept at +0.4 V vs. Ag/AgCl/3 M KCl, while the potential of the disk electrode was swept from +0.5 to -0.2 V vs. Ag/AgCl (3 M KCl) with a scan rate of 5 mV s^{-1}. The calculated collection efficiency (N) is 0.18 for the Ni-hydroxynitrate sample and 0.25 for Co-hydroxynitrate.

Considering the high currents obtained with Co-hydroxynitrate, the O_2 FE was further investigated through gas chromatography. Experiments were conducted in an H-type cell with an air-tight electrode compartment connected to the gas chromatograph. An anion exchange membrane (fumasep® FAB-PK-75, Fumatech) was used to separate catholyte and anolyte compartments. The reference electrode was a leakless Ag/AgCl (3 M KCl) reference electrode immersed in the working solution (deoxygenated purified 1 M KOH). A Pt mesh was used as the counter electrode. The working electrode consisted of a Co-hydroxynitrate drop-coated carbon paper (H23, Quintech) with a catalyst loading of 1 mg cm^{-2}. The catalyst was drop-coated using the same ink composition mentioned above in this section. The piece of carbon paper used had a geometric area of 1 cm x 1 cm, and both sides of the paper were drop-coated (total geometric area = 4 cm^2). Oxygen was quantified during electrolyzes conducted at different current densities (3.75 up to – 50 mA cm^{-2}) for 15 min each. An aliquot of the oxygen produced in the anode chamber was automatically into the gas chromatograph and analyzed online in all the experiments. The gas chromatograph used was an SRI 8610C MG1 Multiple Gas Analyzer System equipped with a packed 3 m HaySep D column (SRI instruments). O_2 was analyzed using a thermal conductivity detector (TCD), previously calibrated with O_2 and N_2 mixtures. High purity nitrogen (99.999 %) was used as the carrier gas in the gas chromatograph. N_2 was also used to deoxygenate the solution and carry the gases from the H-type cell to the chromatograph, with a flow rate of 10 mL min^{-1} provided by a flow mass controller. The FE for O_2 was also calculated during 2 h electrolysis at 10 mA cm^{-2}. In this case, a constant current was applied for 2 h, and each 15 min, a sample was injected in the gas chromatograph and thus analyzed.

The FE was calculated using the following formula:

$$FE = \frac{C_{\mathrm{O2}} \cdot j_{\mathrm{N2}} \cdot 4 \cdot F}{V_{\mathrm{m}} \cdot I} \cdot 100\ (\%) \qquad \text{[Eq. 7]}$$

Where: C_{O2}- is the O_2 concentration obtained from the gas chromatograms, j_{N2} is the N_2 flow- the carrier gas, F is the Faraday constant, V_{m}- molar volume, and I is the electrolysis current.

S.1. Rotating ring disk electrode (RRDE) measurements.

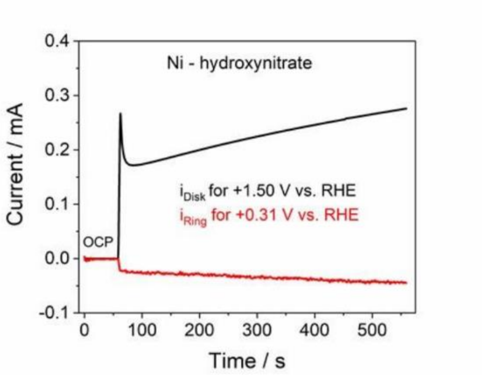

Figure S1. Chronoamperometric measurement was performed using Ni-hydroxynitrate coaded GC to calculate the Faradaic Efficiency towards O_2 formation. The WE are set at OCP for the first 60 s and then swept up to +1.50 V vs. RHE for 500 s. RRDE measurements were recorded under 3000 rpm and with a constant electrode potential of +0.31 V vs. RHE in the Pt ring.

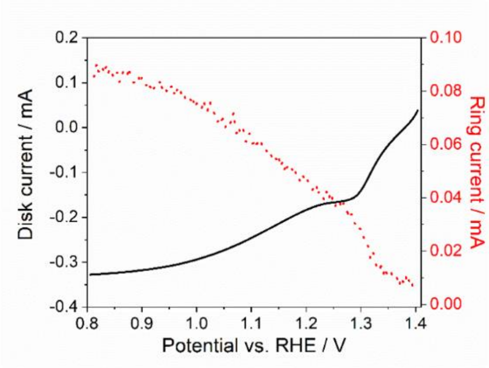

Figure S2. RRDE experiments performed to determine the collection efficiency (N) for the Ni-hydroxynitrate modified GC electrode using an Ar-purged 5 mM $K_3[Fe(CN)_6]$ in 1 M KOH solution.

S.2. Faradaic efficiency for OER determined by gas chromatography measurements.

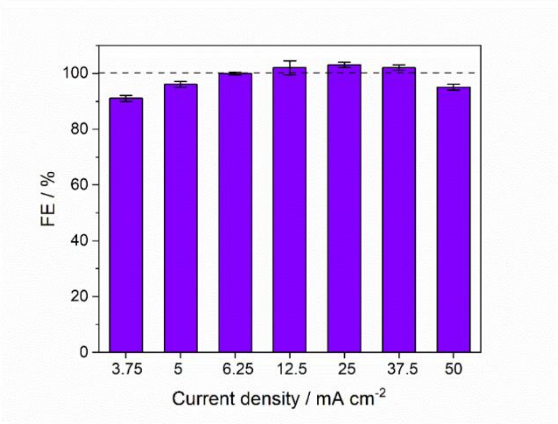

Figure S3. O_2 faradaic efficiencies were calculated at different current densities used for the galvanostatic water electrolysis using Co-hydroxynitrate as electrocatalyst. (Electrode geometric area = 4 cm^2). The O2 concentrations obtained based on two chromatograms were used to calculate the FE, and the data are averaged.

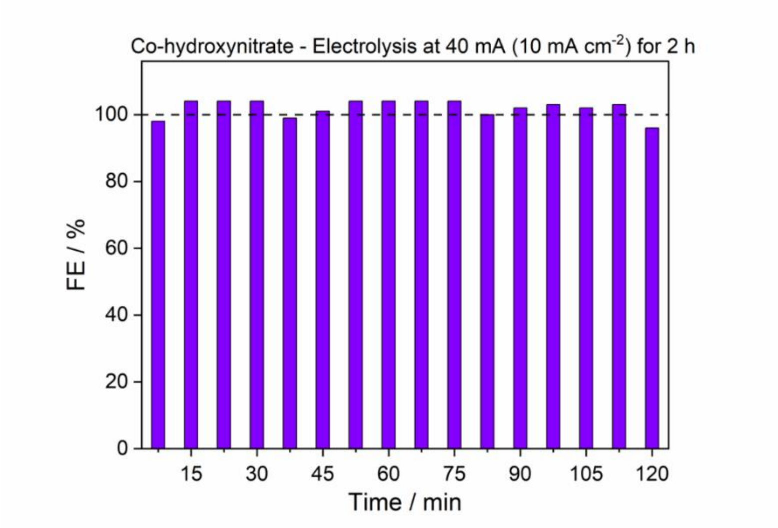

Figure S4. O_2 faradaic efficiencies evaluated over 2 h at the 15-minute interval while performing water electrolysis galvanostatically at 10 mA cm^{-2} (40 mA) using Co-hydroxynitrate as electrocatalyst. O_2 quantification was performed by gas chromatography every 7.5 minutes.

S.3. Post-mortem SEM characterization.

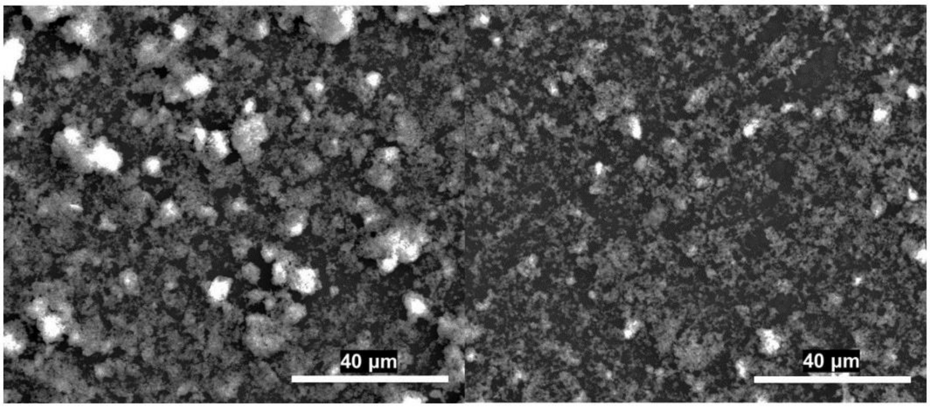

Figure S5. SEM images of the Co-hydroxynitrate modified GC electrode before (left) and after (right) 2 h chronopotentiometry measurement performed at a current of 1.134 mA corresponding to 10 mA cm^{-2} current density.

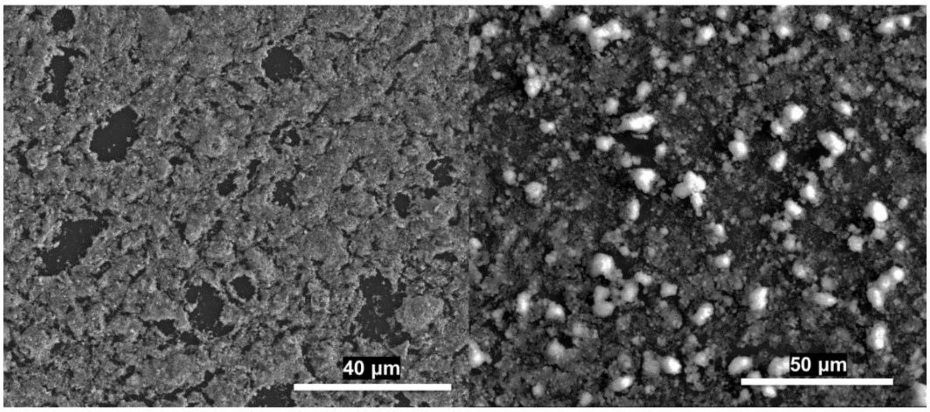

Figure S6. SEM images of the Ni-hydroxynitrate modified GC electrode before (left) and after (right) 2 h chronopotentiometric measurement performed at a current of 1.134 mA, corresponding to 10 mA cm^{-2} current density.

S.4. Stability measurements.

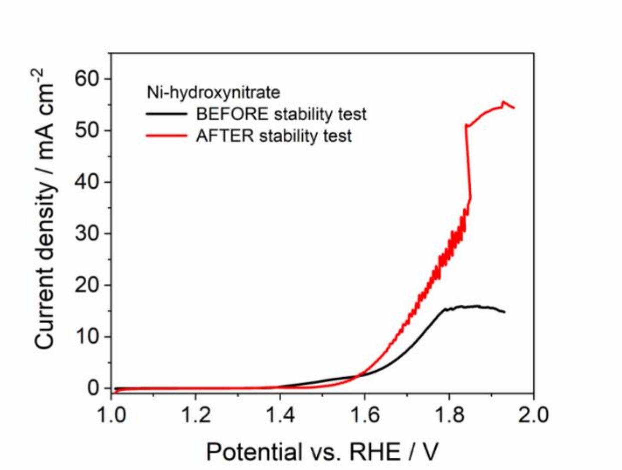

Figure S7. LSVs performed for Ni-hydroxynitrate modified GC electrode before and after a stability measurement based on applying 10 mA cm^{-2} for 2 h. LSV were recorded in a O_2-saturated 1 M KOH solution with a rotation of 1600 rpm.

S.5. Post-mortem XRD characterization

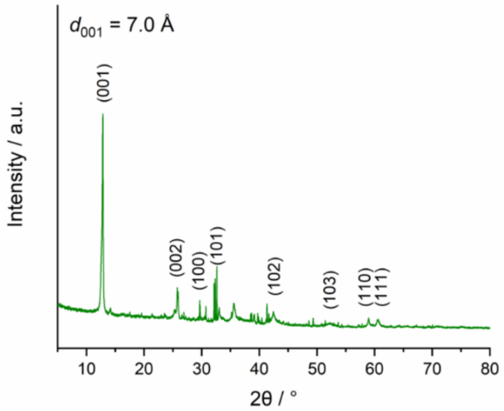

Figure S8. Post-electrolysis XRD performed for Ni-hydroxynitrate after electrolysis performed at 0.55 V vs. Ag/AgCl 3 M KCl in 1 M KOH for 2 h.

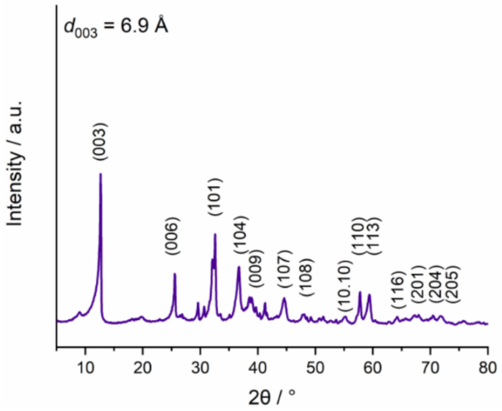

Figure S9. Post-electrolysis XRD performed for Co-hydroxynitrate after electrolysis performed at 0.55 V vs. Ag/AgCl 3 M KCl in 1 M KOH for 2 h.

S.6. Post-electrolysis EDX characterization

Energy dispersive X-ray (EDX) spectroscopy measurements of Ni- and Co-hydroxynitrate samples were conducted to rule out the incorporation of secondary metals during the chronopotentiometry experiment (10 mA cm^{-1} for 2 h). The obtained results present no evidence of such metal (particularly Fe) incorporation. The only additional signals not belonging to the catalyst can be attributed to the Nafion binder (F, S) and traces of electrolyte (K). The investigation included probing each sample at 10 different spots from which two representative EDX spectra of points 1 and 2 are shown.

Ni-hydroxynitrate

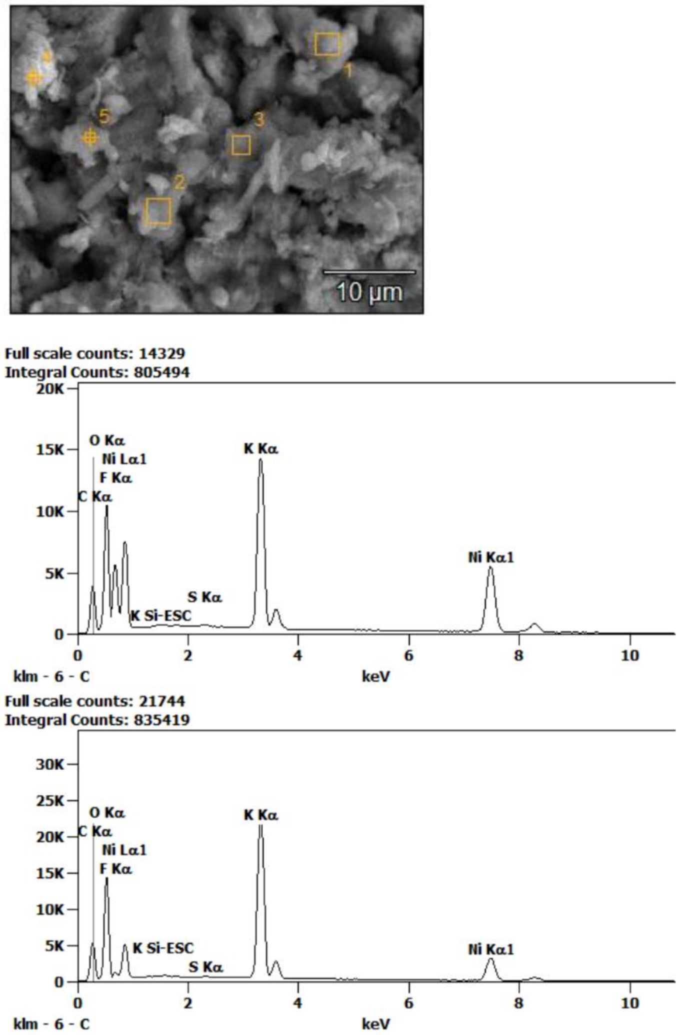

Figure S10. EDX characterization of Ni-hydroxynitrate after 2 h chronopotentiometry measurement performed at a current of 1.134 mA, corresponding to 10 mA cm^{-2} current density.

Co-hydroxynitrate

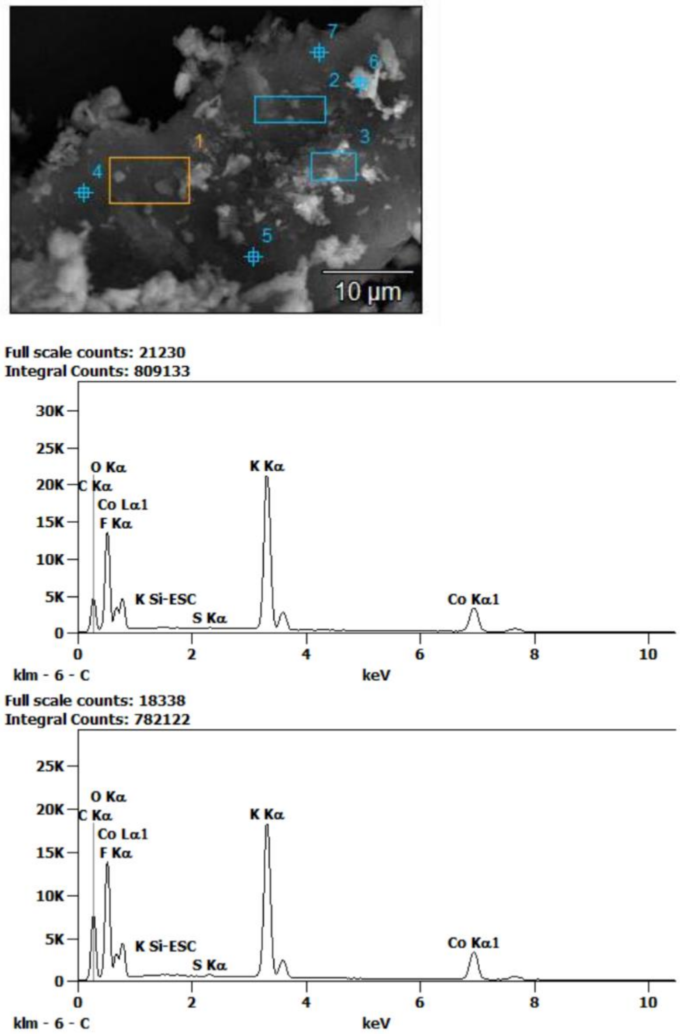

Figure S11. EDX characterization of Co-hydroxynitrate after 2 h chronopotentiometry measurement performed at a current of 1.134 mA, corresponding to 10 mA cm^{-2} current density.

[1] U. Costantino, F. Marmottini, M. Nocchetti, R. Vivani, *Eur. J. Inorg. Chem.* **1998**, *1998*, 1439-1446.

[2] a) K. Petrov, N. Zotov, O. Garcia-Martinez, R. Rojas, *J. Solid State Chem.* **1992**, *101*, 145-153; b) D. Louër, *J. Solid State Chem.* **1975**, *13*, 319-324; c) M. Louer, D. Louer, D. Grandjean, D. Weigel, *Acta Crystallogr. Sect. B: Struct. Sci.* **1973**, *29*, 1707-1710; d) M. Rajamathi, P. Vishnu Kamath, *J. Power Sources* **1998**, *70*, 118-121.

[3] C. C. L. McCrory, S. Jung, J. C. Peters, T. F. Jaramillo, *J. Am. Chem. Soc.* **2013**, *135*, 16977-16987.

6.3 Grafting control – OER catalysis through a scalable Fe-corrosion process

Sustainable oxygen evolution catalysis – electrochemical generation of mössssbauerite via corrosion engineering of steel

Sebastian Weiß[a,b], A.V. Radha[b], Michael Ertl[b], Catherine McCammon[a], Josef Breu[a,b]*

Published in Materials Advances **2021**, 2, 5650-5656.

Impact Factor (2023) Materials Advances: 3.18
DOI: 10.1039/d1ma00381j

[a] Bavarian Center for Battery Technology (BayBatt), University of Bayreuth, Universitätsstr. 30, 95447 Bayreuth, Germany

[b] Department of Chemistry, University of Bayreuth, Universitätsstr. 30, 95447 Bayreuth, Germany. E-mail: josef.breu@uni-bayreuth.de

[c] Bayerisches Geoinstitut, University of Bayreuth, Universitätsstr. 30, 95447 Bayreuth, Germany

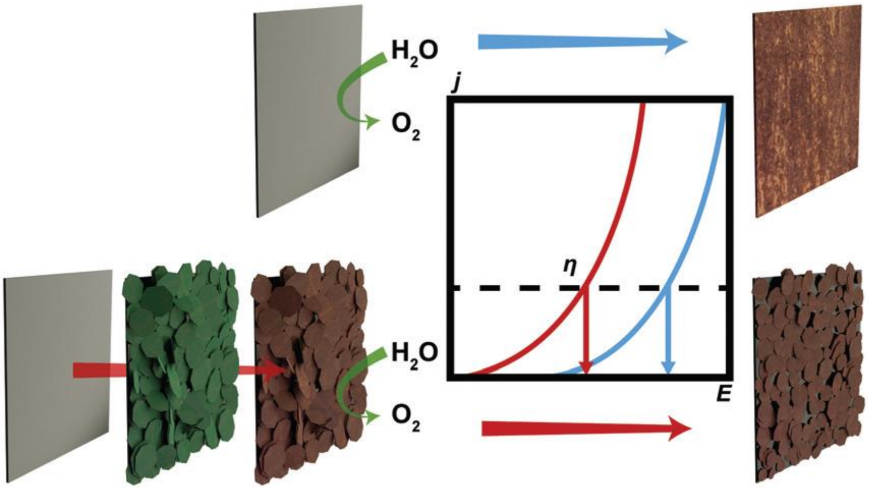

Materials Advances

PAPER

View Article Online
View Journal | View Issue

Check for updates

Cite this: *Mater. Adv.*, 2021, 2, 5650

Sustainable oxygen evolution catalysis – electrochemical generation of mössbauerite *via* corrosion engineering of steel†‡

Sebastian Weiß,[ab] A. V. Radha,[b] Michael Ertl,[b] Catherine McCammon[c] and Josef Breu*[ab]

Received 27th April 2021,
Accepted 13th July 2021

DOI: 10.1039/d1ma00381j

rsc.li/materials-advances

A versatile electrochemical corrosion process was used to generate green rust (GR) on a steel substrate and to transform it into the trivalent iron-only oxygen evolution catalyst mössbauerite (GR*) upon a subsequent oxidation process. Besides being scalable, cheap, and time-efficient, the demonstrated procedure is based on earth-abundant and non-hazardous materials only. Oxidation of mixed-valence Fe^{2+}/Fe^{3+} GR to GR* was achieved by chemical and electrochemical processes. The latter induces less grafting of interlayer CO_3^{2-}, leading to less contraction of the interlayer space and a reduction in the observable stacking disorder. The direct electrodeposition of the catalyst on a conductive substrate enabled the first systematic study of the impact of grafting on the performance of GR* in the oxygen evolution reaction (OER). The materials subjected to chemical (GR^*_{ChOx}) and electrochemical oxidation (GR^*_{ElOx}) allowed obtaining a current density of 100 mA cm^{-2} at 1.82 V and 1.84 V, respectively, thus improving the electrocatalytic capabilities and outperforming the bare steel substrate operated in 1 M KOH solutions.

Introduction

Resolving energy and environmental issues has been receiving enormous attention. It can be regarded as the critical challenge of the 21st century.[1,2] Most of the proposed strategies focus on renewable energies to curb CO_2 emissions by gradually turning away from conventional fossil energy sources. Due to the intermittent nature of these energy sources, suitable storage methods are imperative to provide a continuous energy supply for grid management.[3] For instance, energy can be stored in the form of chemical bonds, *e.g.*, hydrogen. However, the bottleneck for establishing a hydrogen-based storage cycle is linked to the oxidative half-reaction, called the oxygen evolution reaction (OER).[4] Moreover, for green energy production, environmentally friendly, earth-abundant, non-hazardous, and affordable elements allowing for technically benign processing are preferred. Such materials with efficient and durable electrocatalytic properties will play a pivotal role in future developments in this field.[5]

Ideally, cheap and scalable anodes for the OER are highly sought-after since noble metal oxides are considered unsuitable due to dissolution, high production price, and catalyst material maintenance.[6] Being affordable and easy to manufacture, iron-based electrodes represent a viable option. Unfortunately, under OER operating conditions, the Pourbaix diagram of iron implies the dissolution of the electrode through the formation of ferrate (FeO_4^{2-}) anions.[7] The dissolved ferrate is not stable in aqueous environments at pH 14 and will thus oxidize water to produce oxygen.[8] Concomitantly, with the reduction of the ferrate, undesirable corrosion products of iron are formed on the steel surface.[9] The formation of this passivation layer may impede further corrosion but may also impair the performance of the electrode due to the low conductivity and/or lacking activity of the formed products.[10]

Using stainless steel, this uncontrolled rusting of the electrode can be mitigated. Among the other transition metal additives, stainless steels typically contain at least 12 wt% of chromium to reduce susceptibility to corrosion.[11] Under ambient conditions, a thin chromium oxide layer passivates the surface. This, however, has been reported to contribute little or even reduce the OER activity of the stainless steel.[12,13] The Pourbaix diagram of Cr, moreover, indicates that the formation of CrO_4^{2-} is thermodynamically favored under OER operating

---

[a] *Bavarian Center for Battery Technology (BayBatt), University of Bayreuth, Universitätsstr. 30, 95447 Bayreuth, Germany*
[b] *Department of Chemistry, University of Bayreuth, Universitätsstr. 30, 95447 Bayreuth, Germany. E-mail: josef.breu@uni-bayreuth.de*
[c] *Bayerisches Geoinstitut, University of Bayreuth, Universitätsstr. 30, 95447 Bayreuth, Germany*

† Dedicated to Prof. Dr Wolfgang Schuhmann on the occasion of his 65th birthday.

‡ Electronic supplementary information (ESI) available: CV, SEM, Mössbauer spectroscopy, CP, and post-catalysis SEM/XRD. See DOI: 10.1039/d1ma00381j

conditions.[14] Indeed, previous studies have shown Cr leaching into the electrolyte in the long term.[13,15,16] The dissolution of chromium under sufficiently high anodic potentials has even been utilized to obtain thin Ni–Fe oxide layers representing a robust OER catalyst.[17] However, Cr(VI) is known to be carcinogenic and must not be released into the environment but rather needs to be completely removed upon exchanging the electrolyte.[18,19] Nevertheless, these and other[13,20,21] studies clearly have proven the efficiency of oxidic layers on Fe-based substrates for OER catalysis. The steel types applied, however, often contain environmentally unfriendly or even toxic elements like Co, Cr, and Ni while processing often is time-consuming and requires harsh conditions.

Layered double hydroxides (LDHs) are regarded as one of the most promising classes of OER catalysts[22] owing to the fact that they exhibit compositional flexibility and allow for tuning of the morphology. When optimizing the electrocatalytic properties, these features allow for the optimization of electronic structures while providing high specific surface area at the same time.[22] Generally, the composition of carbonate-LDHs can be described as $M_{6-x}^{2+}M_x^{3+}(OH)_{12}(CO_3)_{x/2}\cdot nH_2O$ with $0 \leq x \leq 2$. Previously, we have shown that the trivalent Fe-only (oxy)hydroxide mössbauerite (GR*; $Fe^{III}_6(O)_4(OH)_8(CO_3)\cdot 3H_2O$) is an n-type semiconductor and exhibits electrocatalytic activity promoting the OER.[23] The catalyst is obtained by the quick oxidation of the mixed-valence mineral green rust (GR; $Fe^{II}_4Fe^{III}_2(OH)_{12}(CO_3)\cdot 3H_2O$). In terms of structure, GR consists of positively charged brucite-like layers containing di-/trivalent cations, interlayered anions, and structural water.[24] Under ambient oxygen fugacity, GR is susceptible to oxidation and can form various ferric oxyhydroxides like goethite, feroxyhyte, and lepidocrocite.[25,26] However, fast chemical oxidation using H_2O_2 leads to the formation of GR*.[23]

Herein, we report the direct electrochemical coating of environmentally friendly, all-iron GR on a steel surface and its subsequent conversion into the efficient OER catalyst GR* (Fig. 1). Anodes are fabricated from inexpensive steel *via* an electrochemical corrosion process producing GR, which is subsequently transformed into the active OER catalyst GR*. Two alternative routes for the conversion were explored, which influence the grafting behavior of the interlayer carbonate: either *via* chemical oxidation (GR*$_{ChOx}$) using H_2O_2 or *via* an electro-oxidation process (GR*$_{ElOx}$). The variation in the structure and the electrochemical performance of the oxidized products obtained by these two methods are compared.

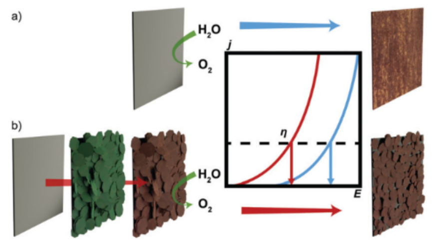

Fig. 1 Schematic comparison of the current–voltage curve for the OER of an unmodified bare steel substrate (a) and the same substrate coated with the all-iron electrocatalyst GR* *via* a corrosion engineering process (b).

Experimental

Materials

All solutions used to synthesize the catalysts were prepared with Ar-saturated Milli-Q water (18.2 MΩ cm). Hydrogen peroxide solution (30%) and ethanol absolute were supplied by VWR Chemicals. Potassium hydroxide was ordered from Bernd Kraft GmbH and sodium bicarbonate from Grüssing GmbH. Substrates were prepared using custom-cut steel plates (DC 01 – DIN EN 10130, Maschinenbau Feld GmbH). The nail varnish (shine last & go! gel nail polish; absolute pure) was bought from Cosnova GmbH.

Electrodeposition of GR and its conversion into GR*

Steel plates were cut to square-sized pieces of 1.4 cm length and any potentially pre-formed corrosion products were removed using grade P400 grinding paper and were further polished with 0.3 μm Al_2O_3 powder. Then, they were cleaned by ultrasonication with ethanol for 5 minutes. Finally, each electrode was rinsed with water and ethanol to remove the remaining loose metal particles and organic contaminants. Electrical contact was provided by using a PTFE-insulated Ag-wire and conductive silver adhesive. UV-curing glue was used to seal any exposed silver. According to a previously published procedure,[27] the plates were placed in a 0.4 M $NaHCO_3$ solution with the pH adjusted to 9.6 by the dropwise addition of 10 M NaOH solution. Electrodeposition and electro-oxidation were conducted using a CH-Instruments potentiostat 710E in a 3-electrode setup. A Fisher-type double net Pt/Ir electrode (∅ 3 cm) and a HydroFlex® hydrogen reference electrode from Gaskatel were used as the counter electrode and reference electrode, respectively. The plates were cycled from 0 to 0.2 V *vs.* RHE for 90 cycles with a scan speed of 10 mV s^{-1}. After completion, a greenish deposit was visible on the surface of the substrate. As a control experiment, the substrate was immersed in the given solution without any applied potential. Here, no formation of a deposit was observed after 12 weeks.

For the complete oxidation of the mixed-valence GR to GR*, two different methods were employed. For chemical oxidation, the sample was immersed in 40 mL of a 25 mM aqueous solution of H_2O_2. Electrochemical oxidation was achieved by simply increasing the voltage from 1.10 to 1.47 V *vs.* RHE (typically 5–10 cycles) and subsequently to the electrodeposition of GR. Scanning experiments were performed until no notable current was detectable. Both procedures yielded orange-brown deposits on the steel substrate plates and were then applied as anodes.

Structural characterization of the materials

To allow for quick measurements to minimize oxidation, powder X-ray diffraction (PXRD) traces for GR were collected using a Bragg–Brentano-type diffractometer (Empyrean) with a Ni-filtered Cu K_α radiation source (λ = 1.540598 Å) equipped with a PIXcel detector. To further reduce fluorescence, PXRD patterns of air-stable GR*-samples were collected using a STOE STADI-P diffractometer with a Ag $K_{\alpha 1}$ radiation source (λ = 0.5594075 Å) in transmission geometry equipped with four MYTHEN2 R 1 K detectors. Data collection was performed in the static mode for one hour, with samples loaded in 0.5 mm glass capillaries. However, to assist comparability, the diffraction traces acquired with Ag $K_{\alpha 1}$ radiation (Fig. 2b) were recalculated assuming Cu K_α radiation. The infrared spectra of the powder samples were recorded using a JASCO FT-IR 6100 spectrometer (400–4000 cm^{-1} range, 1 cm^{-1} resolution). Transmission electron microscopy (TEM) images were obtained using a Zeiss/LEO EM922 Omega transmission electron microscope. Scanning electron microscopy (SEM) images were acquired using a Zeiss/LEO 1530 system. For Mössbauer spectroscopy, a small amount of the powder sample was mixed with transparent nail varnish and spread over a region of 1 mm diameter on a plastic foil. The dimensionless effective sample thickness was estimated to be 12 ($\sim$30 mg Fe cm^{-2}), which is close to the optimum thickness for this composition.[28] The Mössbauer spectra were recorded at room temperature (293 K) in the transmission mode using a constant acceleration Mössbauer spectrometer with a nominal 370 MBq ^{57}Co high specific activity source in a 12-μm-thick Rh matrix.[29,30] The velocity scale was calibrated relative to a 25-μm-thick α-Fe foil using the positions certified for the (former) National Bureau of Standards, standard reference material no. 1541; line widths of 0.36 mm s^{-1} for the outer lines of α-Fe were obtained at room temperature. The spectrum was collected for one day. The Mössbauer spectra were fitted with MossA software[31] using the full transmission integral. Data were fitted into doublets with pseudo-Voigt lineshape and conventional constraints (doublet components constrained to have equal widths and areas).

Electrochemical characterization

Electrochemical characterization was performed using an Autolab potentiostat/galvanostat PGSTAT204. Counter and reference electrodes were the same as those used for the preparation of the material. If not noted otherwise, all electrocatalytic performance measurements were performed in O_2 saturated 1 M KOH solutions. The electrolyte for all measurements was purified using the cation-exchange resin Chelex® 100 (Bio-Rad Laboratories) following the procedure recommended by the producer.[32] For electrochemical measurements, the exposed surface area was reduced to 1 cm^2 by sealing the rest of the plate with hot melt adhesives. The obtained potentials were corrected by 85% of the uncompensated resistance (*iR*) determined *via* current interrupt. Polarization curves were acquired by performing linear sweep voltammetry (LSV) in the range of 1.0–2.5 V with 5 mV s^{-1}. The overpotential (η) is given as the voltage potential difference of 1.23 V. Stability measurements were performed galvanostatically by applying a current of 10 mA, corresponding to a current density of 10 mA cm^{-2}, for 24 h. Galvanostatic stability experiments were carried out without *iR* compensation.

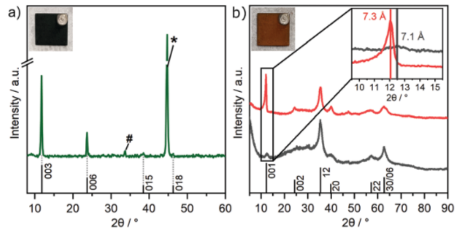

Fig. 2 PXRD patterns of (a) GR on a steel substrate as obtained through an electrochemical corrosion engineering process (*: substrate, #: partially oxidized product formed during measurements) and (b) scraped off GR* powder as obtained through electro-oxidation (GR^*_{ElOx}; red) and chemical oxidation (GR^*_{ChOx}; gray) of GR. Photographs of GR and GR^*_{ElOx} are shown in the insets.

The determination of the electrochemically active surface area (ECSA) was performed by cyclic voltammetry (CV) measurements in an Ar-saturated 1 M KOH at various scan rates (10, 20, 40, …, 100 mV s^{-1}) in the potential window between 0.210 V and 0.310 V *vs.* RHE where there was no faradaic current response. The double-layer capacitance (C_{dl}) was estimated by plotting $\Delta j = j_a - j_c$ at 0.260 V as a function of the scan rate ν (eqn (1)).[33]

$$C_{dl} = 0.5\cdot(d(\Delta j)/d\nu) \qquad (1)$$

The ECSA was calculated by dividing C_{dl} by the specific capacitance C_s of a flat surface. A value of C_s = 0.04 mF cm^{-2} was reported as an average value for different metal electrodes in an alkaline environment.[34]

Results and discussion

Various strategies have been employed to synthesize GR. These include Fe^{II}/Fe^{III} co-precipitation,[23] oxidation of ferrous hydroxide,[35] bacterial reduction of ferric compounds,[36] and electrosynthesis.[37] Formation of carbonate interlayered GR has been followed by Génin *et al.* by tracking the E_h during the reaction.[38] They further constructed the corresponding Pourbaix diagram, which identifies the stability field of GR with variation in pH and E_h.[38] Based on previous investigations, a pH of 9.6 was considered most suitable to enable a successful deposition.[27] For this pH, the E_h range of GR can be identified to be located between 0 V and 0.15 V. For cyclic voltammetry, the window was chosen from 0 V to 0.2 V to account for possible overpotentials. After cycling, a greenish deposit was formed on the steel electrode. The intensity of the wave peak recorded during deposition increased steadily, indicating the thickening of the deposited material layer with time (Fig. S1, ESI‡). The obtained product was characterized utilizing XRD directly on the steel substrate to minimize unintended oxidation by air (Fig. 2a).

The diffraction pattern of GR is in accordance with previous reports on the material (PDF #00-046-0098).[23,39,40] The *d*-spacing of 7.5 Å for the first reflection is characteristic for GR containing carbonate ions in the interlayer space and is usually assigned as the 003 plane of the $3R_1$ polymorph.[23,40] The coefficient of variation of the average of the basal spacing as calculated from individual $00l$ reflections was found to be small for GR (0.12%).

This indicates little variance in the stacking distance of individual interlayers.[39] As previously found, the remaining, weak in-plane reflections observed are in line with the $3R_1$ polymorph.[23,40] A prominent reflection at 44.7° is caused by the underlying substrate and can be assigned to α-Fe(110) (PDF #00-006-0696).

Because of the oxygen sensitivity of GR,[25] a controlled oxidation process is necessary to obtain phase pure GR*.[23] Previously, we have shown that this can be achieved by subjecting GR to a H_2O_2 treatment as it allows rapid oxidation. Applying this chemical oxidation (GR^*_{ChOx}) to the GR deposited on the steel electrode led to an immediate color change from green to orange-brown. Alternatively, the previously deposited GR on the steel substrate was subjected to electrochemical oxidation (GR^*_{ElOx}) *via* cyclic voltammetry in the range of 1.10–1.47 V *vs.* RHE. A similar color change to orange-brown was observed. A suitable potential range to facilitate the oxidation was identified using cyclic voltammetry over a broad range from 0.60 to 1.57 V (Fig. S2, ESI‡). Because both GR* samples are air-stable, the obtained products were scraped off the plate before being characterized using XRD (Fig. 2b).

The powder XRD patterns of both GR* samples exhibit very few asymmetric and rather broad reflections. The featureless diffraction pattern is typical for GR*.[23,39,41] The diffraction pattern can be fully explained with a turbostratic disorder and concomitant interstratification of domains with grafted carbonate and domains with intercalated carbonate. In any case, side phases are not indicated in the diffraction pattern. This is in contrast with previous reports, where GR was oxidized in an ambient atmosphere or by bubbling oxygen through the suspension where mixtures of GR* with goethite are obtained instead of phase pure GR*.[27,42] Both the strategies presented herein, however, yield the desired product with no side phases. The first reflex of GR* appears at 7.1 Å (GR^*_{ChOx}) and 7.3 Å (GR^*_{ElOx}) and has been related to the basal spacing.[41] However, an integral $00l$ series is missing, indicating heavy random interstratification. The apparent basal spacing of both samples is lower as compared to that of the mixed-valence parent GR (7.5 Å).[40] In GR^*_{ElOx}, the (001) reflection is rather sharp and more intense as compared to that in GR^*_{ChOx}. Moreover, even the (002) reflection (d = 3.7 Å) is visible while being submerged into the background when the oxidation is performed chemically.

We have previously shown that the oxidation of mixed-valence Fe-LDHs triggers partial grafting (*i.e.*, chemical bonding) of interlayer carbonate to the brucite-like layers.[39] Density functional theory (DFT) calculations have shown that the completely grafted structure shows a basal spacing, which is 0.3 Å smaller than that for the non-grafted LDH.[39] A similar trend was found in CoFe-LDHs, where it was found that a higher Fe-content promoted more grafting.[43] In the presence of H_2O_2, the grafting was shown by DFT to proceed exothermically, which constitutes the driving force for the grafting process.[39] Grafting can also be qualitatively supported by FT-IR, as discussed below. Thus, the variations in the apparent basal spacings found for GR^*_{ChOx} and GR^*_{ElOx} are attributed to a random interstratification of grafted and intercalated domains. The higher intensity and higher d-value observed for GR^*_{ElOx} indicate significantly fewer grafted domains being produced by electrochemical oxidation as compared to chemical oxidation (GR^*_{ChOx}). Employing electro-oxidation (*i.e.*, in the absence of H_2O_2), the driving force for grafting might be smaller as compared to chemical oxidation and consequently, more intercalated (*i.e.* ungrafted) domains contribute to random interstratification leading to an overall higher observed basal spacing of 7.3 Å.

To corroborate the varying grafting probability with the oxidation method, FT-IR spectra were recorded (Fig. 3). Based on the symmetry of the carbonate ion, it is possible to experimentally distinguish between non-grafted interlayer carbonate and carbonate ions that are grafted to the brucite layers. The former features a D_{3h} symmetry, whereas the latter shows symmetry reduction to C_{2v}. As shown in the previous work, the ν_3 vibration band of CO_3^{2-} at 1350 cm^{-1} may be used to quantify grafting. Symmetry reduction due to grafting manifests as an energetic splitting of this band to a second one observable at 1485 cm^{-1}, which is characteristic of the grafted carbonate species.[39] Irrespective of the oxidation method, these two bands are present. The relative intensity of these two bands furthermore allows for the assessment of the extent of grafted and non-grafted species qualitatively. Both bands, assigned to grafted and ungrafted carbonate species, exhibit roughly similar intensity for GR^*_{ChOx}. For GR^*_{ElOx}, however, the band's relative intensity at 1485 cm^{-1} is notably decreased. Thus, it can be concluded that grafting of carbonate species is less prevalent when performing electro-oxidation. This phenomenon is in line with the above interpretation of the XRD patterns (Fig. 2b). It suggests that oxidation with a potent

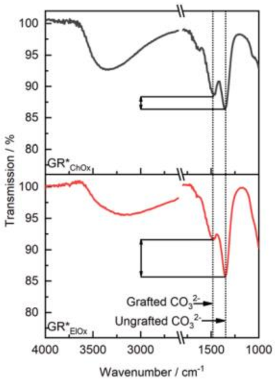

Fig. 3 Normalized FT-IR spectra of GR^*_{ChOx} (gray) and GR^*_{ElOx} (red). Carbonate peak splitting is found in both samples. Based on the relative intensity of grafted and ungrafted carbonate peaks, a lower proportion of grafted CO_3^{2-} can be obtained for GR^*_{ElOx}.

chemical oxidation agent, such as H_2O_2, provides a stronger driving force for grafting as compared to electro-oxidation.

Besides basal reflections, only asymmetric, non-uniformly broadened reflections are observed in the diffraction patterns of both GR* samples. As previously shown,[39] they originate from two-dimensional diffraction by the brucite layers being stacked with the random phase (turbostratic disorder) leading to *hk*-bands.

The SEM images of both GR* samples (Fig. S3a–d, ESI‡) confirm the coating on the substrate. The micrographs of the bare steel substrate merely show some surface roughness due to polishing (Fig. S3e and f, ESI‡). For both chemically and electrochemically oxidized samples, the deposited layer features a plate-like morphology typically observed for LDHs. The steel substrate is completely coated and the coating appears to be uniform. The platy crystals of both GR* samples feature dimensions ranging from 0.4 μm to 4.5 μm in diameter and 40–80 nm in thickness. Large platelets are found to be intergrown, with smaller platelets providing an increased number of edges and corner sites, contributing to the OER activity.[22] A similar appearance of both samples indicates the topotactic transformation of GR to GR* and thus the morphology is determined already in the first step, the electrochemical deposition of GR, with little to no morphology change occurring upon the formation of GR*.[44] This conclusion is supported by the SEM micrographs of GR acquired prior to oxidation (Fig. S4, ESI‡).

The Mössbauer spectra of chemically and electrochemically oxidized samples are also very similar (Fig. S5, ESI‡). The ^{57}Fe spectra were acquired at room temperature consisting of a single, broad doublet with a mean quadrupole splitting of 0.67 mm s^{-1} and 0.75 mm s^{-1} and an isomer shift of 0.35 mm s^{-1} and 0.36 mm s^{-1} with respect to metallic iron. These values agree well with those expected for GR*.[40,41] Complete oxidation from Fe^{2+} to Fe^{3+} can be achieved for both samples as no residual ferrous doublet can be observed in the acquired spectra. Not surprisingly, Mössbauer spectroscopy is insensitive to the degree of grafting.

Both GR* samples were tested for OER catalysis. The electrochemically active surface area (ECSA) is calculated (Fig. 4a) by performing CV in a non-faradaic regime at different scan rates (Fig. S6, ESI‡). Due to the influence of the setup and the method of determining the absolute ECSA,[12] we only use the ECSA as an activity parameter to compare the samples obtained within this study. For this purpose, the relative ECSA of the untreated steel plate is compared with those of GR*$_{ChOx}$ and GR*$_{ElOx}$.

Compared to a non-coated sample, the controlled corrosion producing GR and then GR* leads to an approximately 2.4- and 2.7-fold increase in the ECSA for GR*$_{ChOx}$ and GR*$_{ElOx}$, respectively. Regarding the different oxidation methods, GR*$_{ElOx}$ has a slightly higher relative ECSA.

LSV experiments are performed and compared to the overpotential (η) of the uncoated substrate (Fig. 4b). Comparing the two GR* samples with varying degrees of grafting furthermore will allow for the first-time conclusion regarding the effect of grafting on the OER performance.

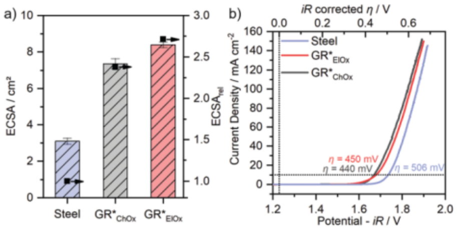

Fig. 4 (a) Electrochemically active surface area with normalized relative ECSA and (b) linear sweep voltammograms for all three samples: the pristine steel plate, GR*$_{ElOx}$, and GR*$_{ChOx}$. LSVs were recorded with a scan rate of 5 mV s^{-1} in O_2-saturated purified 1 M KOH solutions.

GR*$_{ChOx}$ and GR*$_{ElOx}$ showed overpotentials of η = 440 mV and η = 450 mV, respectively, at a current density of 10 mA cm^{-2} while for the uncoated bare steel plate, η = 506 mV is necessary. A current density of 100 mA cm^{-2} was reached at the overpotentials of 598 mV for GR*$_{ChOx}$ and 610 mV for GR*$_{ElOx}$. The absence of any notable pre-peaks is consistent with the expectations and conclusions from the Mössbauer spectroscopy measurements, as both electrocatalysts have been fully oxidized to the all-ferric oxidation state.

Compared to the uncoated steel plate, both GR* catalyst materials show a clear OER activity improvement. The overpotentials at 10 mA cm^{-2} are in the range reported for mössbauerite synthesized at room temperature (η = 540 mV) and at a temperature of 50 °C (η = 400 mV). The offset may be attributed to the different synthesis methods and the rotating disc electrode setup being used to determine the latter values.

Despite the slightly higher ECSA of GR*$_{ElOx}$ compared to GR*$_{ChOx}$, the latter exhibits a higher activity over the probed potential range. Normalization of the polarization curves to the ECSA (Fig. S7, ESI‡) further confirms the higher intrinsic activity of GR*$_{ChOx}$ compared to GR*$_{ElOx}$. We attribute this to the higher degree of carbonate grafting of GR*$_{ChOx}$ which can be regarded as a formal replacement of OH^- with CO_3^{2-}, modulating the electronic structure and thus the redox activity of the metal center. According to the HSAB principle, the softer base OH^- donates electron density to the adjacent metal centers more readily than the harder base CO_3^{2-}.[45] Therefore, a lower electron density is expected at the electrocatalytically active transition-metal center for GR*$_{ChOx}$ as compared to GR*$_{ElOx}$. Investigations on NiFe-LDHs have shown that such reduced electron density, charge delocalization and the incorporation of electron-withdrawing anions or cations can be beneficial for the facilitation of higher-valent electrophilic transition metal ion sites. At these sites, the nucleophilic attack of hydroxyl and water molecules is promoted, leading to improved adsorption of reaction intermediates during the OER.[46,47]

In order to investigate the stability and versatility of the catalyst during continuous operation, chronopotentiometry experiments were conducted. Here, the galvanostatic performance was investigated by applying a current corresponding to a current density of 10 mA cm^{-2} for 24 h in 1 M KOH (Fig. S8, ESI‡). Over this time, the necessary overpotential to maintain this current was recorded. Initially, GR*$_{ElOx}$ and GR*$_{ChOx}$ allow achieving the current density of 10 mA cm^{-2} at lower potentials than the uncoated substrate. Throughout the experiment, an increase of the potential was recorded for GR*$_{ElOx}$ (+21 mV), GR*$_{ChOx}$ (+30 mV), and the uncoated bare steel substrate (+26 mV).

The decrease in the performance of both GR* samples may be related to various effects such as the physical detachment of the catalyst material under operating conditions or degradation resulting in the loss of activity and active sites.[23] Interestingly, the potential of GR*$_{ChOx}$ increased the most during the first 2 hours of the experiment (inset Fig. S8, ESI‡). Most likely, this is caused by the energy released during harsh chemical oxidation, which might result in a less intimate contact between the substrate and the catalyst. Thus, GR*$_{ChOx}$ is more prone to a loss of electrical contact during operation. Due to the prior electrochemical treatment, GR*$_{ElOx}$ shows an initial performance increase which could be related to the easier formation of percolation paths and active sites. In GR*$_{ChOx}$, these improving changes are delayed and masked by possible detrimental alterations discussed earlier.

As expected, the performance of the uncoated steel also decreases, likely due to the formation of inactive corrosion products blocking the access to more electroactive centres. The formation of such products was also evidenced by the brownish-black staining of the surface after the experiment.

To gain insight into the alteration of catalysts during catalysis, post-catalysis SEM studies of the employed electrodes were performed. For the bare steel substrate, the results evidence the formation of a porous surface layer (Fig. S9a and b, ESI‡). This indicates the oxidation of Fe^0 to soluble Fe-species as predicted by the Pourbaix diagram discussed earlier. Alteration of the electrode under the current load was also evident by the previously described brown-black staining. The post-catalysis XRD measurements (Fig. S10, ESI‡) indicate the presence of $Fe_{1-x}O$ and Fe_3O_4 deposits formed *via* reprecipitation. Presumably, these deposits are responsible for the deterioration of catalytic performance during the chronopotentiometry measurements.

For GR*$_{ChOx}$ and GR*$_{ElOx}$ catalysts, the platelet-like morphology was generally preserved, although a loss of the catalyst material (−23%, determined gravimetrically) was observed during the stability experiment. The SEM analysis moreover indicates the degradation of the hexagonal platelet shapes to more rounded corners and the secondary deposits covering the platelets after 24 h (Fig. S9c–f, ESI‡). Based on our previous study examining the stability of mössbauerite in a setup using a rotating disc electrode, we conclude that during electrolysis, small amounts of the catalyst can be dissolved into the electrolyte and are redeposited as amorphous iron (oxy)hydroxides.[23] The post-catalysis XRD measurements (Fig. S10, ESI‡) do not show any crystalline phase other than GR* and steel.

Conclusions

Manufacturing catalyst-coated electrodes through a controlled, cheap, and time-efficient corrosion engineering process of steel presents a viable way to obtain electrodes for the oxygen evolution reaction. A carbon steel substrate was used to deposit the known iron-only electrocatalyst GR* *via* its precursor GR. Clearly, the choice of oxidation method, *i.e.*, chemical or electrochemical oxidation, has a notable influence on the structural constitution and performance of the catalyst. Chemical oxidation gives a higher degree of grafting, which appears to be advantageous for the catalytic performance.

Based on these results, further developments will aim towards maximizing the catalyst's coverable surface area, *e.g.*, by deposition on steel wool or iron foam. Of course, concomitant doping can further improve the performance as well.

Author contributions

Sebastian Weiß: investigation, formal analysis, writing – original draft, and writing – review & editing; A. V. Radha: investigation; Catherine McCammon: investigation, formal analysis, and resources; Michael Ertl: investigation; Josef Breu: resources, supervision, writing – original draft, and writing – review & editing.

Conflicts of interest

There are no conflicts of interest to declare.

Acknowledgements

The authors are grateful for financial support from the Deutsche Forschungsgemeinschaft (DFG) within the collaborative research center 840 "From particulate nanosystems to mesotechnology" (79971943; SFB 840). They thank Mirijam Zobel for the measurement time with her powder X-ray diffractometer. The authors thank O. Khoruzhenko for the graphic design. They further thank R. Timmins and C. Habel for their advice and proofreading the manuscript. They appreciate the support from the Keylab for Optical and Electron Microscopy of the Bavarian Polymer Institute (BPI). They thank Marco Schwarzmann for the corresponding measurements. S. W. acknowledges the support from the Elite Network of Bavaria and thanks the graduate school of the Bavarian Center for Battery Technology (BayBatt) for ongoing support.

Notes and references

1 Z. W. Seh, J. Kibsgaard, C. F. Dickens, I. Chorkendorff, J. K. Nørskov and T. F. Jaramillo, *Science*, 2017, **355**, eaad4998.
2 S. Chu and A. Majumdar, *Nature*, 2012, **488**, 294–303.
3 J. Yin, A. Molini and A. Porporato, *Nat. Commun.*, 2020, **11**, 4781.
4 D. Zhao, Y. Pi, Q. Shao, Y. Feng, Y. Zhang and X. Huang, *ACS Nano*, 2018, **12**, 6245–6251.
5 I. Roger, M. A. Shipman and M. D. Symes, *Nat. Rev. Chem.*, 2017, **1**, 0003.

6 L. Wu, L. Yu, X. Xiao, F. Zhang, S. Song, S. Chen and Z. Ren, *Research*, 2020, **2020**, 17.

7 R. Tolouei, J. Harrison, C. Paternoster, S. Turgeon, P. Chevallier and D. Mantovani, *Phys. Chem. Chem. Phys.*, 2016, **18**, 19637–19646.

8 D. G. Lee and H. Gai, *Can. J. Chem.*, 1993, **71**, 1394–1400.

9 J. M. Schreyer and L. T. Ockerman, *Anal. Chem.*, 1951, **23**, 1312–1314.

10 R. M. Cornell and U. Schwertmann, *The Iron Oxides: Structure, Properties, Reactions, Occurrences and Uses*, Wiley, 2006.

11 S. Papavinasam, in *Corrosion Control in the Oil and Gas Industry*, ed. S. Papavinasam, Gulf Professional Publishing, Boston, 2014, pp. 133–177.

12 S. Anantharaj, S. R. Ede, K. Karthick, S. Sam Sankar, K. Sangeetha, P. E. Karthik and S. Kundu, *Energy Environ. Sci.*, 2018, **11**, 744–771.

13 H. Zhong, J. Wang, F. Meng and X. Zhang, *Angew. Chem., Int. Ed.*, 2016, **55**, 9937–9941.

14 B. A. Marinho, R. O. Cristóvão, R. A. R. Boaventura and V. J. P. Vilar, *Environ. Sci. Pollut. Res.*, 2019, **26**, 2203–2227.

15 F. Guo, Y. Wu, H. Chen, Y. Liu, L. Yang, X. Ai and X. Zou, *Energy Environ. Sci.*, 2019, **12**, 684–692.

16 X. Liu, B. You and Y. Sun, *ACS Sustainable Chem. Eng.*, 2017, **5**, 4778–4784.

17 H. Schäfer, S. Sadaf, L. Walder, K. Kuepper, S. Dinklage, J. Wollschläger, L. Schneider, M. Steinhart, J. Hardege and D. Daum, *Energy Environ. Sci.*, 2015, **8**, 2685–2697.

18 H. Sun, J. Brocato and M. Costa, *Curr. Environ. Health Rep.*, 2015, **2**, 295–303.

19 S. Mitra, A. Sarkar and S. Sen, *Nanotechnol. Environ. Eng.*, 2017, **2**, 11.

20 Y. Liu, X. Liang, L. Gu, Y. Zhang, G.-D. Li, X. Zou and J.-S. Chen, *Nat. Commun.*, 2018, **9**, 2609.

21 H. Schäfer, S. M. Beladi-Mousavi, L. Walder, J. Wollschläger, O. Kuschel, S. Ichilmann, S. Sadaf, M. Steinhart, K. Küpper and L. Schneider, *ACS Catal.*, 2015, **5**, 2671–2680.

22 Y. Wang, D. Yan, S. El Hankari, Y. Zou and S. Wang, *Adv. Sci.*, 2018, **5**, 1800064.

23 M. Ertl, C. Andronescu, J. Moir, M. Zobel, F. E. Wagner, S. Barwe, G. Ozin, W. Schuhmann and J. Breu, *Chem. – Eur. J.*, 2018, **24**, 9004–9008.

24 M. Usman, J. M. Byrne, A. Chaudhary, S. Orsetti, K. Hanna, C. Ruby, A. Kappler and S. B. Haderlein, *Chem. Rev.*, 2018, **118**, 3251–3304.

25 U. Schwertmann and H. Fechter, *Clay Miner.*, 1994, **29**, 87–92.

26 M. Abdelmoula, P. Refait, S. H. Drissi, J. P. Mihe and J. M. R. Génin, *Corros. Sci.*, 1996, **38**, 623–633.

27 L. Legrand, L. Mazerolles and A. Chaussé, *Geochim. Cosmochim. Acta*, 2004, **68**, 3497–3507.

28 G. J. Long, T. Cranshaw and G. Longworth, *Moessbauer Eff. Ref. Data J.*, 1983, **6**, 42–49.

29 C. McCammon, V. Chaskar and G. Richards, *Meas. Sci. Technol.*, 1991, **2**, 657.

30 C. A. McCammon, *Hyperfine Interact.*, 1994, **92**, 1235–1239.

31 C. Prescher, C. McCammon and L. Dubrovinsky, *J. Appl. Crystallogr.*, 2012, **45**, 329–331.

32 Bio-Rad Laboratories, Chelex(R) 100 and Chelex 20 Chelating Ion Exchange Resin – Instruction Manual, https://www.bio-rad.com/webroot/web/pdf/lsr/literature/LIT200.pdf, 2021.

33 H. Deng, C. Zhang, Y. Xie, T. Tumlin, L. Giri, S. P. Karna and J. Lin, *J. Mater. Chem. A*, 2016, **4**, 6824–6830.

34 C. C. L. McCrory, S. Jung, J. C. Peters and T. F. Jaramillo, *J. Am. Chem. Soc.*, 2013, **135**, 16977–16987.

35 P. Refait and J.-M. Génin, *Corros. Sci.*, 1993, **34**, 797–819.

36 G. Ona-Nguema, M. Abdelmoula, F. Jorand, O. Benali, A. Géhin, J. C. Block and J. M. R. Génin, *Hyperfine Interact.*, 2002, **139**, 231–237.

37 L. Legrand, S. Savoye, A. Chausse and R. Messina, *Electrochim. Acta*, 2000, **46**, 111–117.

38 J.-M. R. Génin, C. Ruby, A. Géhin and P. Refait, *C. R. Geosci.*, 2006, **338**, 433–446.

39 P. Lyu, M. Ertl, C. J. Heard, L. Grajciar, A. V. Radha, T. Martin, J. Breu and P. Nachtigall, *J. Phys. Chem. C*, 2019, **123**, 25157–25165.

40 J. M. R. Génin, A. Christy, E. Kuzmann, S. Mills and C. Ruby, *Hyperfine Interact.*, 2014, **226**, 459–482.

41 J. M. R. Génin, S. J. Mills, A. G. Christy, O. Guérin, A. J. Herbillon, E. Kuzmann, G. Ona-Nguema, C. Ruby and C. Upadhyay, *Mineral. Mag.*, 2014, **78**, 447–465.

42 C. Ruby, M. Abdelmoula, S. Naille, A. Renard, V. Khare, G. Ona-Nguema, G. Morin and J.-M. R. Génin, *Geochim. Cosmochim. Acta*, 2010, **74**, 953–966.

43 S. Weiß, M. Ertl, S. D. Varhade, A. V. Radha, W. Schuhmann, J. Breu and C. Andronescu, *Electrochim. Acta*, 2020, **350**, 136256.

44 J.-M. R. Génin, C. Ruby and C. Upadhyay, *Solid State Sci.*, 2006, **8**, 1330–1343.

45 H. Xu, D. C. Xu and Y. Wang, *ACS Omega*, 2017, **2**, 7185–7193.

46 L. Fan, P. Zhang, B. Zhang, Q. Daniel, B. J. J. Timmer, F. Zhang and L. Sun, *ACS Energy Lett.*, 2018, **3**, 2865–2874.

47 Y.-Y. Dong, D.-D. Ma, X.-T. Wu and Q.-L. Zhu, *Inorg. Chem. Front.*, 2020, **7**, 270–276.

Electronic Supplementary Material (ESI) for Materials Advances.

Sustainable Oxygen Evolution Catalysis - Electrochemical Generation of Mössbauerite *via* Corrosion Engineering of Steel

Sebastian Weiß,[a,b] A.V. Radha,[b] Michael Ertl,[b] Catherine McCammon [c] and Josef Breu [a,b*]

[a] Bavarian Center for Battery Technology (BayBatt), University of Bayreuth, Universitätsstr. 30, 95447 Bayreuth (Germany)

[b] Department of Chemistry, University of Bayreuth, Universitätsstr. 30, 95447 Bayreuth (Germany)

[c] Bayerisches Geoinstitut, University of Bayreuth, Universitätsstr. 30, 95447 Bayreuth (Germany)

* Correspondence to: josef.breu@uni-bayreuth.de

1. Cyclic voltammogram recorded during the deposition process

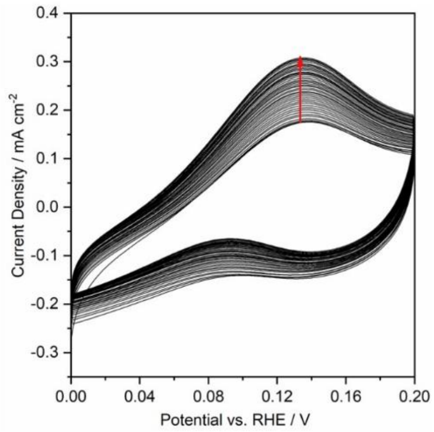

Fig. S1: Voltammogram recorded during the deposition of GR with a scan speed of 5 mV s^{-1}.

Cyclic voltammetry in the GR associated stability region was performed. The applied potentials ensure a suitable Fe^{2+}/Fe^{3+} ratio for the deposition of GR. Maximum anodic currents are found at 0.13 V vs. RHE. With increasing number of cycles, the current density increases from 0.175 mA cm^{-2} to 0.308 mA cm^{-2}.

2. Electrooxidation of Green Rust

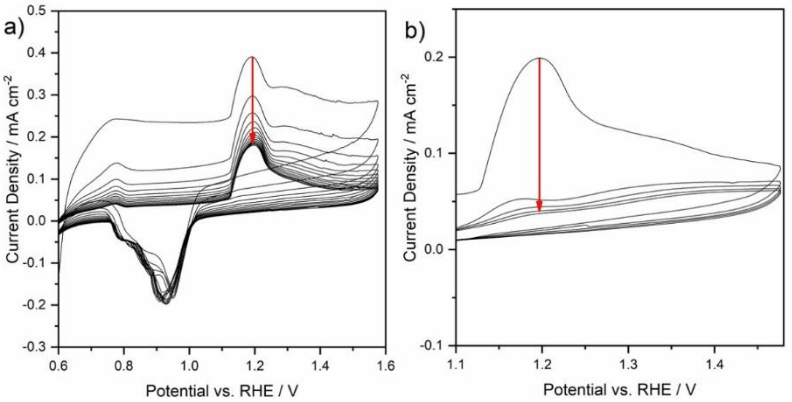

Fig. S2: a) Voltammogram recorded to identify a suitable oxidation potential to obtain GR* from GR. b) Voltammogram recorded during the oxidation of the material. Voltammograms were recorded with a scan speed of 5 mV s^{-1}.

Cyclic voltammetry was performed to identify a suitable oxidation potential to facilitate the oxidation of GR to GR*. For screening, a potential range from 0.6 V to 1.6 V was chosen. The recorded voltammogram features a small anodic wave at 0.78 V and an intense one at 1.20 V. A broad cathodic wave peaked between 0.95-0.91 V.

By reducing the potential range to 1.10-1.47 V, only the anodic event can be observed. Rapidly decreasing current densities indicate a quick oxidation process.

3. SEM micrographs of the oxidized and untreated samples

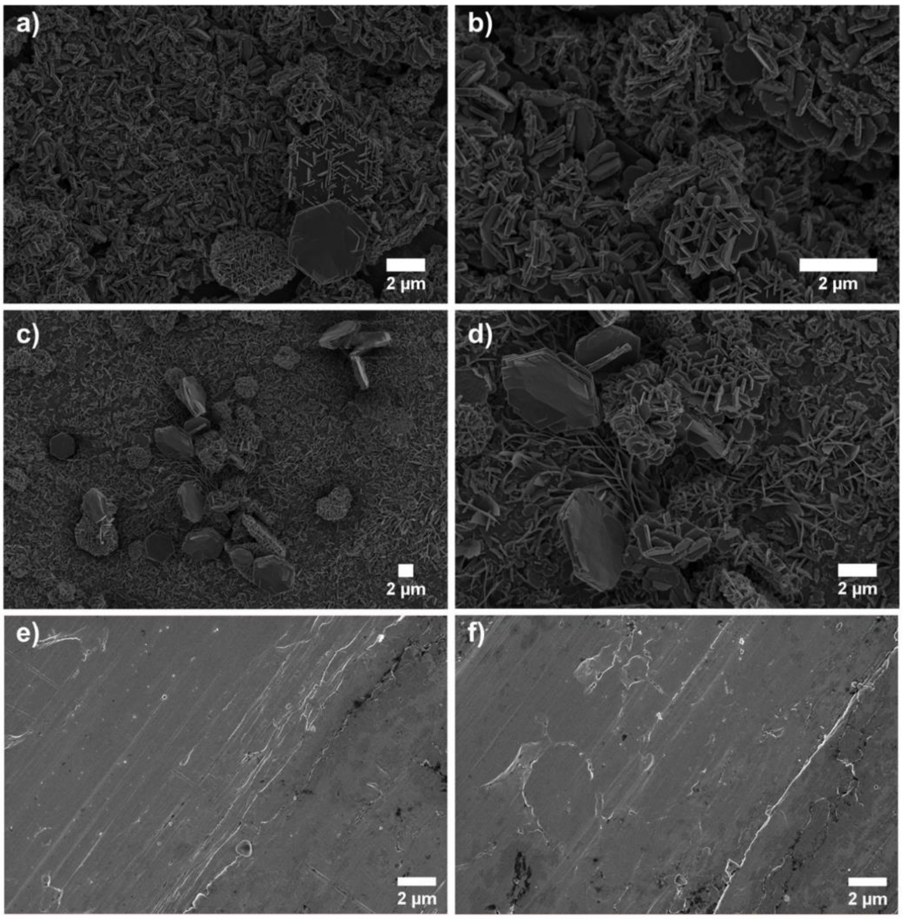

Fig. S3: SEM micrographs of the GR* samples. The GR*$_{ChOx}$ and GR*$_{ElOx}$ catalysts are shown in a,b) and c,d), respectively. Both feature similar morphologies of big, platy crystals intergrown with smaller platelets. In e) and f), the untreated steel plate is shown. Apparent roughness originates from the polishing procedure.

4. SEM micrograph of the unoxidized GR sample

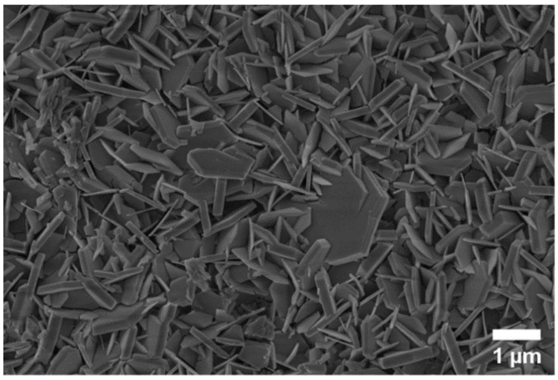

Fig. S4: SEM micrograph of GR before oxidation. The material features a similar morphology to these of GR*. Big, platy crystals intergrown with smaller platelets are observable and underline the assumption of a topotactic conversion from GR to GR*$_{ChOx}$ or GR*$_{ElOx}$. Please note that partial oxidation is possible due to oxygen volatility and the necessary transfer of the sample.

5. Mössbauer spectroscopy

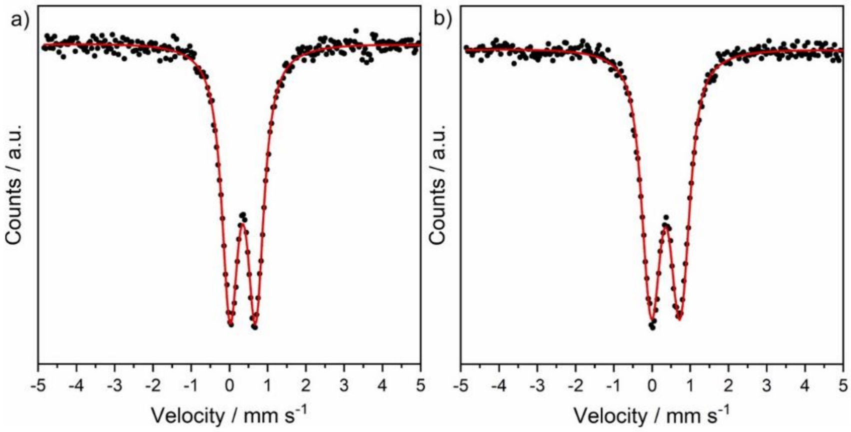

Fig. S5: Room temperature Mössbauer spectra of a) GR*$_{ChOx}$ and b) GR*$_{ElOx}$. No Fe^{2+} impurities are detectable in either of the two samples.

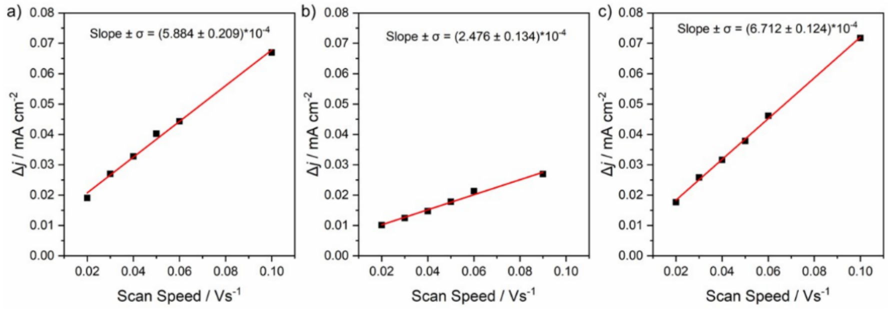

Fig. S6: Plots to determine the ECSA based on the difference between cathodic and anodic current depending on the scan speed: a) GR*$_{\text{ChOx}}$, b) blank substrate and c) GR*$_{\text{ElOx}}$.

6. Electrochemical Active Surface Area (ECSA)

7. ECSA normalized Linear Sweep Voltammograms

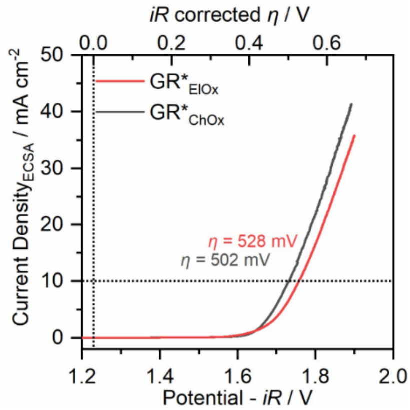

Fig. S7: ECSA normalized polarization curves of GR*$_{ChOx}$ and GR*$_{ElOx}$. LSVs were recorded with a scan rate of 5 mV s^{-1} in O_2-saturated purified 1 M KOH solutions.

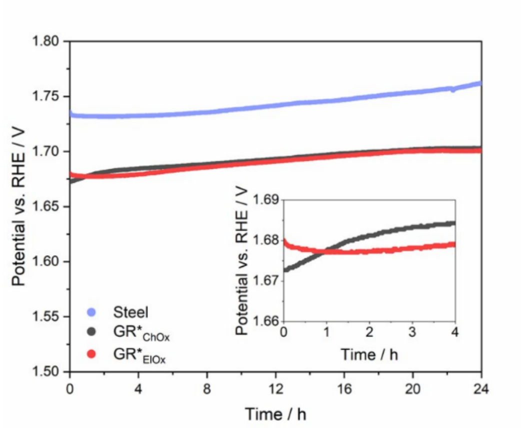

Fig. S8: Galvanostatic stability test of GR*$_{ChOx}$, GR*$_{ElOx}$, and steel in 1 M KOH at 10 mA cm^{-2} for 24 hours.

8. Galvanostatic stability tests

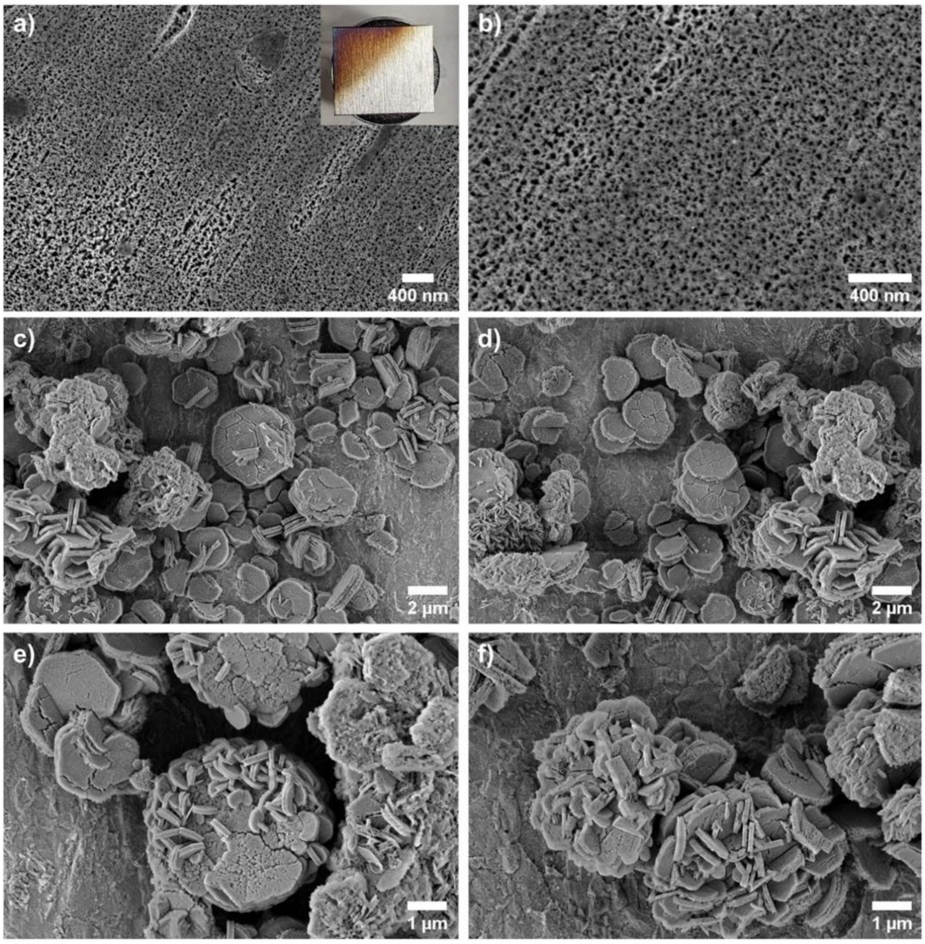

Fig. S9: Representative post-catalysis SEM micrographs for the bare steel (a,b), GR*$_{ChOx}$ (c, d), and GR*$_{ElOx}$ (e, f) sample after chronopotentiometry for 24 h at a current density of 10 mA cm^{-2}. Both samples show apparent degradation of the platelet-like catalyst morphology with some secondary deposit onto these platelets. A photograph of a partly immersed steel plate shows the apparent staining after electrocatalysis.

9. Post-catalysis investigations: Scanning Electron Microscopy

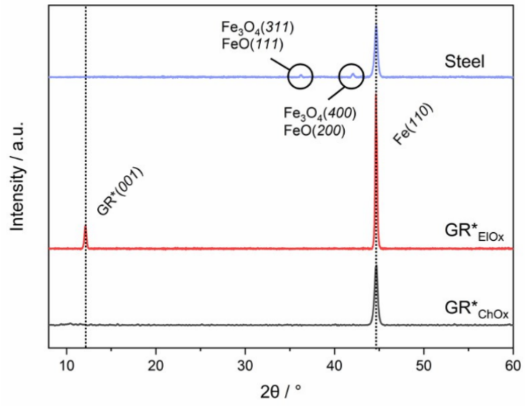

Fig. S10: Post-catalysis XRD patterns (Cu K_α source) of the bare steel substrate, the GR*$_{ChOx}$, and GR*$_{ElOx}$ sample after chronopotentiometry for 24 h at a current density of 10 mA cm^{-2}. The bare steel substrate exhibits weak reflections which can be assigned to the presence of Fe_3O_4 (PDF #01-072-2303) and FeO (PDF #00-006-0615). GR*$_{ChOx}$ does not show any reflections, which indicates partial dissolution and thus the complete attenuation of the very weak (*001*) reflection. Due to the stronger initial intensity of the (*001*) reflection in GR*$_{ElOx}$, the signal is still detectable post-catalysis.

10. Post-catalysis investigations: X-ray diffraction

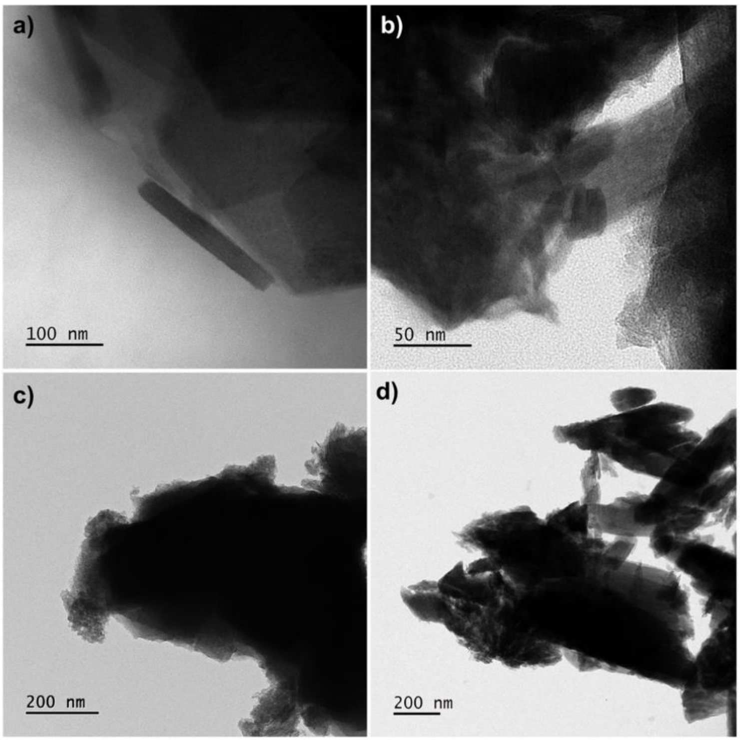

Fig. S11: Representative TEM micrographs from GR*$_{ChOx}$ (a), and GR*$_{ElOx}$ (b) before catalysis. Both feature similar morphologies of big, platy crystals partially intergrown with smaller platelets. The big platelets are composed of multiple individual layers. Post-catalysis TEM micrographs of GR*$_{ChOx}$ (c), and GR*$_{ElOx}$ (d) show that the platelet-like morphology is generally preserved but apparently overgrown by second phase.

11. Post-catalysis investigations: Transmission Electron Microscopy

7 List of Publications

Publications being part of this thesis:

S. Weiß, M. Ertl, S.D. Varhade, A.V. Radha, W. Schuhmann, J. Breu, C. Andronescu: Trivalent iron rich CoFe layered oxyhydroxides for electrochemical water oxidation, *Electrochimica Acta*, **2020**, 136256.

A.V. Radha, S. Weiß, I. Sanjuán, M. Ertl, C. Andronescu, J. Breu: The Effect of Interlayer Anion Grafting on Water Oxidation Electrocatalysis: A Comparative Study of Ni- and Co-Based Brucite-Type Layered Hydroxides, Layered Double Hydroxides and Hydroxynitrate Salts, *Chemistry - A European Journal*, **2021**, 16930-16937.

S. Weiß, A.V. Radha, M. Ertl, C. McCammon, J. Breu: Sustainable oxygen evolution catalysis – electrochemical generation of mössbauerite via corrosion engineering of steel, *Materials Advances*, **2021**, 5650-5656.

Further publications:

S. Weiß, J. Breu: Lithium-Ionen-Batterien - Herausforderungen der aktuellen Technologien, *Spektrum Magazin*, **I/2019**, 30-33.

S. Weiß, A. Loginov: From Science in the Train to Hiking at Lake Baikal: Manifold Experiences during the 9th German-Russian Travelling Seminar, *PCnano Journal*, **2019**, 9-13.

P. Loch, K. W. Bø Hunvik, F. Puchtler, S. Weiß, K. K. Seljelid, P. M. Røren, S. Rudic, S. Raaen, K. D. Knudsen, H. N. Bordallo, J. O. Fossum, J. Breu: Spontaneous formation of an ordered interstratification upon Ni-exchange of Na-fluorohectorite, *Applied Clay Science*, **2020**, 105831.

V. Dudko, O. Khoruzhenko, S. Weiß, M. Daab, P. Loch, W. Schwieger, J. Breu: Repulsive Osmotic Delamination: 1D Dissolution of 2D Materials, *Advanced Materials Technologies*, **2022**, 2200553.

M. Stevenson, S. Weiß, G. Cha, M. Schamel, L. Jahn, D. Friedrich, M. A. Danzer, J. Y. Cheong, J. Breu: Osmotically delaminated silicate nanosheet-coated NCM for ultra-stable Li^+ storage and chemical stability towards long-term air exposure, *to be submitted*.

8 Acknowledgements

I want to express my deep gratitude to Prof. Josef Breu for the engaging topic of my thesis, his support, scientific guidance, and trust. I appreciate the possibility of working on highly engaging projects in a modern research environment while being given a chance to develop both my topic and myself.

Prof. Takayoshi Sasaki was a fantastic host and supervisor during my time at National Institute for Material Science in Tsukuba. I am grateful for his time and appreciate his guidance and valuable advice in the chemistry and physics of 2D materials.

I thank Prof. Corina Andronescu for her time and efforts with our joint projects and cooperation, which I enjoyed enormously.

I would like to thank Dr. Catherine McCammon from the Bavarian Research Institute of Experimental Geochemistry and Geophysics (BGI) for many helpful discussions and explanations about Mössbauer spectroscopy and performing measurements.

Many things have only been made possible by the professors, staff, and students of the Bavarian Centre for Battery Technology (BayBatt). I appreciate many engaging scientific exchanges, support, and the provision of research infrastructure.

My gratitude also belongs to the organizers and members of the Elite Study Program "Macromolecular Science" and the Elite Network of Bavaria for interdisciplinary insights and the possibility to grow personally.

For always having an open ear for challenges and readily providing practical advice and help, I would like to express my gratitude to our technicians Marco Schwarzmann, Florian Puchtler, and Michael Thelen.

For all the organization, quick help, and management behind the scenes, I would like to acknowledge our secretaries Petra Seidler, Iris Raithel, and Silke Reimann.

A big thanks to the whole team of the Inorganic Chemistry 1 for a lot of helpful discussions and the pleasant work atmosphere. Notably, I want to thank my lab colleagues Max Stevenson, Dr. Gihoon Cha, and Ingmar Pietsch, for the great teamwork and mutual support. Particularly, I would like to acknowledge Dr. Christoph Habel, who also became a great friend.

As the people with a tremendous indirect contribution, I would like to thank my friends for being the best company and making it possible to enjoy a rich social life besides work, getting honest advice when wanted, and the necessary distraction when needed.

Finally, I would like to express my deep and sincere gratitude for my family and their everlasting support. I thank my family from the bottom of my heart, especially my mother, who has always supported me and without whom this thesis would not have been possible. Thank you for your unconditional support and for everything that you have done – this work is dedicated to you. I would also like to specifically thank and commemorate my grandfather, whose broad interest and untiring endurance to expand his knowledge have profoundly shaped me. I will always be grateful to him for his example and the conveyance of these values.

9 Eidesstattliche Erklärung

(Eidesstattliche) Versicherungen und Erklärungen

(§ 9 Satz 2 Nr. 3 PromO BayNAT)

Hiermit versichere ich eidesstattlich, dass ich die Arbeit selbstständig verfasst und keine anderen als die von mir angegebenen Quellen und Hilfsmittel benutzt habe (vgl. Art. 64 Abs. 1 Satz 6 BayHSchG).

(§ 9 Satz 2 Nr. 3 PromO BayNAT)

Hiermit erkläre ich, dass ich die Dissertation nicht bereits zur Erlangung eines akademischen Grades eingereicht habe und dass ich nicht bereits diese oder eine gleichartige Doktorprüfung endgültig nicht bestanden habe.

(§ 9 Satz 2 Nr. 4 PromO BayNAT)

Hiermit erkläre ich, dass ich Hilfe von gewerblichen Promotionsberatern bzw. -vermittlern oder ähnlichen Dienstleistern weder bisher in Anspruch genommen habe noch künftig in Anspruch nehmen werde.

(§ 9 Satz 2 Nr. 7 PromO BayNAT)

Hiermit erkläre ich mein Einverständnis, dass die elektronische Fassung meiner Dissertation unter Wahrung meiner Urheberrechte und des Datenschutzes einer gesonderten Überprüfung unterzogen werden kann.

(§ 9) Satz 2 Nr. 8 PromO BayNAT)

Hiermit erkläre ich mein Einverständnis, dass bei Verdacht wissenschaftlichen Fehlverhaltens Ermittlungen durch universitätsinterne Organe der wissenschaftlichen Selbstkontrolle stattfinden können.

Bayreuth, 12.10.2023

…………………………………………………………………………………….

Ort, Datum Sebastian Weiß